Nondifferentiable energy minimization for cohesive fracture in a discontinuous Galerkin finite element framework

by

Mohammadreza Hirmand

A thesis
presented to the University of Waterloo
in fulfillment of the
thesis requirement for the degree of
Doctor of Philosophy
in
Mechanical and Mechatronics Engineering

Waterloo, Ontario, Canada, 2019

Examining Committee Membership

The following served on the Examining Committee for this thesis. The decision of the Examining Committee is by majority vote.

External Examiner:	Raul Radovitzky, Professor Department of Aeronautics and Astronautics, Massachusetts Institute of Technology
Supervisor(s):	Katerina Papoulia, Associate Professor Department of Applied Mathematics and Department of Mechanical and Mechatronics Engineering, University of Waterloo
	Hamid Jahedmotlagh, Professor Department of Mechanical and Mechatronics Engineering, University of Waterloo
Internal Member:	Kaan Inal, Associate Professor Department of Mechanical and Mechatronics Engineering, University of Waterloo
Internal Member:	John Montesano, Assistant Professor Department of Mechanical and Mechatronics Engineering, University of Waterloo
Internal-External Member:	Robert Gracie, Associate Professor Department of Civil and Environmental Engineering, University of Waterloo

Author's declaration

I hereby declare that I am the sole author of this thesis. This is a true copy of the thesis, including any required final revisions, as accepted by my examiners

I understand that my thesis may be made electronically available to the public.

Abstract

Until recently, most works on the computational modelling of fracture relied on a Newtonian mechanics approach, i.e., momentum balance equations describing the motion of the body along with fracture criteria describing the evolution of fractures. Robustness issues associated with this approach have been identified in the previous literature, several of which, as this thesis shows, due to the discontinuous dependence of stress field on the deformation field at the time of insertion of displacement discontinuities. Lack of continuity limits applicability of the models and undermines reliability of the numerical solutions. In particular, solutions often show non-convergent behaviour with time step refinement and exhibit nonphysical velocity fields and crack activation patterns. In addition, implicit time-stepping schemes, which are favoured in quasi-static and low-velocity problems, are challenging in such models. This is not a coincidence but a manifestation of algorithmic pitfalls of such methods.

Continuity of stresses is in general hard to achieve in a computational model that employs a crack initiation criterion. Energy (variational) approaches to fracture have gained increased popularity in recent years. An energy approach has been shown to avoid introduction of a crack initiation criterion. The central idea of this model is the minimization of a mechanical energy functional, whose term representing the energy due to the cracks is a nondifferentiable function of the interface openings at zero opening displacement. A consequence of this formulation is that crack initiation happens automatically as a by-product of energy minimization. This avoids the complexities arising from the introduction of an extrinsic activation criterion but entails minimization of a nondifferentiable potential.

The aim of this research is to develop robust and efficient computational algorithms for numerical implementation of the energy approach to cohesive fracture. Two computational algorithms have been proposed in a discontinuous Galerkin finite element framework, including a continuation algorithm which entails successive smooth approximations of the nondifferentiable functional and a block coordinate descent algorithm which uses generalized differential calculus for the treatment of nondifferentiability. These methods allow for a seamless transition from the uncracked to the cracked state, making possible the use of iterative solvers with implicit time-stepping, and completely sidestepping robustness issues of previous computational frameworks.

A critical component of this work is validation of the robustness of the proposed numerical methods. Various numerical simulations are presented including time step and mesh size convergence studies and qualitative and quantitative comparison of simulations with experimental observations and theoretical findings. In addition, an energy-based hydromechanical model and computational algorithm is presented for hydraulic fracturing in

impermeable media, which shows the crucial importance of continuity in multi-physics modelling. A search algorithm is developed on the basis of graph theory to identify the set of fluid-pressurized cracks among cracks in naturally fractured domains.

Acknowledgements

First and foremost, I would like to thank my supervisor, Professor Katerina Papoulia, for her insightful guidance and continuous support throughout my time as her student. I greatly benefited from her immense knowledge and careful advice throughout the course of my research. I would also like to pass my sincere gratitude to my co-supervisor, Professor Hamid Jahed, who made his support and advice available in various ways since the very first day.

My sincere thanks also go to the committee members for reviewing this thesis. They generously gave of their time to offer valuable comments that improved my work. I am grateful to Professor Stephen Vavasis for his expert comments and discussions throughout the course of my research.

Last but not least, my deep and sincere gratitude to my family: my parents and my sisters and brother. Their unparalleled love and heart-warming encouragement have kept me going in tough times not only through my PhD but throughout my life.

Dedication

To my parents for their endless love and sacrifice

Table of Contents

List of Algorithms

List of Figures

List of Abbreviations

Block-CD Block Coordinate Descent

CCS Compact Compression Specimen

CMOD Crack Mouth Opening Displacement

CPZ Cohesive Process Zone

DG Discontinuous Galerkin

FE Finite Element

FEM Finite Element Method

FPZ Fracture Process Zone

IVP Initial Value Problem

LEFM Linear Elastic Fracture Mechanics

XFEM eXtended Finite Element Method

Chapter 1

State-of-the-art of cohesive zone modelling: a review

1.1 Introduction

Fracture is one of the most commonly encountered failure modes of materials observed in a wide range of engineering applications from aerospace and automotive to biomechanics and geomechanics. The prevention of fracture-induced failure is, therefore, a major concern in engineering design. There are numerous works in the engineering fracture mechanics literature that deal with an analytical solution to the problem of a single crack in a solid body, see e.g., [3] and references therein. In these works, crack growth is assumed to occur by the extension of the crack as an idealized surface in a dominant path. In real-life circumstances, however, fracturing processes mainly involve the nucleation, growth, and coalescence of multiple cracks and micro-branches. As explained in [36], "all fracture is dynamic at some scale" due to the dynamic process of the bond rupture, even when dynamic effects are not significant at the macroscopic scale and the crack appears to be advancing quasi-statically. Thus, "the dynamic fracture problem is the most fundamental in the science of fracture."

Fracture in brittle and quasi-brittle materials has been extensively studied from different perspectives by researchers in the theoretical, experimental and computational communities. A recent review of the theoretical and experimental developments in dynamic brittle fracture has been given by Fineberg and Bouchbinder [47]. Theoretically, the Rayleigh wave speed v_R is the limiting velocity of a mode-I propagating crack [50]. However, experiments have shown that the crack velocity is limited by just about half of its theoretical value and never reaches v_R [50]. Experimental observations have also shown that, under certain conditions, a single crack will bifurcate into two growing cracks [130]. For a crack propagating through a specimen at constant velocity, Yoffe [180] found that the hoop stress $\sigma_{\theta\theta}$ attains a maximum for a nonzero value of θ if the velocity of the crack is larger than $0.65v_R$. This work was probably the first to give an explanation of why a propagating crack in a linear elastic specimen bifurcates before it reaches the Rayleigh speed. Other experimental results have shown that the crack faces roughen at velocities $0.3 \sim 0.4v_R$ [132, 149]. The structure of this roughness is a periodic side branching conjoining the main crack [149]. Sharon et al. [150] suggest that this pattern is due to an inherent dynamic instability in the crack's advance when the velocity exceeds $0.36v_R$. These authors relate the fluctuations in velocity of the leading crack observed in the experiment to the growth of side branches. Ravi-Chandar et al. [133] describe the periodic patterns as an outcome of nucleation, growth and coalescence of microcracks. This differs from the previous reasoning as standalone microcracks are assumed to grow independently of the main crack and then coalesce to form the branches.

While the above theoretical and experimental developments have greatly enhanced our

understanding of the fracture phenomenon, they clearly show the inherent complexities in computational modelling of fracture. Within the context of continuum mechanics, fracture of solids can be modeled using either a strong discontinuity approach (also referred to as the discrete approach) or an approach in which the displacement field is continuous (also referred to as the smeared approach). In the discrete approach, the displacement of the solid body is allowed to be discontinuous across crack faces to achieve a clear physical representation of cracks. The most well-known theories behind the strong discontinuity approach are linear elastic fracture mechanics (LEFM) [75, 3], and the cohesive zone model [11, 43]. The finite element method (FEM) and its variants have been extensively used in numerically modelling discrete fracture. Among such methods one can count the interface element method [177, 25, 116], the discontinuous Galerkin (DG) method [96, 129, 68], the extended finite element method (XFEM) [99, 169, 13], the embedded discontinuity method [8, 7] and the cracking particle/node method [153, 128], to name only a few. In the smeared approach, the displacements are continuous everywhere but the material strength is gradually reduced to model material failure processes. Degradation of the material strength in the continuous approach is modelled by making use of continuum damage mechanics [88]. Successful modelling of dynamic crack propagation, including bifurcation, has been reported, for example, in [125, 114, 115] using nonlocal damage models [123].

The present research concerns computational modelling of cohesive crack propagation within the context of the discrete fracture approach. This review is therefore intended to be neither a complete survey of all existing approaches to failure modelling nor historically complete in any one area. In particular, the continuum damage mechanics approach as well as alternative frameworks such as peridynamics [152], the discrete element method [37] or molecular dynamics [74] are intentionally not touched upon in the remaining of this chapter. Instead, the main focus will be to discuss, firstly, the issues with existing cohesive zone modelling methods and, secondly, promising directions for future development, identified through a comprehensive review of the cohesive zone modelling literature. The remaining of this chapter is structured as follows. A brief description of the cohesive crack model will be given in Section 1.2. Issues with intrinsic and extrinsic cohesive crack models are then discussed in Sections 1.3. This is followed by discussing the issue of mesh dependence in Section 1.4. The hybrid discontinuous Galerkin method and energy approaches to fracture are those topics identified as promising and are discussed in Sections 1.5 and 1.6, respectively. Section 1.7 presents an overview on the objectives of this research and the methodologies used to achieve them. Finally, statement of contributions is given in Section 1.8.

1.2 The cohesive crack model

In the vast majority of materials, failure is a continuous process that involves gradual degradation of stiffness before a dominant crack forms. In fact, formation of cracks is usually associated with softening response after the material reaches its ultimate strength. Softening may be attributed to small-scale yielding, micro-crack initiation, growth and coalescence in the fracture process zone (FPZ) prior to the impending formation of the crack, as schematically shown in Figure 1.1. In LEFM, it is assumed that the size of the FPZ is small compared to a characteristic length of the specimen, thus neglected in the stress analysis of the solid body. A consequence of this assumption is that the theoretical stress field is singular (infinite magnitude) at the crack-tip in LEFM theories [3]. While the use of LEFM may be justified in perfectly brittle materials, the nonlinear material behaviour in the FPZ must be taken into account in the more general case as the utility of LEFM diminishes.

The concept of cohesive crack was first introduced by Barenblatt [11] and Dugdale [43] to describe the nonlinear failure processes occurring ahead of a forming crack-tip. In this model, the near-tip fracturing processes is lumped onto an extension of the crack faces referred to as the cohesive process zone (CPZ). The softening material behaviour is then modelled by postulating an opening-dependent traction in the CPZ expressed as a decaying function of the crack opening. As the maximum cohesive traction in the CPZ is equal to the maximum tensile strength of the material, the model avoids the nonphysical singular stress field occurring in LEFM. Various traction-separation functions have been proposed in the literature, a comprehensive review of which is given in [120].

Depending on how the pre-softening, elastic behaviour is modeled in the CPZ, cohesive crack models are categorized in two groups: intrinsic (or, initially elastic) models and extrinsic (or, initially-rigid) models. A schematic of the intrinsic and extrinsic cohesive

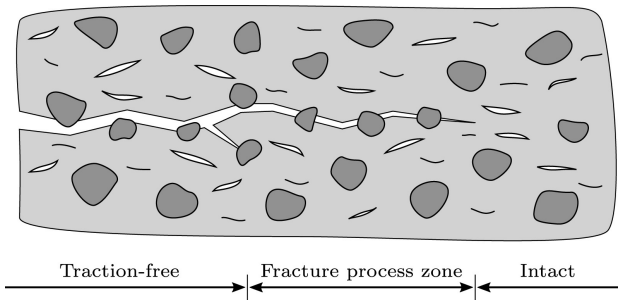

Figure 1.1: Schematic of the fracture process zone [62]

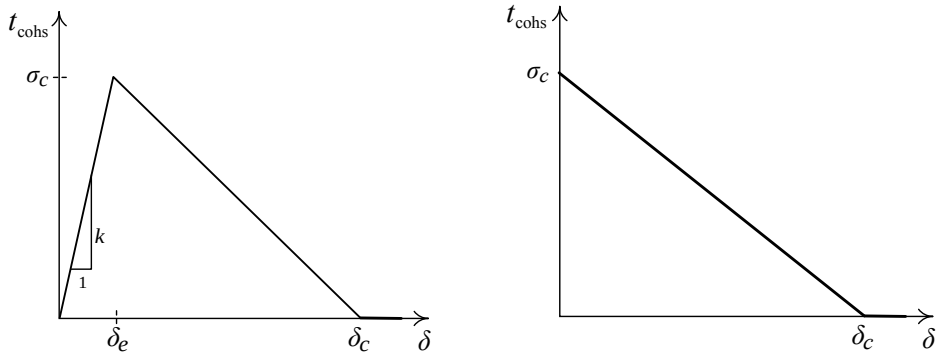

Figure 1.2: a) initially-elastic and b) initially-rigid cohesive models with linear softening

models with linear softening is shown in Figure 1.2. In these graphs, the horizontal axis represents some norm of the crack opening, δ, and the vertical axis show some norm of the cohesive traction, t_{cohs}. In both intrinsic and extrinsic models, the maximum effective stress attained is the material strength σ_c, followed by a descending branch until cohesion is lost at a critical effective opening δ_c. Whereas in the intrinsic model the maximum effective stress σ_c is associated with an elastic opening δ_e of the crack faces, in the extrinsic model no crack opening is allowed before σ_c is reached. In fact, intrinsic models involve an initially elastic branch with slope $k = \sigma_c/\delta_e$ representing the elastic stiffness of the material in the CPZ before the material strength is reached.

Intrinsic cohesive models are best suited for modelling pre-existing, physical initially elastic interfaces whose faces show relative elastic displacement prior to the onset of damage. In such cases, the parameter k represents the elastic stiffness of the material that bonds adjacent layers. Numerical implementation of intrinsic cohesive models is normally associated with embedding the discontinuity in the displacement field along the *a priori* known failure path from the start of the simulation [176]. Extrinsic cohesive models, on the other hand, are preferred for fracture of homogeneous solids, in which the failure path is not known in advance and no displacement discontinuity is present before the material strength is reached. Within a numerical simulation framework, this often amounts to the adaptive insertion of displacement discontinuities in the body [25]. The discretization scheme used for introducing displacement discontinuities is technically independent of the type of cohesive crack model.

1.3 Modelling cohesive cracks using interface elements

The interface element method is among the most widely used discretization schemes for modelling displacement discontinuities. In this method, displacement discontinuities (i.e., cracks) are allowed to propagate through the inter-element boundaries of the mesh using *interface elements*. Figure 1.3 schematically shows interface elements in 2D and 3D. To insert interface elements in the mesh, one has to duplicate the nodal points of the "bulk" elements sharing an edge of the mesh, allowing for a jump in the displacement field across the edge. The interface element method limits crack nucleation sites to a finite number of possible paths, thus introducing a degree of obvious mesh dependence. A discussion of the ramifications of this as well as a comparison with its alternative, XFEM, which allows introduction of cracks independent of element edges, will be given in Section 1.4.

Interface elements have been used with both intrinsic and extrinsic cohesive crack models. When the crack trajectory is unknown *a priori*, an intrinsic cohesive crack model requires that interface elements be inserted everywhere in the mesh at the start of the simulation as proposed by Xu and Needleman [177]. As noted by Klein et al. [84], this introduces artificial compliance to the finite element (FE) model with the elastic stiffness approaching zero in the limit of mesh size refinement. Alternatively, extrinsic cohesive models can be used in conjunction with adaptive insertion of interface elements whenever and wherever a fracture criterion is met as proposed by Camacho and Ortiz [25]. This approach suffers from an issue known as time-discontinuity [117] leading to several algorithmic pitfalls and nonphysical solutions. In the following subsections, we will discuss the artificial compliance and time-discontinuity issues in further detail.

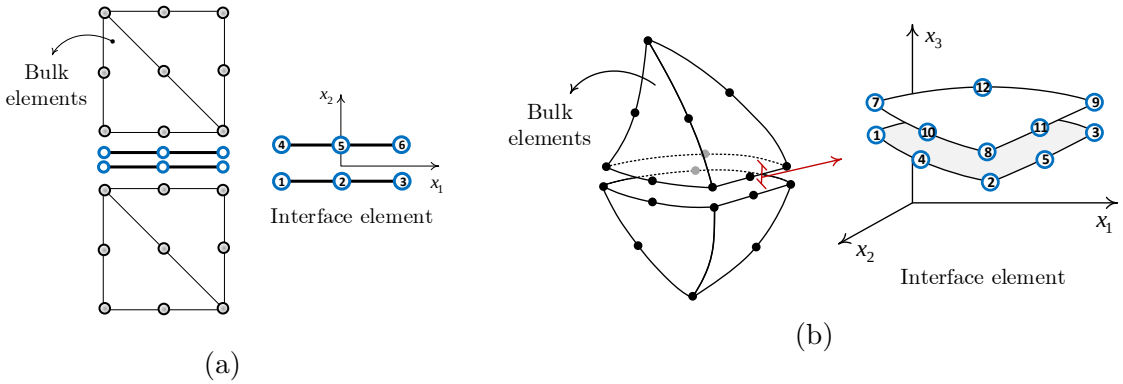

Figure 1.3: Schematic of interface elements in a) two-dimensional and b) three-dimensional meshes

1.3.1 Intrinsic models: the issue of artificial compliance

In order to explain the artificial compliance issue, let us consider the simple case of an elastic bar [84] as shown in Figure 1.4. The bar has elastic modulus E and is discretized with continuum elements of size h in its undeformed state. Consider now that interface elements of thickness zero and elastic stiffness k are inserted everywhere between the continuum elements. The effective modulus of the bar is [84]

$$E_{\text{eff}} = E\left(1 - \frac{1}{1 + kh/E}\right), \tag{1.1}$$

from which $E_{\text{eff}} < E \ \forall h, k > 0$, and $E_{\text{eff}} \to 0$ as $h \to 0 \ \forall k > 0$ making convergence under mesh refinement impossible. The opening induced by the elastic surfaces introduces artificial compliance to the mesh, which progressively increases as the mesh is refined and more interface elements are introduced. In a finite element formulation, the use of initially elastic interface elements may be viewed as imposing the displacement continuity at the element edges using a penalty method, which is known to undermine consistency of the discrete finite element weak formulation [10].

From equation (1.1), one may argue that the original stiffness of the bar may be recovered in the limit of $kh \to \infty$, which may be attained if $k \to \infty \ \forall h > 0$. However, other numerical issues arise when k is too large. In static problems or in dynamic problems with implicit time-stepping, a very large value of k may lead to ill-conditioning of the system of finite element equations to be solved during iterations [48]. In explicit time-stepping, on the other hand, too large values of k put extremely severe restrictions on the critical time step size Δt_{cr} defined by the Courant-Friedrichs-Lewy (CFL) condition [35] as

$$\Delta t \leq \Delta t_{\text{cr}} = \min\left(h\sqrt{\frac{\rho}{E}}, h\sqrt{\frac{\rho}{kh}}\right), \tag{1.2}$$

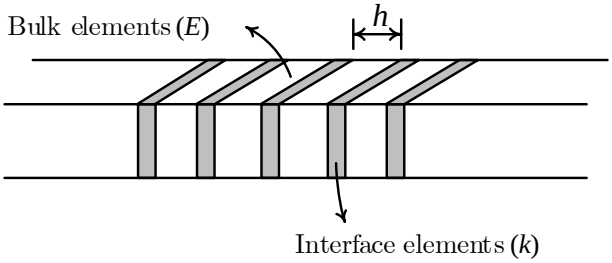

Figure 1.4: Schematic of a one-dimensional bar with elastic interfaces

in which ρ is the material density. One can verify that for finite $h > 0$, $\Delta t_{\text{cr}} \to 0$ as $k \to \infty$. Another issue arising from the use of a large initial stiffness k is traction oscillations along interface elements [144]. A common strategy to alleviate this problem has been to employ reduced Lobatto or trapezoidal integration for the interface elements which is, however, shown to not work well in many cases [157]. The reason is that initially elastic interface elements share stability properties with equivalent mixed-mode formulations (i.e., the use of Lagrange multipliers for enforcement of the constraint), hence exhibiting oscillations due to the violation of the inf-sup Ladyzhenskaya-Babuka-Brezzi condition [23].

It has been shown that the artificial compliance introduced by the initial stiffness of the cohesive model leads to dependence of the crack paths on the orientation of the elements [178, 177, 143]. In their initial simulations, Xu and Needleman [177] reported that, for a structured triangular mesh, the crack advances in a straight path when the triangles are oriented at $\pm 45^\circ$ and $\pm 60^\circ$ whereas it propagates in a zig-zag fashion when the triangles are oriented at $\pm 15^\circ$ and $\pm 30^\circ$. In fact, the initially elastic interface elements give rise to anisotropy in the FE mesh, which is dependent on the mesh configuration, thus introducing a nonphysical mesh sensitivity. Another issue caused by artificial compliance is the partial transmission and reflection of stress waves across interface elements in the mesh [45, 129]. In consequence, initially elastic models may fail to predict the formation of cracks due to underprediction of the magnitude and speed of the stress waves in the solid body. Rodovitzky et al. [129] reported that an initially elastic model failed to predict the spall of an elastic bar subjected to axial impulsive loading.

1.3.2 Extrinsic models: the issue of time-discontinuity

Suppose that a spatial discretization of the solid body is carried out using the FEM. The spatially discretized model yields a system of ordinary differential equations with unknown $\mathbf{U}(t)$, the vector of nodal displacements, expressed as

$$\mathbf{M}\ddot{\mathbf{U}}(t) + \mathbf{F}_{\text{int}}(\mathbf{U}, \boldsymbol{\kappa}) - \mathbf{F}_{\text{ext}} = \mathbf{0}, \tag{1.3}$$

in which $\mathbf{M}$ is the (consistent or lumped) mass matrix, $\mathbf{F}_{\text{int}}$ is the internal force vector, $\mathbf{F}_{\text{ext}}$ is the vector of external forces, and $\boldsymbol{\kappa}$ is a vector of history variables. The above equation is said to be time-continuous if $\mathbf{F}_{\text{int}}$ is a continuous function of $\mathbf{U}$ for all $(\mathbf{U}, \boldsymbol{\kappa})$ encountered on its solution trajectory [117]. Note that as equation (1.3) is already spatially discretized, spatial continuity is not relevant here.

As a result of time discontinuity, solution of an initial value problem (IVP) may not

exist or may be nonunique. Consider, for example, the following IVP [117],

$$\frac{du(t)}{dt} = f(u), \quad u(0) = 0 \tag{1.4}$$

with $f(u)$ a discontinuous function of u defined as,

$$f(u) = \begin{cases} -1 & u \geq 0 \\ 1 & u < 0. \end{cases} \tag{1.5}$$

The solution to the above IVP is plotted in Figure 1.5, showing that no solution exists for $t > 0$. An attempt to solve this IVP numerically, e.g., with a finite difference scheme, results in a solution that oscillates around $u = 0$. If, as another example,

$$f(u) = \begin{cases} 1 & u > 0 \\ 0 & \leq 0, \end{cases} \tag{1.6}$$

the IVP would not have a unique solution, e.g., the following function could be a solution to the IVP for any choice of t_1,

$$u(t) = \begin{cases} 0 & 0 \leq t \leq t_1 \\ t - t_1 & t > t_1. \end{cases} \tag{1.7}$$

The numerical solution of this ill-posed IVP would be sensitive to small perturbations, which would cause one or the other solution to be selected. It should be noted that discontinuity in $\mathbf{F}_{\text{ext}}$ does not raise any of the issues caused by discontinuity in $\mathbf{F}_{\text{int}}$. For

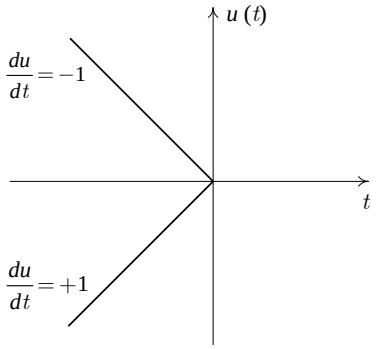

Figure 1.5: The solution to the IVP Equation (1.4) with discontinuous $f(u)$ Equation (1.5)

instance, the differential equation $du/dt = f$ in which f is a discontinuous function of t, has a unique solution that can be easily found numerically or analytically [117].

Initially-rigid cohesive zone models based on adaptive insertion of displacement discontinuities are time-discontinuous [117, 140], that is, the internal force vector $\mathbf{F}_{\text{int}}$ in equation (1.3) is a discontinuous function of the deformation $\mathbf{U}$ at the time a crack is inserted. The reason is that there is an infinite locus of possible component values of the force vector at an interface point that satisfy the crack propagation criterion at the time of inserting the displacement discontinuity. Whereas prior to activation the internal force vector is computed from the bulk elements adjoining the interface, after activation it is computed from the cohesive traction-separation model. Both vectors satisfy the scalar damage initiation criterion but they are different, thus leading to a discontinuity of the internal force vector. In a class of initially-rigid models that rely on an effective crack opening displacement defined as a norm of the opening displacement, such as the one proposed in [113], a more challenging form of time-discontinuity is encountered, in which the cohesive force vector is not defined at damage nucleation (i.e., zero effective displacement discontinuity) due to division by zero [117]. Time-discontinuity is not an issue specific to the interface element method. Discretization schemes based on the XFEM, in which the displacement discontinuities are modelled by introducing additional enrichment degrees of freedom rather than duplicating the existing nodal points, are time-discontinuous for similar reasons.

Time-discontinuity results in several numerical issues including presence of nonphysical shocks [95, 154], lack of convergence in the error norm as the time step and mesh is refined [140, 117], over-activation of interfaces [147, 140], nonphysical velocity fields [73, 95], and inability to perform implicit time-stepping [72, 161, 101]. Remedies proposed to achieve time-continuity typically rely on "encoding" knowledge of the interface stress or opening displacement immediately prior to activation into a modified cohesive traction-separation model. Among these remedies one can name a material strength that is a variable parameter computed at the time of crack nucleation [117, 153, 166], an offset of the interface opening at activation [140, 167, 72], and a correction force vector added to the enrichment degrees of freedom [95, 154]. Such remedies are not always grounded in physical reasoning. For example, there is no basis for asserting that the interface can "remember" its traction at the time of failure. However, they are of theoretical interest since they validate the assertion that time-discontinuity causes the pathological behaviours mentioned above.

Time-discontinuity of extrinsic cohesive zone models introduces challenges in obtaining convergence in implicit time integrators due to the interference of crack propagation criteria with Newton's iterations. Many researchers have simply sought to circumvent these challenges either by using explicit time integrators or by dealing with crack propagation at the

end of the implicit step. In the latter case, which has been particularly prevalent in XFEM implementations, cracks are kept fixed within the computations of the Newton solver. Once convergence is achieved, a stress criterion is checked at the crack-tip to answer the binary question of whether or not the crack should advance. While crack propagation angle may be determined by using, for example, the maximum hoop stress direction criterion [44], the crack advancement length is often taken to have a pre-determined value, e.g., the size of a generic element in the crack-tip area [99], or is determined by a Paris-type fatigue law [100]. Among the very few authors who have proposed intricate time-stepping schemes for discrete fracture is Areias and coworkers [6, 4]. These authors combine discrete equilibrium equations with the cohesive traction-separation model to form a nonlinear complementarity problem. An implicit solution is then made possible through smoothing of the complementarity conditions, leading to a mixed formulation with displacements and cohesive forces as unknowns. A certain level of approximation is thus introduced due to smoothing. In addition, these works make no attempt to address the question of time-continuity.

Computational modelling of fracture using an extrinsic cohesive zone model relies entirely on a Newtonian mechanics approach, i.e., equilibrium equations used for describing motion of the body along with fracture criteria describing evolution of displacement discontinuities (cracks). Continuity of stresses is in general hard to achieve in these computational models. A more recent development that can completely resolve the time-discontinuity issue is the energy approach to cohesive fracture [116, 91], which will be discussed in Section 1.6.

1.4 Mesh dependence: crack path and length convergence

Defining element edges as potential crack sites enables modelling complex failure patterns in a straightforward manner. Branching, fragmentation and coalescence of cracks are often natural outcomes of the method. However, the method introduces a certain degree of mesh dependence as mentioned previously. Supposedly, mesh refinement can alleviate this issue by providing more potential sites of crack nucleation and propagation in the mesh. In fact, accurate results have been reported in the literature by using sufficiently refined meshes, see e.g., [129, 105, 182, 120] among others. Besides mesh refinement, methods proposed in the literature to resolve mesh dependence more rigorously include employing special families of meshes possessing the isoperimetric property, adaptive strategies involving remeshing and realignment of the element edges during the simulation, and the XFEM and its variants.

1.4.1 The isoperimetric property and pinwheel meshes

For spatial convergence, element edges need to represent the true crack, including its length, as the mesh is refined. The length of the true versus approximated crack path is physically signicant because a fundamental assumption of cohesive crack models is that the energy needed to create a crack is proportional to its length. However, convergence of the crack path does not guarantee convergence of the crack length. Indeed, failure of length to converge is the typical behaviour for any family of structured meshes. For example, consider the cross-quadrilateral mesh with aspect ratio 1:1 shown in Figure 1.6 and assume that the true crack path is the line segment connecting the upper-left and lower-right corners of the domain. It can be shown that no matter how much the mesh is refined, the best approximation to the crack path (which is not uniquely determined) is a jagged line that is always longer than the correct path by approximately %8 [118].

Papoulia et al. [118] pointed out that there is one family of triangulations known to have the above convergence property in 2D, namely, pinwheel tiling. Pinwheel tiling possesses the "isoperimetric" property that for any line segment (p, q) and for any $\epsilon > 0$, there exists a triangulation $\mathcal{T}_i$ such that the shortest (p, q) path approximated using only edges of $\mathcal{T}_i$ has length $\|p - q\| + \epsilon$ [118]. The pinwheel tiling starts with a $1\colon 2\colon \sqrt{5}$ right triangle (Figure 1.7a) and subdivides it into five $1\colon 2\colon \sqrt{5}$ subtriangles that are similar to each other. This subdivision process may be repeated indenitely, yielding a tiling of the original triangle with an arbitrary level of renement. To change the tiling into a mesh suitable for finite element computations, one can remove hanging nodes in the tiling by splitting all the $1\colon 2\colon \sqrt{5}$ triangles at the final recursion level of the tiling into three (Figure 1.7b). The generalization of the pinwheel tiling to arbitrary triangles (not only $1\colon 2\colon \sqrt{5}$) has been proposed in [55]. Pinwheel meshes converge slowly (in terms of crack paths) and are not easy to generate except for the simplest domain geometries. In addition, generating meshes that posses the isoperimetric property in 3D is not a trivial task [118].

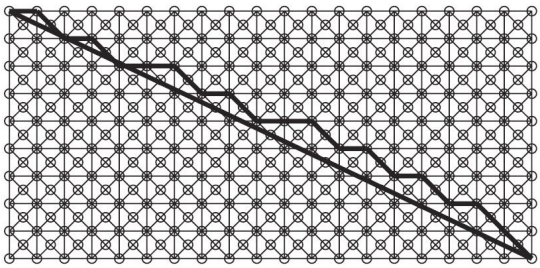

Figure 1.6: An example of failure in crack length convergence (reproduced from [118])

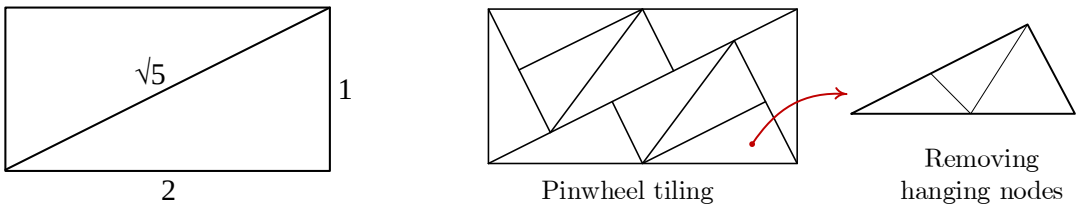

(a) (b)

Figure 1.7: Generation of isoperimetric meshes based on pinwheel tiling

1.4.2 Adaptive re-meshing methods

Paulino et al. [122] proposed node perturbation and edge-swap operators to address biased mesh orientation in structured **4k** meshes. These operators lead to geometrically and topologically unstructured meshes, as summarized in Figure 1.8. Numerical results reported in [122] showed improved spatial convergence; however, no formal proof of convergence in the sense described in Section 1.4.2 exists for these schemes. The same authors combined NP and ES operators with adaptive mesh refinement and mesh coarsening schemes for improved spatial convergence [121]. Further, Lew and coworkers [131] proposed "universal meshes," a technique to create conforming triangulations of the domain by only perturbing nodes of a background universal mesh in the vicinity of the crack. In this method, the crack propagation angle is determined explicitly using, for example, the maximum circumferential stress criterion [44]. In the context of LEFM, adaptive remeshing is often used in conjunction with *a posteriori* error estimates to refine the new mesh in the crack-tip area, see e.g., [78].

Remeshing can be difficult and computationally expensive especially in dynamic fragmentation and multiple crack growth simulations, in which the mesh typically needs to be

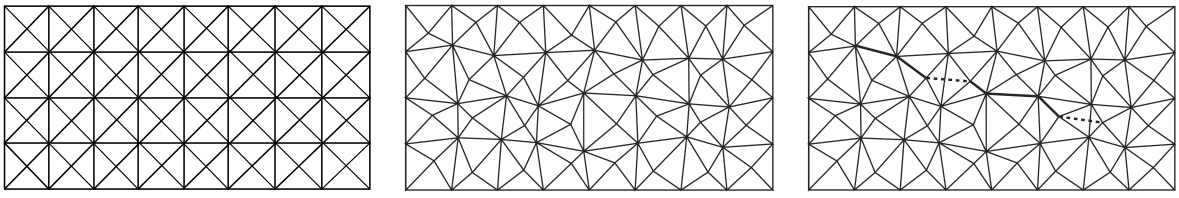

(a) the initial **4k** mesh (b) the NP operator (c) the ES operator

Figure 1.8: NP and ES operators applied to an initially structured mesh [122]

updated numerous times during the course of the simulation. Mota et al. [103] showed that the computational complexity of mesh topology modification algorithms could in fact be exorbitant, ($\mathcal{O}(n^{1.9})$, where n is the number of interface elements) and proposed an insertion scheme which is of order $\mathcal{O}(n)$. In addition, remeshing requires projection of the solution fields from the old mesh to the new. Even with excellent projection schemes, significant discontinuities can be introduced in the velocity, stress and displacement fields, which can further deteriorate the time-continuity of the model. Lastly, adaptive insertion of interface elements makes the application of scalable parallel computational schemes, necessary for problems of increasing size, very difficult [129]. The issue comes forth by noting that mesh refinement is critical for mitigating mesh dependence of the results and for resolving the size of the CPZ which could be extremely small in brittle materials.

1.4.3 Interface elements vs. XFEM

As pointed out previously, the XFEM, pioneered by Belytschko and coworkers [99, 100], can model cracks independent from the element edges by allowing the cracks to pass through within the elements. This is normally achieved by enriching the approximate solution space by discontinuous basis functions (e.g., the Heaviside function) on the basis of the partition of unity method [94].

In XFEM, crack surfaces are tracked explicitly using level set methods [156]. This can be an intractable task, particularly for problems involving multiple cracks and fragmentation. In fact, XFEM modelling of dynamic crack propagation inevitably requires a branching criterion, which can be quite ad-hoc and is mostly limited to two crack branches, see e.g., [38, 8]. Methods proposed to overcome this limitation of XFEM include the cohesive segment method of Remmers et al. [134] and the cracking node method of Belytschko and coworkers [153, 128]. In these methods, cracks are represented by a set of overlapping segments as illustrated in Figure 1.9. Convergence of the crack length in the sense discussed in Section 1.4.2 thus remains an open question in these methods.

Numerical implementation of XFEM algorithms often involves "hidden" tolerances. One example of this is the case, in which the crack crosses (or, is too close to) a nodal point of the mesh and, as a result, a singular system of finite element equations is encountered. The commonplace practice for resolving this issue is to introduce a minimum distance tolerance that determines whether or not the cut node should be enriched [42]. Another example of such hidden tolerances encountered in the cracking node method [153] is a set of minimum distance criteria introduced to avoid injection of spurious parallel crack segments in problems involving multiple cracks and fragmentation. In general, the XFEM appears to be best suited for modelling one or a small number of dominant cracks.

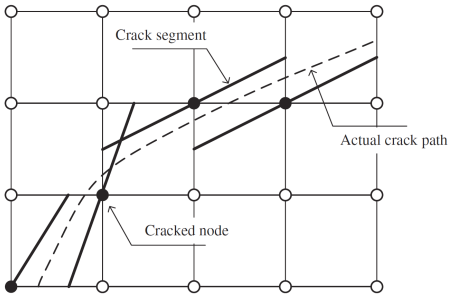

Figure 1.9: Schematic of a typical arrangement of crack segments to represent the true crack in the cracking node method [153]

1.5 Discontinuous Galerkin method for cohesive crack modelling

In the discontinuous Galerkin method, the discrete finite element weak form is obtained by seeking an element-wise-continuous approximate solution (as opposed to the standard Galerkin formulations where a domain-wise-continuous approximation is sought) [89]. The continuity of the solution field at inter-element boundaries is then enforced weakly by making use of a method, due to Nitsche [107], which ensures consistency and stability of the finite element formulation.[1] Within the context of solid mechanics, the DG method has been sometimes referred to as the "interior penalty method" [9]. Among several applications, the Nitsche method has been used in [46] for boundary condition enforcement, in [51] for domain decomposition, in [173] for contact and in [69] for incompressible elasticity. Recently, the DG method has found application in cohesive zone modelling, which will be discussed in the following.

1.5.1 The discontinuous Galerkin weak form

Suppose that a finite element discretization Ω_h of a solid body is achieved and let $\partial\Omega_h$ denote the exterior boundary of the mesh. The mesh is subjected to traction $\widetilde{\mathbf{t}}$ on $\partial_t\Omega_h$ and displacement $\widetilde{\mathbf{u}}$ on $\partial_u\Omega_h$, where $\partial_t\Omega_h$ and $\partial_u\Omega_h$ are disjoint parts of $\partial\Omega_h$. Although the DG method does not require the finite element mesh to be conforming, we consider here, for simplicity, that the mesh is conforming. Let $\Gamma_{d,h}$ denote the union of all element edges in the

[1] We recall that consistency and stability of the finite element formulation are two requirements necessary for convergence of the finite element solution.

interior of the mesh and let the normal to $\Gamma_{d,h}$ be denoted $\mathbf{n}_d$. Neighbouring elements in the mesh do not share nodal points/edges, allowing for the insertion of interface elements along all inter-element edges of the mesh as shown in Figure 1.10. The approximate displacement field denoted $\mathbf{u}_h$ is element-wise continuous but exhibits a displacement jump $[\![\mathbf{u}_h]\!]$ on $\Gamma_{d,h}$ and satisfies $\mathbf{u}_h = \widetilde{\mathbf{u}}$ on $\partial_u \Omega_h$. The DG weak form can be written as [89]

$$\begin{aligned}\int_{\Omega_h} \rho\, \delta\mathbf{u}_h \cdot \ddot{\mathbf{u}}_h \, dV + \int_{\Omega_h} \boldsymbol{\sigma}_h : \delta\boldsymbol{\varepsilon}_h \, dV + \int_{\Gamma_{d,h}} [\![\delta\mathbf{u}_h]\!] \cdot \left(\langle \boldsymbol{\sigma}_h \rangle \, \mathbf{n}_d + \eta [\![\mathbf{u}_h]\!]\right) \, dS = \\ \int_{\partial_t \Omega_h} \delta\mathbf{u}_h \cdot \widetilde{\mathbf{t}} \, dS + \int_{\partial\Omega_h} \delta\mathbf{u}_h \cdot \mathbf{b} \, dV = 0,\end{aligned} \tag{1.8}$$

which must be satisfied for any admissible test displacement function $\delta\mathbf{u}_h$. The test function $\delta\mathbf{u}_h$ is approximated similarly to $\mathbf{u}_h$ except that $\delta\mathbf{u}_h = \mathbf{0}$ on $\partial_u \Omega_h$. In the above, $\boldsymbol{\sigma}_h$ is the Cauchy stress tensor computed strongly from the infinitesimal strain tensor $\boldsymbol{\varepsilon}_h = \nabla^s \mathbf{u}_h$, ρ is the material density, $\mathbf{b}$ is the vector of body forces per unit volume, and η is a strictly positive numerical parameter to be discussed shortly. The jump and average operators are defined as

$$[\![*]\!] = *^+ - *^- \quad \text{and} \quad \langle * \rangle = \frac{1}{2}(*^+ + *^-), \tag{1.9}$$

where

$$*^\pm = \lim_{\xi \to 0^+} *(\mathbf{x} \pm \xi \mathbf{n}_d), \quad \mathbf{x} \in \Gamma_{d,h}. \tag{1.10}$$

The above definition for the jump operator makes the choice for the direction of $\mathbf{n}_d$ immaterial as the value of $* \cdot \mathbf{n}_d$ remains unchanged when the direction of $\mathbf{n}_d$ is reversed. The DG weak form can be made symmetric by the introduction of additional terms to the

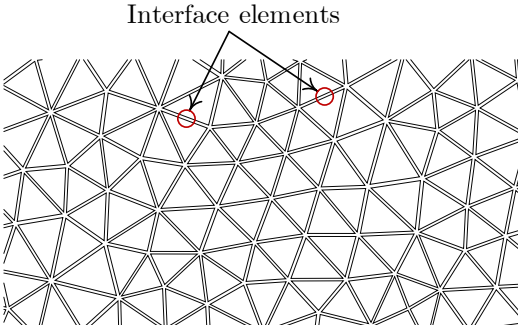

Figure 1.10: Interface elements in a DG mesh. The bulk elements are shrunk for better illustration

weak form (1.8). This, along with further details on its derivation, has been discussed in [89, 110] among others.

The interfacial traction $\langle \boldsymbol{\sigma}_h \rangle \, \mathbf{n}_d + \eta [\![\mathbf{u}_h]\!]$ appearing in the integral on $\Gamma_{d,h}$ in (1.8) is often referred to as the Nitsche traction, see e.g., [142]. The first term of the Nitsche traction ensures consistency of the finite element formulation. Were it not for this term, the formulation would correspond to a penalty formulation which gives rise to the complexities associated with artificial compliance discussed in Section 1.3.1 due to lack of consistency. The second term of the Nitsche traction is a penalization term introduced for the stability of the formulation. In linear elasticity, the penalty parameter η may be defined as

$$\eta = \chi \frac{\mu}{h_s}, \tag{1.11}$$

in which μ is the shear modulus, h_s is an element-wise measure of the mesh size, and $\chi > 0$ is a dimensionless parameter which must be greater than a minimum threshold dependent on the order of approximation to ensure stability [89]. Radovitzky et al. [129] suggested that the range $2 \leq \chi \leq 10$ leads to stable numerical results for quadratic approximations. The DG formulation was extended to finite deformation in [109]. Extension to dynamics was proposed in [111], where it was shown that the explicit stable time step is reduced by a factor of $1/\sqrt{\chi}$.

1.5.2 The hybrid DG-cohesive element method

The idea of using DG formulations in cohesive zone modelling was first proposed by Mergheim et al. [96], who modelled adhesive interfaces in two dimensions. In this work, the DG method was used only in the pre-failure state along a *a priori* known surface. At the onset of material failure, the DG formulation gives its place to an extrinsic cohesive zone model formulation describing the nonlinear fracturing processes until the formation of a traction-free interface. Radovitzky et al. [129] used a similar approach for modelling dynamic fracture in 3D by introducing the DG formulation in the entire finite element mesh. Thanks to the DG formulation, issues associated with the effect of artificial compliance discussed in Section 1.3.1 were effectively avoided. Because the method does not require adaptive insertion of elements, it is also readily amenable to scalable parallel computations [129]; see also [105] for more details on the numerical implementation of this method. Other applications of the DG method to cohesive crack modelling include the space-time DG approach proposed by Abedi et al. [1] and the cohesive interface formulation proposed by Hansbo and Salomonsson [70].

To switch from the DG formulation to the cohesive zone formulation, a binary variable α is defined that takes a value of zero before fracture and of 1 after fracture. The boundary integral on $\Gamma_{d,h}$ in (1.8) is replaced by

$$\int_{\Gamma_{d,h}} (1-\alpha)[\![\delta \mathbf{u}_h]\!] \cdot (\langle \boldsymbol{\sigma}_h \rangle \, \mathbf{n}_d + \eta [\![\mathbf{u}_h]\!]) \; dS + \int_{\Gamma_{d,h}} \alpha \, \delta \mathbf{u}_h \cdot \mathbf{t}_{\text{cohs}}([\![\mathbf{u}_h]\!]) \, dS, \tag{1.12}$$

in which $\mathbf{t}_{\text{cohs}}([\![\mathbf{u}_h]\!])$ is the cohesive traction computed from an extrinsic cohesive zone model. For an initially uncracked body, α is 0 everywhere on $\Gamma_{d,h}$ at the start of the simulation but becomes 1 anywhere and at any time a fracturing criterion is met and then remains constant. The fracturing criterion can be written for the cohesive zone model of, for example, Ortiz and Pandolfi [113] as

$$\sigma_{\text{eff}} = \sqrt{(\boldsymbol{\sigma}_h : [\mathbf{n}_d \otimes \mathbf{n}_d])^2 + \beta^{-2} (\boldsymbol{\sigma}_h : [\mathbf{I} - \mathbf{n}_d \otimes \mathbf{n}_d])^2} \geq \sigma_c \quad \rightarrow \quad \alpha = 1, \tag{1.13}$$

where σ_c is the material strength in tension and β is a constant of the cohesive zone model representing the ratio of the material strength in shear to that in tension.

The switch from DG to cohesive zone is performed at the quadrature point level, thus affording the possibility of sub-element crack resolution. When the faces of a cracked interface come into contact, i.e., when $[\![\mathbf{u}_h]\!] = \mathbf{0}$ and $[\![\dot{\mathbf{u}}_h]\!] < 0$, the nonpenetration constraint in the normal direction is enforced by using the normal component of the DG traction. In that case, the tangential response is still governed by the cohesive zone model. Radovitzky et al. [129] showed that the hybrid DG-cohesive element method is free of the artificial compliance effect and guarantees transmission of longitudinal waves in both the pre- and post-failure stages. However, as will be shown in the following, the hybrid DG-cohesive element method is still not time-continuous in its present form.

1.5.3 Attaining time-continuity

In this section, a preliminary method, based on Sam et al. [140], is presented for making the hybrid DG-cohesive element method time-continuous. Since time-continuity concerns the initiation of damage, introduction of a history variable that accounts for the irreversibilty of subsequent fracturing processes [113] is neglected in the presentation that follows.

Suppose that the fracturing criterion is met at an interface Gauss point at $t = t_0$. To assure time-continuity in the hybrid DG-cohesive zone method, one needs to have

$$\left\langle \boldsymbol{\sigma}_h^0 \right\rangle \mathbf{n}_d + \eta [\![\mathbf{u}_h^0]\!] = \mathbf{t}_{\text{cohs}}([\![\mathbf{u}_h^0]\!]), \tag{1.14}$$

in which the superscript 0 implies that the variables are evaluated at $t = t_0$. Note that since the DG method enforces displacement continuity only weakly, the interface shows a nonzero, albeit very small, displacement jump $[\![\mathbf{u}_h^0]\!]$ at the onset of fracture. This nonzero jump is a result of the numerical solution and does not represent a physical crack opening displacement. As discussed in Section 1.3.2, the above criterion is not guaranteed to hold in general. The basic idea of the method proposed by Sam et al. [140] is to start with an initially elastic cohesive zone model and apply a shift of the origin such that the cohesive traction for zero crack opening displacement matches the traction obtained from bulk stresses at interface activation. Consider a generic initially elastic cohesive model that represents the cohesive traction as a function $f(\boldsymbol{\delta})$ of the crack opening displacement $\boldsymbol{\delta}$. An *activation opening displacement* $\boldsymbol{\delta}_a$ is first defined such that

$$f(\boldsymbol{\delta}_a) = \left\langle \boldsymbol{\sigma}_h^0 \right\rangle \mathbf{n}_d. \tag{1.15}$$

Note that the activation opening displacement $\boldsymbol{\delta}_a$ is defined locally at the Gauss point level, i.e., each Gauss point on the interface has its own $\boldsymbol{\delta}_a$. A cohesive traction-separation model that can ensure time-continuity in (1.12) is now given by

$$\mathbf{t}_{\text{cohs}}([\![\mathbf{u}_h]\!]) = f(\boldsymbol{\delta} + \boldsymbol{\delta}_a) + \mathbf{p}_h^0 \xi(\delta_{\max}), \tag{1.16}$$

in which $\mathbf{p}_h^0 = \eta[\![\mathbf{u}_h^0]\!]$ is the penalty component of the Nitsche traction at crack nucleation and $\xi(\delta_{\max})$ is a decaying function of the maximum effective opening displacement attained in the loading history, $\delta_{\max}$, satisfying $\xi(0)$=1. The term $\mathbf{p}_h^0 \xi(\delta_{\max})$ is not present in the original work of Sam et al. [140] who modelled initially-rigid cohesive interfaces by adaptive insertion of interface elements rather than the present DG approach. The function $\xi(\delta_{\max})$ is thus introduced to phase out $\mathbf{p}_h^0$ with the opening of the interface to alleviate alteration of the original traction-separation model with the physically meaningless traction $\mathbf{p}_h^0$. A convenient choice for $\xi(\delta_{\max})$ would be the exponential form $\xi(\delta_{\max}) = e^{-a\delta_{\max}/\delta_c}$, where $a \gg 1$ is a constant that determines how fast the function decays. By taking, for example, $a = 300$, the function $\xi(\delta_{\max})$ decays to zero within machine precision once $\delta_{\max}$ reaches $0.1\delta_c$. The actual crack opening displacement $\boldsymbol{\delta}$ to be used in the evaluation of f is different from the displacement jump at the interface and is given by

$$\boldsymbol{\delta} = [\![\mathbf{u}_h]\!] - [\![\mathbf{u}_h^0]\!]. \tag{1.17}$$

With the above definition, one can verify that the condition (1.14) is satisfied by the cohesive model (1.16) at $[\![\mathbf{u}_h]\!] = [\![\mathbf{u}_h^0]\!]$.

Within a time discrete framework, t_0 does not necessarily coincide with any of the discrete time steps defined for time integration. Suppose the activation criterion (1.13) is

first satisfied at time step t_1. Let $t_2 = t_1 - \Delta t$ be the time step immediately prior to t_1. The activation time t_0 is taken to be an intermediate point between t_1 and t_2 determined by linear interpolation as

$$t_0 = A_1 t_1 + A_2 t_2, \tag{1.18}$$

where the interpolators $0 \leq A_1 \leq 1$ and $0 \leq A_2 \leq 1$ are given by,

$$A_1 = \frac{\sigma_c - \sigma^2_{\text{eff}}}{\sigma^1_{\text{eff}} - \sigma^2_{\text{eff}}} \quad \text{and} \quad A_2 = \frac{\sigma^1_{\text{eff}} - \sigma_c}{\sigma^1_{\text{eff}} - \sigma^2_{\text{eff}}}. \tag{1.19}$$

In the above, σ^1_{eff} and σ^2_{eff} are effective stresses obtained at t_1 and t_2, respectively. The variables $[\![\mathbf{u}^0_h]\!]$ and $\langle \boldsymbol{\sigma}^0_h \rangle$ needed for the computation of cohesive traction defined through equations (1.15)-(1.17) are interpolated in a similar manner as,

$$\begin{aligned} [\![\mathbf{u}^0_h]\!] &= A_1 [\![\mathbf{u}^1_h]\!] + A_2 [\![\mathbf{u}^2_h]\!], \\ \left\langle \boldsymbol{\sigma}^0_h \right\rangle &= A_1 \left\langle \boldsymbol{\sigma}^1_h \right\rangle + A_2 \left\langle \boldsymbol{\sigma}^2_h \right\rangle. \end{aligned} \tag{1.20}$$

Illustrative example. *Rectangular block with a weak interface* In order to validate the assertion that the modified cohesive model given by (1.16) corrects the pathological behaviour emanating from time-discontinuity, the mixed-mode failure of a weak interface shown in Figure 1.11 was analyzed numerically. Time integration was performed explicitly using the central difference scheme. Results of the temporal convergence study (Figure 1.11b) show that the time-continuous model exhibits the expected second order convergence rate at selected pre- and post-failure stages while the time-discontinuous model shows very poor convergence or no convergence at all in the post-failure stage. In addition, the velocity contours obtained by the two methods, shown in Figure 1.12, clearly indicate that the time-continuous model resolves the pathological behaviour observed in the time-discontinues model. It must be noted this pathological behaviour is different than shock waves induced due to external shock forces. In addition, the spurious irregularities do not go away with mesh or time step refinement.

Finally, it is worth mentioning that even though the cohesive traction (1.16) makes the hybrid DG-cohesive element approach time-continuous, the method is still not amenable to implicit time-stepping. In particular, it was found that a Newton-Raphson iteration for the solution of the nonlinear system of equations fails to converge at crack activation in many cases. Failure to converge is typically due to an oscillatory behaviour between cracked (cohesive zone model formulation) and uncracked (DG formulation) conditions. It thus appears that the hybrid DG-cohesive element method is best suited for dynamic problems and explicit time-stepping.

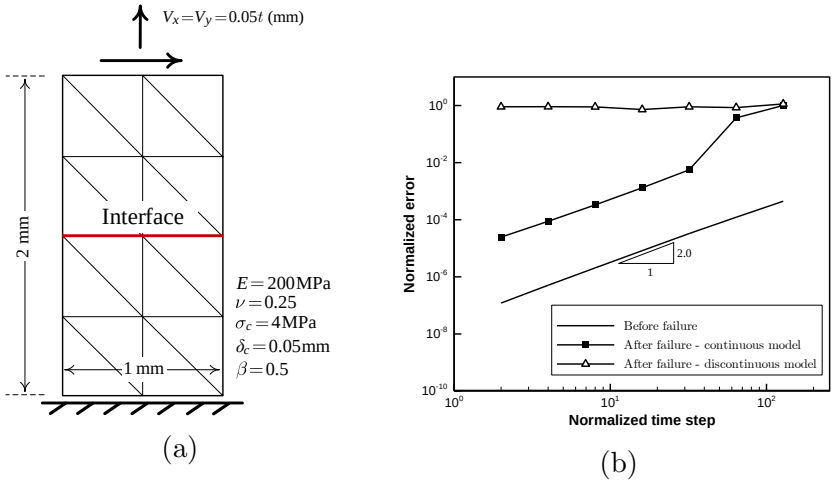

(a) (b)

Figure 1.11: Rectangular block with a weak interface; a) problem definition, boundary conditions and the FE mesh, b) results of the temporal convergence study

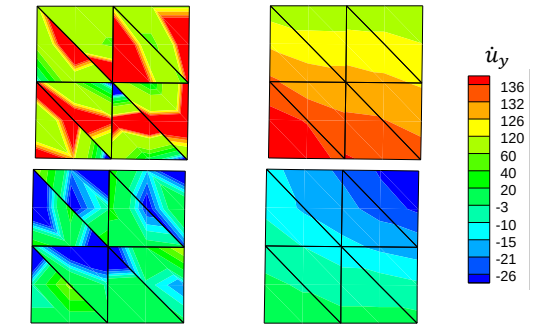

Figure 1.12: Contours of the vertical velocity field obtained by the time-continuous and time-discontinuous hybrid DG-cohesive element methods (color bar in mm/s)

1.6 Energy approaches to fracture

In Griffith's LEFM theory [66], the elastic energy release rate G induced by the infinitesimal growth of an existing crack-tip along a *a priori* known path is compared to a critical energy rate G_c and propagation occurs when $G = G_c$. Even though fracture mechanics, as proposed by Griffith [66], is solidly based on energy methods, early works in com-

putational fracture mechanics, including those reviewed in the preceding sections, have generally favoured a Newtonian approach, i.e., balance of forces, along with crack propagation criteria (in the discrete approach) or with damage evolution laws (in the smeared approach). However, energy approaches to fracture have gained big interest in recent years. Francfort and Marigo [49] expanded Griffith's energy theory by formulating brittle fracture as an energy minimization problem that simultaneously seeks the displacement field and the crack path, represented as a set valued variable, that minimize the sum of the bulk and surface dissipated energies in the loaded body. This has been the core idea idea of energy (variational) approaches to fracture, see also [30]. In the context of LEFM, numerical implementation of the energy approach has been achieved by representing the cracks as a "phase field" [20]. In the context of cohesive fracture, the energy approach has been formulated as a nondifferentiable energy minimization problem [116, 91]. An important difference between the two approaches is that the first leads to a smeared crack whereas the second is a discrete cohesive crack approach. In what follows, each of these methods are briefly discussed.

1.6.1 Crack as a phase field

In the spirit of the variational approach to brittle fracture [49], deformation and fracture of a solid body Ω containing an evolving crack $\mathcal{S}$ is formulated by the minimization of its potential energy functional π expressed, in the absence of inertial effects and external forces, as

$$\pi(\boldsymbol{\varepsilon}, \mathcal{S}) = \int_{\Omega \backslash \mathcal{S}} \psi(\boldsymbol{\varepsilon})\, dV + \int_{\mathcal{S}} G_c\, dS, \tag{1.21}$$

where ψ is the strain energy density function represented as a function of the strain tensor $\boldsymbol{\varepsilon} = \nabla^s \mathbf{u}$ and G_c is the (constant) fracture energy. Note that the displacement field $\mathbf{u}$ is continuous everywhere in $\Omega \backslash \mathcal{S}$ except for discontinuities across the unknown crack surfaces $\mathcal{S}$.

Numerical implementation of the energy formulation in this context was achieved by Bourdin et al. [20], who approximated the original functional by an elliptic functional, in which an additional "phase field" was introduced that regularizes the sharp crack surface into a diffuse zone and interpolates between the unbroken and the broken state of the material. The above functional is approximated by $\widetilde{\pi}$ as [20]

$$\widetilde{\pi}(\boldsymbol{\varepsilon}, d; \nabla d) = \int_\Omega g(d)\psi(\boldsymbol{\varepsilon})\, dV + \frac{1}{c_0}\int_\Omega G_c \left[\frac{1}{l_0} w(d) + l_0(\nabla d \cdot \nabla d)\right] dV, \qquad \text{with} \quad c_0 = 4\int_0^1 \sqrt{w(s)}\, ds. \tag{1.22}$$

in which $0 \leq d \leq 1$ is a new unknown, the phase field, taking a value of 1 close to $\mathcal{S}$ and 0 away from it, and l_0 is a numerical parameter that controls the width of the diffuse region. Furthermore, $w(d)$ is a function characterizing the local part of the dissipated energy, which could be taken as $w(d) = d$ or $w(d) = d^2$; $g(d)$ is a monotonically decreasing *stiffness degradation function* of d with $g(0) = 1$ (no damage) and $g(1) = 0$ (complete loss of stiffness). More details on different forms of $g(d)$ and its effect on the numerical results along with a recent review on phase field modelling of fracture can be found in [93]. A variational formulation using the regularized potentials (1.22) leads to an equilibrium equation governing the bulk deformation and an additional equation governing the evolution of the phase field.

The phase field method leads to a smeared crack whose thickness, however, is controlled by l_0 so the method is free of the several issues, such as mesh dependence, that plague conventional damage mechanics. It has been shown that the approximate functional (1.22) converges to the original functional (1.21) as $l_0 \to 0$ in a Γ-convergence sense[2] [20]. However, phase field models inherit the deficiency of Griffith's theory in the limit because they predict crack nucleation at a critical stress inversely proportional to the square root of l_0 [18]. Therefore, l_0 is may be regarded as a material property that should be fixed for a specific problem as in gradient-damage models [127]. More recently, phase field methods have been extended to the case of cohesive fracture, see e.g., [106, 62]. These models differ from a Barenblatt description of cohesive fracture (i.e., an opening-dependent fracture energy functional as in Section 1.6.2); rather, they build on the work of Lorentz et al. [92] who derived the cohesive zone behaviour as the asymptotic response of a nonlocal damage model associated with a particular stiffness degradation function $g(d)$. In consequence, in these models, the length scale l_0 is no longer a material constant but a purely numerical parameter. Phase-filed formulations of fracture are thus closely related to gradient/nonlocal damage models of continuum damage mechanics even though they are entirely based upon an energy description of discrete brittle fracture.

[2] Γ-convergence is a notion of variational convergence that implies convergence of minimizers.

1.6.2 Nondifferentiable energy minimization for cohesive fracture

In the context of cohesive fracture model, the energy functional of the fracturing body is expressed as

$$\pi(\boldsymbol{\varepsilon}, \mathcal{S}) = \int_{\Omega \setminus \mathcal{S}} \psi(\boldsymbol{\varepsilon})\, dV + \int_{\mathcal{S}} \psi_{\text{cohs}}(\llbracket \mathbf{u} \rrbracket)\, dS, \tag{1.23}$$

where ψ_{cohs} is the cohesive surface energy density function which, according to Barenblatt's cohesive crack model [11], depends nontrivially on the displacement jump $\llbracket \mathbf{u} \rrbracket$ across the unknown discontinuity surface $\mathcal{S}$. On the basis of the variational approach to fracture, Charlotte et al. [30, 29] and Bourdin et al. [21] showed that nondifferentiablity of ψ_{cohs} at zero displacement jump is the necessary requirement for obtaining a stress criterion for the initiation of cracks (i.e., nonzero displacement jump at finite stresses) as a result of the loss of stability of the elastic response. This was also shown in 1D earlier on by DelPiero [39]. In the above, fracturing processes are assumed to be reversible for simplicity of presentation. Irreversibly can be modelled by introducing a history variable as described, for example, in [113].

It is noted that a phase field approximation to the functional (1.23) would not be possible as the surface energy function ψ_{cohs} is not a constant parameter but an opening dependent function. Numerical implementation of the above energy formulation can, however, be achieved by restricting the evolution of crack surfaces $\mathcal{S}$ to a set of *a priori* known boundaries Γ_d. As Γ_d represents potential sites of crack nucleation and propagation, the displacement field is allowed to be discontinuous everywhere across Γ_d, and a new variable $\boldsymbol{\delta}$ is introduced that represents the magnitude of the displacement jump on Γ_d. The potential (1.23) is rewritten as

$$\widetilde{\pi}(\boldsymbol{\varepsilon}, \boldsymbol{\delta}) = \int_{\Omega \setminus \Gamma_d} \psi(\boldsymbol{\varepsilon})\, dV + \int_{\Gamma_d} \psi_{\text{cohs}}(\boldsymbol{\delta})\, dS, \tag{1.24}$$

which should now be minimized subject to the constraint $\llbracket \mathbf{u} \rrbracket = \boldsymbol{\delta}$ on Γ_d. Numerical implementations of initially-rigid interfaces using a formulation similar to the above has been proposed by Lorentz [91] and Papoulia [116]. Consistent with earlier findings in [30, 29, 21], both authors pointed out that the initially-rigid behaviour across the interfaces is associated with the nondifferentiability of the cohesive potential ψ_{cohs} at zero interface opening. The usual step of passing to a weak form thus does not apply in such formulations as the objective functional is not globally differentiable. Instead, methods corresponds to a constrained nondifferentiable energy minimization problem. Because crack nucleation happens

automatically as a result of energy minimization, these methods completely sidestep the complexities arising from the use of an extrinsic failure criterion in previous stress based formulations (see Section 1.3.2). However, the need arises for a solution method able to handle the nondifferentiability. Whereas Lorentz [91] used a generalized definition of the derivative at the nondifferentiable point, Papoulia [116] proposed a continuation method with successive smoothing of the cohesive surface energy function ψ_{cohs}.

A major difference between the numerical implementations proposed in [91, 116] and that of phase field is that the former preserve the discrete nature of fracture and are thus able to model the opening of cracks and associated post-failure mechanisms. A sharp representation of the crack in phase field models must be determined *a posteriori* or, alternatively, by coupling the method with an algorithm that allows transition of diffuse damage to sharp crack faces, see e.g., [61].

To demonstrate the role of nondifferentiability, consider the simple one-dimensional model shown in Figure 1.13a proposed by Papoulia [116]. Let δ_s and δ_i denote the deformation of the spring and the opening of the interface, respectively. The displacement compatibility constraint is $\delta_i + \delta_s = \Delta$, where Δ is an externally applied displacement. Let $\psi_s(\delta_s)$ and $\psi_i(\delta_i)$ denote the energy functions associated with the spring and the interface, respectively, and suppose that the total potential energy of the system, π, is the sum of

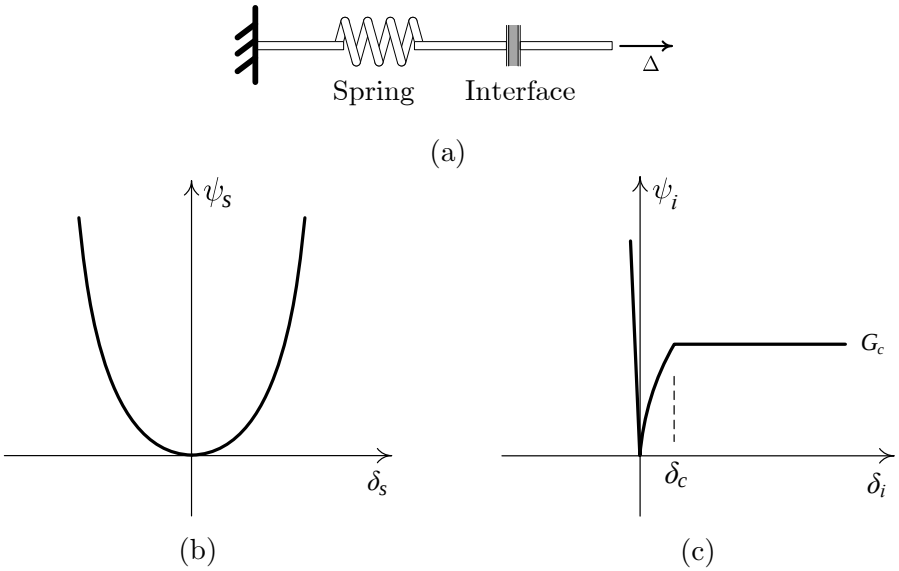

Figure 1.13: a) the one-dimensional model of a spring and a cohesive interface, b) potential energy of the spring, c) potential energy of the interface

these two potentials, $\pi(\delta_s, \delta_i) = \psi_s(\delta_s) + \psi_i(\delta_i)$. The potential of the spring is the classical quadratic $\psi_s = k\delta_s^2/2$, where k is the spring constant, see Figure 1.13b. That of the interface can be written for a linear softening relationship as

$$\psi_i(\delta_i) = \int_0^{\delta_i} \sigma_c \left(1 - \frac{\delta}{\delta_c}\right) d\delta = \sigma_c \delta_i - \frac{1}{2}\frac{\sigma_c}{\delta_c}\delta_i^2, \tag{1.25}$$

for $0 \leq \delta_i \leq \delta_c$, followed by a constant $G_c = \sigma_c \delta_c/2$ for $\delta_i \geq \delta_c$ (i.e., complete loss of cohesion), see Figure 1.13c. For $\delta_i < 0$, the interface potential is written as $\psi_i = -c\delta_i$, which, with $c \gg 1$ being a large penalty parameter, implies that a high value of compressive traction will act to impose a zero interpenetration constraint when $\Delta < 0$. At $\delta_i = 0$, the slope of ψ_i is σ_c on the positive side of δ_i and $-c$ on the negative side of δ_i. The equilibrium configuration of the spring-interface system is denoted $(\delta_i^\star, \delta_s^\star)$, the minimizer of the total energy functional, that is,

$$(\delta_i^\star, \delta_s^\star) = \text{argmin}\left\{\pi(\delta_i, \delta_s) = \psi_i(\delta_i) + \psi_s(\delta_s)\right\} \quad \text{s.t.} \;\; \delta_i + \delta_s = \Delta. \tag{1.26}$$

It can be shown that the configuration $(\delta_i^\star = 0, \delta_s^\star = \Delta)$ is one such minimizer [116]. To this end, the derivatives to the left and to the right of $\delta_i = 0$ can be easily evaluated, with $\delta_s = \Delta$, as

$$\begin{aligned} \frac{\partial \pi}{\partial \delta_i}(0^+, \Delta) &= -k\Delta + \sigma_c \\ \frac{\partial \pi}{\partial \delta_i}(0^-, \Delta) &= -k\Delta - c, \end{aligned} \tag{1.27}$$

of which the second is always negative for $\Delta > 0$ and the first is positive for small Δ. A well-known theorem in nonsmooth optimization, specialized to the univariate case, states that if $\pi(x)$ is a real-valued function such that its left-derivative $\pi'(x_0^-)$ and its right-derivative $\pi'(x_0^+)$ both exist at a point x_0 and if $\pi'(x_0^-) < 0$, $\pi'(x_0^+) > 0$, then x_0 is a local minimizer of π. Accordingly, it can be argued that for small values of Δ, of either sign, the minimum is attained when $\delta_i = 0$, i.e., the interface remains exactly at zero opening displacement. This is possible because ψ_i' jumps discontinuously from a negative to a positive value at $\delta_i = 0$, i.e., ψ_i is not differentiable at the origin. In contrast, one can verify that if ψ_i were differentiable at $\delta_i = 0$, then any small value of Δ would lead to a nonzero minimizer $\delta_i^\star \neq 0$ [116].

1.7 Motivation, objectives and methodology

As with many other physical phenomena, computational modelling of fracture constitutes an indispensable tool not only to predict failure of cracked structures but also to provide an ever-closer understanding of fracture process mechanisms. Robustness issues in existing methods of discrete fracture have led to many of the algorithmic pitfalls and nonphysical solutions discussed in previous sections. The demands for obtaining reliable simulation results in engineering applications motivates development of new computational methods. In particular, the newly proposed methods need to deliver the following properties:

- *Preserve the discrete nature of fracture* Methods that smear crack faces over a narrow region, such as methods of continuum damage or phase field methods, are not pursued in this research. A distinct advantage of the sharp crack approach is that it is able to model the opening of cracks and associated post-failure mechanisms. This is especially useful in coupled multi-physics problems, in which additional unknowns, defined locally along the crack faces, are explicitly dependent on the crack opening field (e.g., hydraulic fracturing).

- *Be free of nonphysical parameters* Regularization parameters such as the initial stiffness k of intrinsic cohesive models (Section 1.3.1) or the activation opening $\boldsymbol{\delta}_a$ in "shifted" initially-rigid models (Section 1.5.3) have no rigorous mathematical or physical grounds and undermine robustness of the numerical algorithm. Methods should be free of such parameters.

- *Time-continuity* The continuity of the internal forces as a function of deformation should be preserved throughout the solution trajectory including at initiation of damage. As discussed in Section 1.3.2, this is crucial to the mathematical soundness of the computational algorithm. Methods that rely on an external fracture criterion violate this condition and are therefore not pursued in this research.

- *Be amenable to both quasi-static and dynamic problems* In addition to explicit time-stepping, which is best-suited for fast dynamic problems, methods should be applicable with implicit time-stepping to address problems with slow/quasi-static loading. As discussed in Section 1.5.3, time-continuity is not always sufficient to make implicit time-stepping possible. Methods that switch from one formulation to another at crack activation (e.g., from DG to cohesive element) are likely to result in non-convergence of nonlinear Newton-Raphson solvers due to an oscillatory behaviour between "cracked" and "uncracked" conditions.

- *Be capable of handling multiple cracks* In conventional engineering fracture mechanics, crack growth is assumed to occur by extension of a single dominant crack. However, a wide variety of circumstances exists in which the fracture process involves nucleation and growth of multiple cracks, fragmentation, bifurcation of cracks or micro-crack branching. Numerical methods are expected to offer a desirable flexibility in modelling these phenomena while producing accurate crack trajectories.

Recognizing these needs, several computational algorithms have been proposed in this research by pursuing and advancing the nondifferentiable energy minimization approach to cohesive fracture discussed in Section 1.6.2. For reasons mentioned earlier - notably the lack of an explicit activation criterion - the nondifferentiable energy minimization approach is a firm basis for developing robust computational algorithms for modelling initially-rigid interfaces. To demonstrate that the newly proposed algorithms deliver the properties mentioned above, the following strategies have been employed in this research where appropriate:

- *Temporal and spatial convergence studies* Convergence tests provide reliable means of examining the mathematical soundness and robustness of the newly proposed algorithms. This is especially true in dynamic crack propagation problems where there are limited, if any, analytical solutions available, against which numerical solutions may be verified. For spatial convergece, methods should not only exhibit expected rates of convergence in the error norms, but also produce convergent crack paths and lengths (i.e., convergence in dissipated fracture energies).

- *Verifying numerical results against experimental findings* The predictive capabilities of the numerical models can be examined by making comparisons with several experimental data reported in the previous literature. In particular, comparisons are made with crack trajectories, load-displacement curves and crack-tip velocities when such data is available. Experimental data are obtained from the literature. Experiments were not conducted as part of this research.

- *Solving multi-physics problems* Many real-world problems involve several interacting physical phenomena. Application of the methods to such problems exposes them to new simulation challenges and examines their capabilities in modelling more complex problems. An example of multi-physics problems involving fracture is hydraulic fracturing, in which cracks are driven by the injection of a fracturing fluid.

1.8 Statement of contributions

Chapter 2 of this dissertation consists of a paper published in *International Journal for Numerical Methods in Engineering* (2018) 115:627-650. The paper was co-authored by myself and my supervisor, Dr. Katerina Papoulia. In this paper, I developed the relevant mathematical and computational techniques, implemented a computer program to perform the numerical simulations and wrote the manuscript. Dr. Papoulia provided supervisory guidance through overseeing formulations and editing the manuscript.

Chapter 3 has been incorporated within a paper that has been submitted for publication in *Computer Methods in Applied Mechanics and Engineering*. The paper was co-authored by myself and my supervisor, Dr. Katerina Papoulia. I developed the mathematical and computational formulation and implemented a computer program to conduct the numerical simulations. I also wrote the manuscript. Dr. Papoulia provided supervisory guidance through overseeing formulations and editing the manuscript. At the time of this writing, the paper is under revision.

Chapter 4 has been incorporated within a paper that has been submitted for publication in *Computer Methods in Applied Mechanics and Engineering*. This paper was co-authored by myself, my supervisor, Dr. Papoulia, and by our research collaborators, Dr. Nasser Khalili, Professor of Geotechnical Engineering, and Dr. Mohammad Vahab, post-doctoral fellow, in the Department of Civil and Environmental Engineering at the University of New South Wales, Australia. I designed the collaborative work, developed the computational formulation and wrote the manuscript. I also worked with the second author (Dr. Mohammad Vahab) in the computer implementation of the proposed algorithms and conducted the numerical simulations. Dr. Papoulia and Dr. Khalili were involved in overseeing the formulation and editing the manuscript. At the time of this writing, the paper is under revision.

Chapter 2

A continuation method for rigid-cohesive fracture in a discontinuous Galerkin finite element setting

This chapter is based on the following journal article:

Hirmand MR and Papoulia KD, A continuation method for rigid-cohesive fracture in a discontinuous Galerkin finite element setting. *International Journal for Numerical Methods in Engineering*, (2018) 115:627-650.

This paper was co-authored by myself and my supervisor, Dr. Katerina Papoulia. In this paper, I developed the relevant mathematical and computational techniques, implemented a computer program to perform the numerical simulations and wrote the manuscript. Dr. Papoulia provided supervisory guidance through overseeing formulations and editing the manuscript.

2.1 Introduction

An energy minimization formulation of initially rigid cohesive fracture is introduced within a discontinuous Galerkin finite element setting with Nitsche flux. The finite element discretization is directly applied to an energy functional, whose term representing the energy stored in the interfaces is nondifferentiable at the origin. Unlike finite element implementations of extrinsic cohesive models, activation of interfaces happens automatically when a certain level of stress encoded in the interface potential is reached. Thus, numerical issues associated with an external activation criterion observed in the previous literature are effectively avoided. Use of the Nitsche flux avoids the introduction of Lagrange multipliers as additional unknowns. Implicit time-stepping is performed using the Newmark scheme, for which a time-discretized "dynamic potential" is developed to properly incorporate momentum. A continuation strategy is employed for the treatment of nondifferentiability which performs faster than the one proposed in [116]. The resulting sequence of smooth nonconvex problems is solved using the trust region minimization algorithm. The method inserts cohesive interfaces at bulk element edges, which, in the absence of any information regarding crack paths, can be all element edges in the domain. The minimization algorithm then decides which interfaces activate, given the applied boundary conditions. Robustness of the proposed method and its capabilities in modelling quasistatic and dynamic problems are shown through several numerical examples.

This chapter is organized as follows. In Section 2.2, we present the formulation of the energy approach. In Section 2.3, we present the DG finite element discretization of the energy functional. The proposed optimization algorithm for the minimization of the discretized functional, which entails a continuation method for the treatment of nondifferentiability in conjunction with a trust region minimization algorithm for solving the resulting smooth problem, is presented in Section 2.4. Section 2.5 contains the temporal discretization scheme and a proposed functional that properly incorporates inertia into the formulation. Section 2.6 presents several numerical simulations of quasistatic and dynamic crack propagation problems. Finally, Section 2.7 offers some concluding remarks.

2.2 Formulation of the energy approach

We consider a body $\Omega \subset \mathbb{R}^{n_{\text{dim}}}$ ($n_{\text{dim}} = 2, 3$) bounded externally by $\partial\Omega$ and containing an evolving $(n_{\text{dim}} - 1)$-dimensional surface $\mathcal{S}$ in the interior of its domain representing cracks, as shown in Figure 2.1. The external boundary $\partial\Omega$, whose unit outward normal is denoted

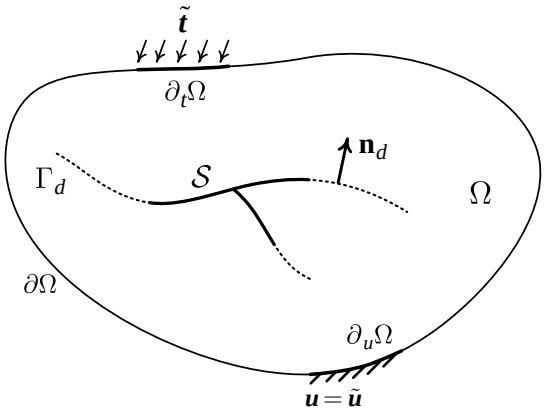

Figure 2.1: Schematic of a solid body Ω containing evolving crack surfaces $\mathcal{S}$. The discontinuity boundary Γ_d represents potential crack paths

$\mathbf{n}$, consists of disjoint parts $\partial_{u_\alpha}\Omega$ and $\partial_{t_\alpha}\Omega$, on which displacement and traction boundary conditions are prescribed, respectively, for each coordinate direction $\alpha = 1 : n_{\text{dim}}$, $\partial_{u_\alpha}\Omega \cup \partial_{t_\alpha}\Omega = \partial\Omega$ and $\partial_{u_\alpha}\Omega \cap \partial_{t_\alpha}\Omega = \emptyset \ \forall\alpha$. Let $\mathbf{u}(\mathbf{x},t) : \Omega \to \mathbb{R}^{n_{\text{dim}}} \times [0,T]$ be the displacement of the fractured body, which is continuous and differentiable everywhere in $\Omega\backslash\mathcal{S}$ except for nonzero jumps across crack surfaces $\mathcal{S}$. To overcome the complexities associated with treating crack surfaces $\mathcal{S}$ as an unknown of the energy minimization formulation, we restrict evolution of $\mathcal{S}$ to a set of *a priori* known discontinuity boundaries $\Gamma_d \subset \Omega$. These represent potential crack paths so that $\mathcal{S} \subseteq \Gamma_d$ throughout the course of crack propagation. Consistent with this assumption, the displacement is allowed to admit a jump $[\![\mathbf{u}(\mathbf{x},t)]\!]$ everywhere on Γ_d. An auxiliary discontinuity opening displacement field $\boldsymbol{\delta}(\mathbf{x},t) : \Gamma_d \to \mathbb{R}^{n_{\text{dim}}} \times [0,T]$ is then defined that tracks the evolution of $\mathcal{S}$ in Γ_d by requiring that

$$\boldsymbol{g}(\mathbf{u},\boldsymbol{\delta}) \equiv [\![\mathbf{u}(\mathbf{x},t)]\!] - \boldsymbol{\delta}(\mathbf{x},t) = \mathbf{0} \quad \text{on } \Gamma_d. \tag{2.1}$$

It follows from the above formulation that $\mathcal{S}(t) = \{\mathbf{x} \in \Gamma_d \,|\, \boldsymbol{\delta}(\mathbf{x},t) \neq \mathbf{0}\}$. The complete state of deformation and fracture of the body is thus described by two independent unknowns, namely $\mathbf{u}$ and $\boldsymbol{\delta}$.

Let $\mathbf{n}_d$ denote the unit normal to the discontinuity. For simplicity, we assume that the deformation is small, so we do not differentiate between the normals to the deformed and undeformed configurations. This assumption does not compromise the main aspects of the method, although it does undermine its ability to quantify the crack opening, which, in the scale of some problems, may indeed be large; see [116] for a fully nonlinear formulation. Accordingly, the normal and sliding components of the jump are defined as $[\![u_n]\!] = [\![\mathbf{u}]\!] \cdot \mathbf{n}_d$

and $[\![\mathbf{u}_s]\!] = [\![\mathbf{u}]\!] - [\![u_n]\!]\mathbf{n}_d$, respectively. Similar definitions can also be made for the discontinuity opening $\boldsymbol{\delta}$, that is, $\delta_n = \boldsymbol{\delta}\cdot\mathbf{n}_d$ and $\boldsymbol{\delta}_s = \boldsymbol{\delta} - \delta_n\mathbf{n}_d$. Defining the opening $\boldsymbol{\delta}$ and deformation $\mathbf{u}$ as independent variables enables the energy formulation to model the bulk and the cracks as independent entities which are, however, related through constraint (2.1) for compatibility of the unknowns fields.

The potential energy of an elastic body is expressed as the sum of the elastic strain energy stored in the bulk, the work of external and body forces, the energy stored in the interfaces and the energy due to momentum:

$$\begin{aligned}\pi(\mathbf{u},\boldsymbol{\delta}) = \int_{\Omega\setminus\Gamma_d} \psi\left(\boldsymbol{\varepsilon}(\mathbf{u})\right)\, dV - \int_{\Omega\setminus\Gamma_d} \mathbf{u}\cdot\mathbf{b}\, dV - \\ \int_{\partial_t\Omega} \mathbf{u}\cdot\widetilde{\mathbf{t}}\, dS + \int_{\Gamma_d} \left(\psi_{\text{cohs}}(\boldsymbol{\delta}) + I_{\mathbb{R}^+}(\delta_n)\right)\, dS + \pi_{\text{dyn}}(\mathbf{u}).\end{aligned} \tag{2.2}$$

The strain energy density function in the first integral is

$$\psi\left(\boldsymbol{\varepsilon}(\mathbf{u})\right) = \frac{1}{2}\boldsymbol{\varepsilon}(\mathbf{u}) : \mathbf{D} : \boldsymbol{\varepsilon}(\mathbf{u}), \tag{2.3}$$

in which $\mathbf{D}$ is the elasticity constitutive tensor and $\boldsymbol{\varepsilon}(\mathbf{u}) = \nabla^s\mathbf{u} \in \mathbb{R}^{n_{\text{dim}}} \times \mathbb{R}^{n_{\text{dim}}}$ is the symmetric part of the displacement gradient. In the second and third integrals, $\mathbf{b}$ is the body force per unit volume and $\widetilde{\mathbf{t}}$ is a prescribed traction vector on $\partial_t\Omega$ (for simplicity of notation, it is assumed that $\partial_{t_\alpha}\Omega = \partial_t\Omega, \alpha = 1 : n_{\text{dim}}$).

The fourth integral in (2.2) contains two terms, the first of which is the cohesive energy corresponding to an initially rigid model and the second an interpenetration penalty that precludes overlap of the discontinuity faces. The two potential functions ψ_{cohs} and $I_{\mathbb{R}^+}$ are functions of $\boldsymbol{\delta}$ and of $\delta_n = \boldsymbol{\delta}\cdot\mathbf{n}_d$, respectively. The precise form of these functions will be discussed in Section 2.4. Both potentials are nondifferentiable at their origins ($\boldsymbol{\delta} = \mathbf{0}$ and $\delta_n = 0$, respectively). This is the crucial mathematical property that keeps the interfaces closed until a certain level of stress/elastic energy is reached in the body (i.e., initially rigid behavior), see the discussion in 1.6.2. In addition, the cohesive potential ψ_{cohs} is nonconvex in $\boldsymbol{\delta}$ so as to capture the expected softening behavior when an interface point opens. The last term in the potential (2.2) stores the "dynamic energy" due to inertia. Because a time dependent potential is difficult to achieve, we obtain a proper "time-discretized" form of this potential using finite difference approximations to the displacement unknowns after time discretization in Section 2.5.

We characterize the equilibrium of the body by the solution of the following constrained minimization problem that must be solved at each time step:

$$\text{find } (\mathbf{u}^\star, \boldsymbol{\delta}^\star) \in \mathcal{U}\times\mathcal{D} \text{ minimizing } \pi(\mathbf{u},\boldsymbol{\delta}) \text{ subject to } \boldsymbol{g}(\mathbf{u},\boldsymbol{\delta}) = \mathbf{0}, \tag{2.4}$$

where $\mathcal{U}$ and $\mathcal{D}$ are spaces of admissible solutions to be approximated by a particular finite element discretization and $\boldsymbol{g}(\mathbf{u}, \boldsymbol{\delta})$ is a linear constraint function as defined in (2.1).

The Lagrangian for the constrained optimization problem (2.4) is

$$\mathcal{L}(\mathbf{u}, \boldsymbol{\delta}, \boldsymbol{\lambda}) = \pi(\mathbf{u}, \boldsymbol{\delta}) + \int_{\Gamma_d} \boldsymbol{\lambda} \cdot \boldsymbol{g} \, dS \tag{2.5}$$

where $\boldsymbol{\lambda}$ is the Lagrange multiplier field. A saddle point of the above Lagrangian corresponds to a solution $(\mathbf{u}^\star, \boldsymbol{\delta}^\star)$ of (2.4).

In a usual variational approach, one would now pass to the derivative of the energy functional to arrive at a weak form through a variational formulation. In our setting, this is not a valid approach because the energy functional in (2.5) is not globally differentiable. We therefore directly apply finite element discretization to the energy functional and solve the resulting finite-dimensional, nondifferentiable energy minimization problem. We note that variational formulations introducing a traction-opening relationship and relying on an extrinsic failure criterion for activation are not mathematically equivalent to the present energy minimization formulation.

In the work of Lorentz [91] a formulation is obtained from the nondifferentiable energy functional by exploiting the concept of a sub-gradient. The method leads to a set of nonlinearly constrained equations to be solved and a constitutive update relation for the opening of the interfaces. A DG implementation of Lorentzs method was presented in [161]. Our method differs from that of Lorentz [91] in that it makes use of a nondifferentiable, nonconvex optimization algorithm to directly tackle the finite-dimensional energy minimization problem arising from a finite element discretization of the energy potential.

2.3 The finite-dimensional problem

The proposed finite element discretization is based on the DG method [89]. The body Ω is approximated by a mesh Ω_h, bounded by $\partial\Omega_h$, $\Omega_h = \cup_e \omega_h^e$, $\overline{\omega}_h^e \cap \overline{\omega}_h^{e'} = \emptyset \, \forall e \neq e'$, where $\overline{\omega}_h^e$ represents the interior of element ω_h^e (Figure 2.2). The deformation field $\mathbf{u}(\mathbf{x}, t)$ is approximated by a piecewise polynomial approximation $\mathbf{u}_h(\mathbf{x}, t)$ in the finite-dimensional space of kinematically admissible solutions

$$\mathcal{U}_h = \left\{ \mathbf{u}_h|_{\omega_h^e} \in \mathcal{P}^p(\omega_h^e) \; \forall \omega_h^e \in \Omega_h; \mathbf{u}_{h_\alpha} = \widetilde{\mathbf{u}}_{h_\alpha} \text{ on } \partial_{u_\alpha}\Omega_h \right\}, \tag{2.6}$$

where $\mathcal{P}^p(\omega_h^e)$ is the space of polynomials of order up to p with support in ω_h^e and $\widetilde{\mathbf{u}}_{h_\alpha}$ is a prescribed displacement on the Dirichlet boundary in the direction α. For the quadratic

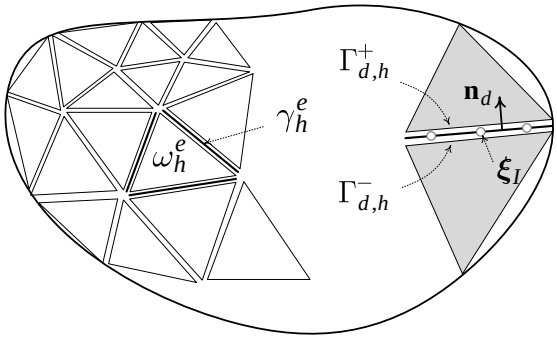

Figure 2.2: Schematic of the discontinuous Galerkin discretization, Ω_h, of the domain and related definitions

triangles used in Section 2.6, $p = 2$. Neighbouring elements do not share nodal points and edges, which allows for jump discontinuities $[\![\mathbf{u}_h(\mathbf{x}, t)]\!]$ of polynomial order p at inter-element boundaries.

The union of element boundaries excluding $\partial\Omega_h$ constitutes the discretized discontinuity boundary $\Gamma_{d,h} = \cup_e \partial\omega^e_h \backslash \partial\Omega_h$. The two faces of the discontinuity are denoted by positive and negative signs as $\Gamma^+_{d,h}$ and $\Gamma^-_{d,h}$ with the unit normal pointing toward $\Gamma^+_{d,h}$. Although the DG discretization does not require the FE mesh to be conforming on $\Gamma_{d,h}$, we use, for simplicity, only conforming meshes. Conventional interface elements [113] of dimension $n_{\text{dim}} - 1$, denoted by γ^e_h in Figure 2.2, are placed at inter-element boundaries to provide a means for numerical integration on $\Gamma_{d,h}$. It follows that $\cup_e \gamma^e_h = \Gamma_{d,h}$.

The finite element approximation of $\boldsymbol{\delta}$, $\boldsymbol{\delta}_h$, is independent of $\mathbf{u}_h$ and thus, of $[\![\mathbf{u}(\mathbf{x}, t)]\!]$. As the potential (2.5) does not involve spatial derivatives of $\boldsymbol{\delta}$, the regularity requirement for $\boldsymbol{\delta}_h$ is weaker than that for $\mathbf{u}_h$ and admits discontinuous approximations along an interface element. For simplicity, we follow the discretization used in [91], whereby a piecewise-constant approximation is employed. Such approximation can be constructed by introducing M nodal points with coordinates $\boldsymbol{\xi}_I \in \Gamma_{d,h}$, $I = 1, 2, , M$ on the interface. The location of the nodal points is chosen to be the Gauss quadrature points of the interface elements. As such, each Gauss point on the interface holds an interface opening degree of freedom representing the constant value of the approximation in some vicinity of the Gauss point. The size of this vicinity does not affect the numerical integration on γ^e_h as values of the integrands are only needed at the Gauss points.

The Lagrange multiplier $\boldsymbol{\lambda}$ is replaced by a numerical flux $\boldsymbol{\lambda}^{\text{DG}}_h$ expressed as a function of primal variables $(\mathbf{u}_h, \boldsymbol{\delta}_h)$ due to Nitsche [107]. This circumvents the need for the fulfillment of the Ladyzhenskaya-Babuska-Brezzi (LBB) condition [23], which restricts the types of

numerically stable displacement-multiplier interpolation combinations, and reduces the number of unknowns compared to a Lagrange multiplier method. Additionally, the method is computationally more cost effective compared to an augmented Lagrange method as computation of the multiplier field does not require an outer augmentation loop as in [116]. The DG flux $\boldsymbol{\lambda}_h^{\mathrm{DG}}$ is [89]

$$\boldsymbol{\lambda}_h^{\mathrm{DG}} = \langle \boldsymbol{\sigma}_h \rangle \, \mathbf{n}_d + \frac{1}{2} \eta \boldsymbol{g}_h, \tag{2.7}$$

in which $\boldsymbol{\sigma}_h = \boldsymbol{\sigma}(\mathbf{u}_h)$ is the Cauchy stress tensor, obtained strongly from $\mathbf{u}_h$, $\langle * \rangle = \frac{1}{2}(*^+ + *^-)$, and η is a sufficiently large penalty number. The first term in (2.7) ensures consistency of the numerical scheme, whereas the second term ensures stability. The penalty number on each interface element γ_h^e is taken as

$$\eta = \frac{\chi \mu}{h_s|_{\gamma_h^e}}, \tag{2.8}$$

in which $h_s|_{\gamma_h^e} = 2 \left(\frac{\mathrm{meas}(\gamma_h^e)}{\mathrm{meas}(\omega_h^{e+})} + \frac{\mathrm{meas}(\gamma_h^e)}{\mathrm{meas}(\omega_h^{e-})} \right)^{-1}$ is the characteristic element size, μ is the shear modulus and χ is a number that must be taken larger than a certain threshold to ensure stability of the method and insensitivity to the magnitude of the penalty number. The range $2 \leq \chi \leq 10$ is suggested in [109]. Note that, as suggested by Equation (2.7), in the limit as $\boldsymbol{g}_h \to \mathbf{0}$, $\boldsymbol{\lambda}_h^{\mathrm{DG}}$ takes the value of $\langle \boldsymbol{\sigma}_h \rangle \, \mathbf{n}_d$ irrespective of the magnitude of η.

With finite element approximations $\mathbf{u}_h$, $\boldsymbol{\delta}_h$ and $\boldsymbol{\lambda}_h^{\mathrm{DG}}$, the minimization problem (2.5) results into the following finite-dimensional problem:

$$\min_{(\mathbf{U},\mathbf{d})} \left\{ \mathcal{L}^{\mathrm{DG}}(\mathbf{u}_h, \boldsymbol{\delta}_h) = \pi(\mathbf{u}_h, \boldsymbol{\delta}_h) + \int_{\Gamma_{d,h}} \langle \boldsymbol{\sigma}_h \rangle \, \mathbf{n}_d \cdot \boldsymbol{g}_h \, dS + \frac{1}{2} \int_{\Gamma_{d,h}} \eta \boldsymbol{g}_h \cdot \boldsymbol{g}_h \, dS \right\}, \tag{2.9}$$

where $\mathbf{U}$ and $\mathbf{d}$ denote the global vector of nodal unknowns corresponding to $\mathbf{u}_h$ and $\boldsymbol{\delta}_h$, respectively. A straightforward minimization of the above potential is out of reach due to nondifferentiability and nonconvexity of the potential function. In what follows, we will describe a minimization algorithm that is capable of handling the nondifferentiable, nonconvex problem.

2.4 Nondifferentiable energy minimization

2.4.1 The cohesive potential

We consider a general class of cohesive models proposed by Ortiz and Pandolfi [113], in which the cohesive potential is expressed as a function of a scalar effective opening displacement δ defined by

$$\delta(\delta_n, \boldsymbol{\delta}_s) = \sqrt{(\delta_n^+)^2 + \|\beta \boldsymbol{\delta}_s\|^2}, \tag{2.10}$$

in which $\delta_n^+ = \max(0, \delta_n)$ and the material constant β weights the normal and tangential components of the displacement vector. The particular form of potential function considered in this chapter is

$$\psi_{\text{cohs}}(\boldsymbol{\delta}) = \begin{cases} \sigma_c \delta - \frac{\sigma_c \delta^2}{2\delta_c} & \delta \in [0, \delta_c) \\ \frac{\sigma_c \delta_c}{2} & \delta \in [\delta_c, \infty), \end{cases} \tag{2.11}$$

in which σ_c and δ_c are the cohesive model parameters representing material strength and critical opening displacement, i.e., opening displacement at loss of cohesion, respectively, see Figure 2.3a. The above, nonconvex in δ, potential corresponds to linear softening behavior in the cohesive process zone:

$$\mathbf{t}_{\text{cohs}} \equiv \nabla_{\boldsymbol{\delta}} \phi = \frac{t_{\text{cohs}}(\delta)}{\delta} (\delta_n^+ \mathbf{n}_d + \beta^2 \boldsymbol{\delta}_s), \quad \boldsymbol{\delta} \neq \mathbf{0}, \tag{2.12}$$

where $\mathbf{t}_{\text{cohs}}$ is the cohesive traction vector and

$$t_{\text{cohs}}(\delta) = \begin{cases} \sigma_c \left(1 - \frac{\delta}{\delta_c}\right) & \delta \in [0, \delta_c) \\ 0 & \delta \in [\delta_c, \infty), \end{cases} \tag{2.13}$$

is a scalar effective traction (Figure 2.3b). The value $\psi_{\text{cohs}}(0) - \psi_{\text{cohs}}(\infty)$ represents the critical fracture energy, which for the present model is $G_c = \sigma_c \delta_c / 2$. We note that the gradient (2.12) is not defined at zero interface opening $\delta_n = \|\boldsymbol{\delta}_s\| = 0$, i.e., the potential (2.11) regarded as a function of $(\delta_n, \boldsymbol{\delta}_s)$ is not differentiable at the origin. The nondifferentiability is due to the presence of the ratios δ_n/δ and $\boldsymbol{\delta}_s/\delta$, which follows from the definition of the norm (2.10). These are both $0/0$ at $\boldsymbol{\delta} = \mathbf{0}$, which, in contrast to the nonsingular, smoothed by continuation case described in Section 2.4.2, cannot be resolved with use of L'Hôpital's rule. This nondifferentiability is fundamental to the model; it is precisely the reason that

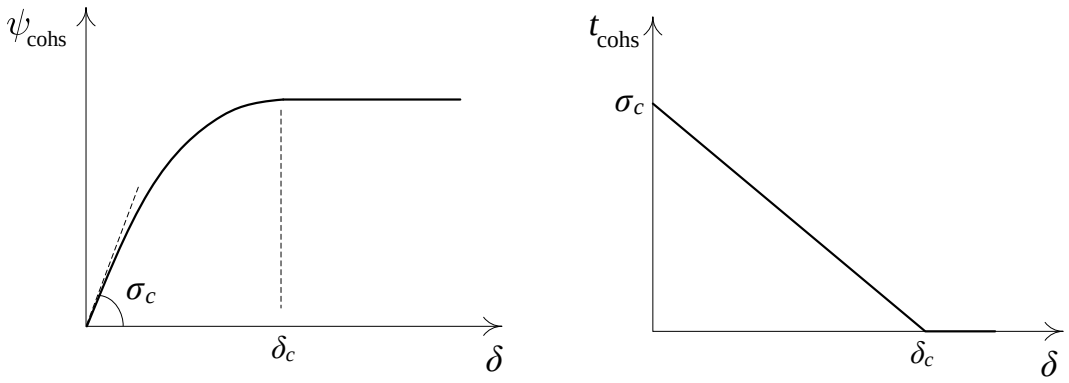

Figure 2.3: a) Cohesive potential ψ_{cohs} and b) effective cohesive traction $t_{\text{cohs}} = \frac{d\psi_{\text{cohs}}}{d\delta}$ as functions of the scalar effective opening δ

the interfaces exhibit initially rigid behavior, that is, the minimizer of the potential occurs at $\boldsymbol{\delta} = \mathbf{0}$ until a positive critical value of the load is attained.

The interpenetration penalty is the indicator function $I_{\mathbb{R}^+}(\delta_n)$ defined as:

$$I_{\mathbb{R}^+}(\delta_n) = \begin{cases} \infty & \delta_n \in (-\infty, 0) \\ 0 & \delta_n \in [0, \infty). \end{cases} \tag{2.14}$$

The indicator function precludes interpenetration since negative displacement jumps would result in infinite energy (hence not a minimum). The interpenetration potential is also nondifferentiable at the origin. The contact traction $t_{\text{cont}}(\boldsymbol{\delta}) = \frac{\partial I_{\mathbb{R}^+}(\delta_n)}{\partial \delta_n} \mathbf{n}_d$ is zero for $\delta_n \to 0^+$, whereas for $\delta_n \to 0^-$ it is undefined. Different definitions of the interpenetration potential are possible, e.g., [116]. Figure 2.4 shows variation of the total interface potential $\phi = \psi_{\text{cohs}} + I_{\mathbb{R}^+}$ as a function of the normal and tangential components of the opening field.

2.4.2 Treatment of nondifferentiability: continuation algorithm

Nondifferentiable objective minimization algorithms usually include solution of a sequence of differentiable problems to achieve the solution of the nondifferentiable problem within desired accuracy [14, 174]. The methodology presented in this chapter follows that proposed in [116]. It entails construction of an outer solution loop, referred to as the continuation loop, in which the interface potentials are approximated by a differentiable, smooth

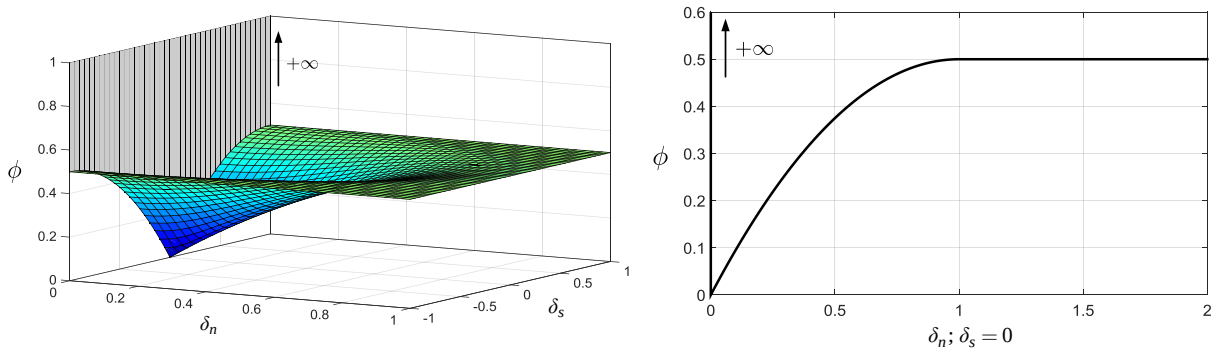

(a) (b)

Figure 2.4: Variation of the total interface potential $\phi = \psi_{\text{cohs}} + I_{\mathbb{R}^+}$ or $\sigma_c = 1.0$ and $\delta_c = 1.0$ a) as a function of δ_n and δ_s and b) as a function of δ_n in the plane $\delta_s = 0$. The potential exhibits a sudden jump to infinity when δ_n becomes negative

function. Smoothness is successively decreased within the continuation iterations, and the previously converged smooth solution is used to form a suitable starting point for the next run of the minimization algorithm with the new, less smooth model. The process is continued until a desired level of accuracy is achieved for the approximation of the nonsmooth potential. In this manner, the problem to be solved in each continuation iteration is minimization of a smooth, nonconvex potential that can be solved using an appropriate smooth minimization algorithm such as the *trust region* method (see Section 2.4.3).

Several continuation strategies can be introduced. The one proposed here is outlined in Algorithm 2.1. Two smoothing parameters are introduced. The first, δ_e, represents the radius of a vicinity of the origin in which the interface potential is approximated by a differentiable expression. The second, $\widehat{\delta}_c$, is a fictitious critical opening displacement that replaces the true critical opening of the cohesive model at intermediate steps of continuation.

The approximate, smooth cohesive potential $\widehat{\psi}_{\text{cohs}}$ used within the continuation iterations is expressed as

$$\widehat{\psi}_{\text{cohs}}(\delta; \delta_e, \widehat{\delta}_c) = \begin{cases} \frac{\sigma_c \delta^2}{2\delta_e} & \delta \in [0, \delta_e) \\ \frac{\sigma_c \widehat{\delta}_c}{\widehat{\delta}_c - \delta_e} \left(\delta - \frac{\delta^2}{2\widehat{\delta}_c} - \frac{\delta_e}{2} \right) & \delta \in [\delta_e, \widehat{\delta}_c) \\ \frac{\sigma_c \widehat{\delta}_c}{2} & \delta \in [\widehat{\delta}_c, \infty). \end{cases} \tag{2.15}$$

This potential corresponds to an initially elastic model, with δ_e the interface opening corresponding to σ_c, which has a well-defined gradient everywhere including at $\delta = 0$.

Algorithm 2.1 The continuation algorithm

Initiate the solution $\mathbf{U} = \mathbf{0}$ and $\mathbf{d} = \mathbf{0}$.
Loop on time steps $i = 0, 1, ..., N$
  Initiate smoothing parameters: δ_e^0 and $\widehat{\delta}_c^0$
  Loop on continuation $j = 1, 2, ..., J$
    (i) Solve the smooth problem (Algorithm 2.2) with approximate potentials $\widehat{\psi}_{\text{cohs}}$ and $\widehat{I}_{\mathbb{R}^+}$ (eqns. (2.15) and (2.16))
    (ii) Initiate the starting point for the next round of smooth minimization problem: for each interface point I, set $\mathbf{d}_I = \mathbf{0}$ if $\delta_I \leq \delta_e$
    (iii) $j \to j + 1$; decrease δ_e and $\widehat{\delta}_c$ using eq. (2.17) to form the new, less smooth model
  End loop on continuation
  $i \to i + 1$; update unknowns
End loop on time steps

Notice that for the smooth potential (2.15), $t_{\text{cohs}}(\delta) = \sigma_c \delta / \delta_e$ for $\delta \in [0, \delta_e)$, and the δ in the denominator of (2.12) cancels out with the δ now appearing in the numerator of $t_{\text{cohs}}(\delta)$. In a similar manner, the smooth interpenetration penalty potential $\widehat{I}_{\mathbb{R}^+}$ is expressed as

$$\widehat{I}_{\mathbb{R}^+}(\delta_n; \delta_e) = \begin{cases} \frac{c\sigma_c \delta_n^2}{2\delta_e} & \delta_n \in (-\infty, 0) \\ 0 & \delta_n \in [0, \infty). \end{cases} \tag{2.16}$$

The parameter c is a constant that determines the maximum effective penalty traction that resists interpenetration, which, in subsequent calculations, is fixed at $c = 5$. In the limit $\delta_e \to 0$, the smoothed potentials (2.15) and (2.16) approach the original nonsmooth potentials (2.11) and (2.14). Thus, we initiate the continuation loop with a relatively large δ_e and successively decrease it within the continuation iterations until a sufficiently small tolerance is achieved for the approximation. Figure 2.5 shows variations of the smoothed interface potential $\widehat{\phi} = \widehat{\psi}_{\text{cohs}} + \widehat{I}_{\mathbb{R}^+}$ for two levels of smoothness.

The reason for the replacement of the critical opening δ_c by the fictitious value $\widehat{\delta}_c$ in (2.15) is as follows. In our experience, starting from a solution, in which all interfaces under tension are slightly open, it is easily possible that δ on one or more interfaces exceeds its critical value. At this point these interfaces lose cohesion and will not recover on subsequent iterations. This behavior is certainly enhanced by nonconvexity of the potential for $\delta \in [\delta_e, \widehat{\delta}_c)$. The sudden change of curvature from $\sigma_c/\delta_e \gg 1$ to $-\sigma_c/\delta_c \ll 1$ at $\delta = \delta_e$ can also cause rapid changes in the search direction of the trust region optimization

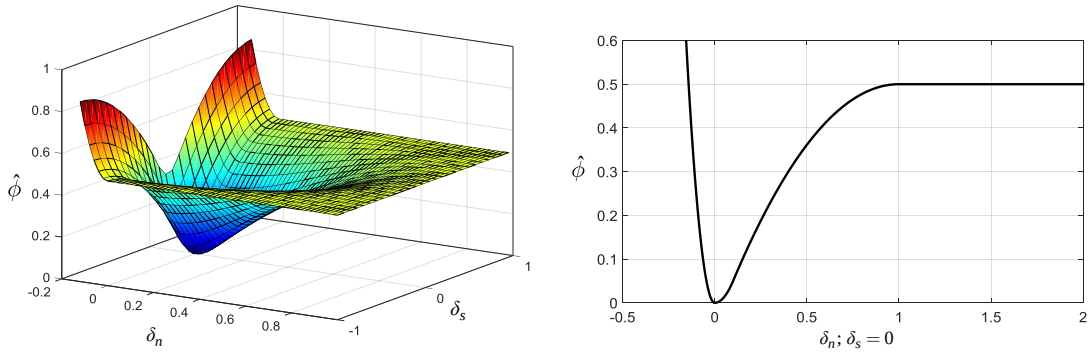

(a)

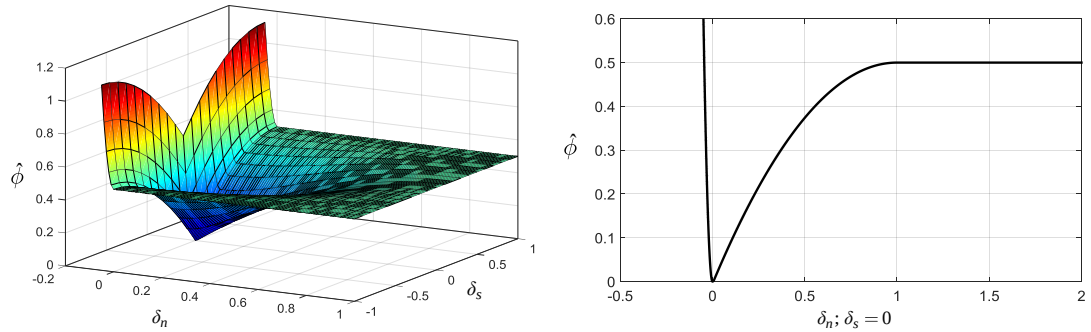

(b)

Figure 2.5: Variation of the smoothed interface potential $\widehat{\phi} = \widehat{\psi}_{\text{cohs}} + \widehat{I}_{\mathbb{R}^+}$ as a function of the normal and tangential components of the opening field with $\sigma_c = 1.0$ and $\widehat{\delta}_c = 1.0$ for a) $\delta_e = 0.1$ and b) $\delta_e = 0.01$. The graphs on the right show the variation of the potential with δ_n in the plane $\delta_s = 0$

algorithm and create convergence difficulties, especially when δ_c is small. This behavior can be prevented by limiting the step-size of the optimization method. In our case, however, this is better achieved by replacing δ_c by a larger fictitious value $\widehat{\delta}_c$ during intermediate steps of continuation. The fictitious value is chosen to be fairly large on the first iteration of continuation and is decreased to the true value on the final iteration.

We reduce the smoothing parameters in an exponential fashion using the relations

$$\delta_e^j = \delta_e^{\text{tol}} \left(\frac{\delta_e^0}{\delta_e^{\text{tol}}} \right)^{1-\frac{j}{J}}, \qquad \widehat{\delta}_c^j = \delta_c \left(\frac{\widehat{\delta}_c^0}{\delta_c} \right)^{1-\frac{j}{J}}, \tag{2.17}$$

where δ_e^0 and $\widehat{\delta}_c^0$ are initial values on the first continuation step, J is the number of contin-

uation steps, and $j \in \{0, 1, 2, ..., J\}$ is the continuation iteration index. Other choices of reduction are also possible. The continuation is performed globally, i.e., there is a single value of δ_e and $\widehat{\delta}_c$ for all domain interfaces in each continuation step.

The solution obtained in a continuation step is used to form a starting point for the optimization algorithm in the next continuation step. To do so, the effective opening of all interface points is checked against the smoothing parameter δ_e at the end of each continuation step. An interface Gauss point I whose effective opening has remained smaller than δ_e is deemed to be at zero-opening and its nodal opening, $\mathbf{d}_I$, is set to zero in the long vector of nodal unknowns $\mathbf{d}$. The optimization algorithm is initiated in the next continuation step using this modified vector of unknowns.

Irreversibility. Following Ortiz and Pandolfi [113], the physical requirement of an irreversible fracturing process can be modeled through incorporating a history variable in the cohesive potential, which, at time t_i, is defined as the maximum opening attained up until time t_i, i.e., the evolution of which is $\delta_{\max,i} = \max_{t' \in \{t_0,...,t_{i-1}\}} \delta(t')$ in a time discrete setting. Note that $\delta_{\max,i}$ is fixed at the beginning of time-step i and, as such, is not an additional variable but a parameter in the context of optimization. Let $\sigma_{\max,i}$ denote the effective traction corresponding to $\delta_{\max,i}$. We assume unloading to the origin, for which the cohesive potential at time step i is given by

$$\psi_{\text{cohs}}(\delta; \delta_{\max,i}, \widehat{\delta}_c) = \begin{cases} \frac{\sigma_c \delta^2}{2\delta_{\max,i}} & \delta \in [0, \delta_{\max,i}) \\ \frac{\sigma_c \widehat{\delta}_c}{\widehat{\delta}_c - \delta_{\max,i}} \left(\delta - \frac{\delta^2}{2\widehat{\delta}_c} - \frac{\delta_{\max,i}}{2} \right) & \delta \in [\delta_{\max,i}, \hat{\delta}_c) \\ \frac{\sigma_c \widehat{\delta}_c}{2} & \delta \in [\widehat{\delta}_c, \infty). \end{cases} \tag{2.18}$$

The above potential, which is differentiable everywhere, becomes operative only after an interface point activates, therefore $\delta_{\max,i} > 0$. An interface point is said to be activated when its effective opening, obtained at the end of a solution step, exceeds δ_e^{tol}. For the interface points that are identified as activated, potential (2.18) replaces (2.15) in the computations of subsequent time steps. The maximum opening of interface points is then updated to $\delta_{\max,i+1} = \max\{\delta_{\max,i}, \delta(t_i)\}$.

2.4.3 Solving the smooth problem: trust region algorithm

A trust-region algorithm, see e.g., [174], is used for the solution of the smooth problem in each step of the continuation iteration, i.e., in step (i) of the inner continuation loop in Algorithm 2.1. The method is particularly capable of handling nonconvex objectives as

the one in (2.15) or (2.18). It bears emphasis that the standard Newton's method cannot be used here due to nonconvexity of the potential.

Algorithm 2.2 The trust region minimization algorithm

Given $\mathbf{y}_0$, $\Delta_0 > 0$ and $r \in [0, \frac{1}{4})$
Loop on trust region iterations $k = 0, 1, ...$ until convergence

(i) Check for convergence
if $\frac{\mathbf{g}(\mathbf{y}_k)}{\mathbf{g}(\mathbf{y}_0)} \leq \text{tol}_{\mathbf{g}}$ and $\frac{\mathcal{L}^{\text{DG}}(\mathbf{y}_k) - \mathcal{L}^{\text{DG}}(\mathbf{y}_{k-1})}{\mathcal{L}^{\text{DG}}(\mathbf{y}_0)} \leq \text{tol}_{\pi}$, declare convergence and **exit**

(ii) Obtain the solution of the minimization problem (2.19), $d\mathbf{y}^\star$

(iii) Evaluate the ratio $r = \frac{\mathcal{L}^{\text{DG}}(\mathbf{y}_k) - \mathcal{L}^{\text{DG}}(\mathbf{y}_k + d\mathbf{y}^\star)}{m_k(\mathbf{0}) - m_k(d\mathbf{y}^\star)}$

(iv) Update trust region radius
if $r < \frac{1}{4}$, **then**
$\Delta_{k+1} = 0.5\Delta_k$
elseif $r \geq \frac{3}{4}$ and $\|d\mathbf{y}^\star\| = \Delta_k$, **then**
$\Delta_{k+1} = 2\Delta_k$
end

(v) Update solution estimate
if $r > r_0$, **then**
$\mathbf{y}_{k+1} = \mathbf{y}_k + d\mathbf{y}^\star$
else
$\mathbf{y}_{k+1} = \mathbf{y}_k$
end

End loop on trust region iterations

Let $\mathbf{y} = \{\mathbf{U}, \mathbf{d}\}$ denote the vector of all unknowns. The trust region iteration is initialized with $\mathbf{y}_0$, obtained from the converged solution of the previous continuation step, as explained in the previous subsection, and with a trust region radius Δ_0 taken to be the real-space diameter of a typical mesh element. This value is reset at the beginning of each continuation step. Algorithm 2.2 outlines the steps involved in the trust region algorithm. The k^{th} iteration of the trust region algorithm seeks the solution of the following quadratic sub-problem

$$\min_{d\mathbf{y}} m_k(d\mathbf{y}) \quad \text{s.t.} \quad \|d\mathbf{y}\| \leq \Delta_k, \tag{2.19}$$

where $m_k(d\mathbf{y}) = \mathcal{L}^{\text{DG}}(\mathbf{y}_k) + \mathbf{g}(\mathbf{y}_k) \cdot d\mathbf{y} + \frac{1}{2} d\mathbf{y} \cdot \mathbf{H}(\mathbf{y}_k) \cdot d\mathbf{y}$ obtained from the first three terms of the Taylor series expansion of $\mathcal{L}^{\text{DG}}$ around the current solution estimate $\mathbf{y}_k$ with

$\mathbf{g}(\mathbf{y}_k) = \nabla\mathcal{L}^{\mathrm{DG}}(\mathbf{y}_k)$ and $\mathbf{H}(\mathbf{y}_k) = \nabla^2\mathcal{L}^{\mathrm{DG}}(\mathbf{y}_k)$, the gradient and Hessian of the potential $\mathcal{L}^{\mathrm{DG}}$ evaluated at $\mathbf{y}_k$, respectively. Since the model is more accurate near $\mathbf{y}_k$, the method tries to find a minimum within a ball of radius Δ_k in which the model can be "trusted". Details of the finite element formulation for the gradient and Hessian of the potential may be found in Appendix A.

Within the trust region iterations, variation of the trust region size and the decision on whether or not to accept a solution increment are made based on the agreement between the improvement (increment) in the true objective, $\mathcal{L}^{\mathrm{DG}}(\mathbf{y}_k) - \mathcal{L}^{\mathrm{DG}}(\mathbf{y}_k + d\mathbf{y}^\star)$, and the increment of the model function, $m_k(\mathbf{0}) - m_k(d\mathbf{y}^\star)$ (see the parameter r in Algorithm 2.2), where $d\mathbf{y}^\star$ is the solution of subproblem (2.19). The solution $d\mathbf{y}^\star$ is accepted as a valid increment only if the actual reduction in the potential is "big" enough ($r > r_0$ in Algorithm 2.2). The iterations may be terminated when the desired tolerances for the gradient and the relative variation of the potential ($\mathrm{tol}_{\mathbf{g}}$ and tol_π, respectively) are achieved. In order to solve the trust region subproblem (2.19), the "nearly exact" method of More and Sorensen [102, 174] has been employed which is particularly capable of handling indefinite Hessians. The method reduces (2.19) to a one-dimensional root finding problem expressed as $\|p(\xi)\| = \Delta_k$, $p(\xi) = -(\mathbf{H}(\mathbf{y}_k) + \xi\mathbf{I})^{-1}\mathbf{g}(\mathbf{y}_k)$, that must be solved for ξ. For details on the trust region subproblem algorithm, the reader is referred to [102, 174].

Remark 1. *Continuation vs. regularization.* The continuation approach proposed in this chapter is not equivalent to simple regularization of the cohesive traction-separation relationship. Continuation entails a series of regularizations until δ_e is driven arbitrarily close to the rigid-cohesive model within desired tolerance. Prior to activation, zero interface opening is found to be the minimizer of the potential, rather than appearing as a result of penalization and is enforced consistently as a constraint on the deformation of the body. Such approach sidesteps the numerical issues related to the artificial compliance of initially elastic models [84]. Furthermore, the smoothing parameter δ_e does not contribute to the $u-u$ block of the Hessian matrix (see Appendix A), which facilitates convergence for small values of δ_e.

Remark 2. *Effect of the penalty on definiteness of the Hessian.* As the term $\frac{1}{2}\int_{\Gamma_{d,h}} \eta\boldsymbol{g}_h\cdot\boldsymbol{g}_h\,dS$ in the finite-dimensional potential (2.9) is quadratic in $\mathbf{d}$, the magnitude of the penalty η affects convexity of (2.9) thus definiteness of the Hessian matrix. One can show that the potential in (2.9) is convex in $\mathbf{d}$ provided that $\eta > \max\{\sigma_c/\delta_c, \beta^2\sigma_c/\delta_c\}$. The latter is not a necessary condition of the trust region minimization algorithm. The penalty number is only a stabilizer of the discontinuous Galerkin method in contrast to the condition $\eta \gg \sigma_c/\delta_c$ of Lorentz [91], which is necessary for existence and stability. Later in Chapter 3, it will be shown, however, that convexity in this context is equivalent to a minimum mesh resolution criterion necessary for obtaining accurate dissipated fracture

energies (see Equation (2.24) below).

Remark 3. *C^2 differentiability of the potential.* The usual theorems that guarantee success of the trust region method assume that the objective function is twice C^2-differentiable. Even though the smoothed interface potentials (2.15) and (2.16) are only C^1-differentiable, the trust region algorithm performed satisfactorily in all of our numerical experiments. Twice differentiable smoothed potentials can be constructed, e.g., using cubic splines [116] or the sigmoid smooth step function [31].

2.5 Time integration and the dynamic energy

In this section, we present the time domain discretization scheme and the proposed "time-discretized" energy functional π_{dyn}. Let us refer to the time-discrete case, with N time steps uniformly spaced by time intervals Δt: $t \in \{t_0 = 0, ..., t_{i-1}, t_i, ..., t_N = T\}$. Suppose that an equilibrium state is known at t_{i-1} and the equilibrium state at t_i is sought. We choose the potential π_{dyn} at time step t_i in such a way that

$$\nabla_{\mathbf{u}_i} \pi_{\text{dyn}} = \int_{\Omega \setminus \Gamma_d} \rho \ddot{\mathbf{u}}_i \, dV, \tag{2.20}$$

in which ρ is the material density and $\mathbf{u}_i$ and $\ddot{\mathbf{u}}_i$ are the finite difference approximations to $\mathbf{u}(t_i)$ and $\ddot{\mathbf{u}}(t_i)$, respectively. The dynamic energy π_{dyn} at t_i is a function of bulk acceleration only since the interfaces are massless. We now make use of the well-known implicit Newmark scheme [104] to establish the link between the displacement field $\mathbf{u}_i$ and its second and first time derivatives as

$$\ddot{\mathbf{u}}_i = \frac{2(\mathbf{u} - \widehat{\mathbf{u}}_i)}{a_1 \Delta t^2} \quad \text{where} \quad \widehat{\mathbf{u}}_i = \mathbf{u}_{i-1} + \Delta t \dot{\mathbf{u}}_{i-1} + (1 - a_1) \frac{\Delta t^2}{2} \ddot{\mathbf{u}}_{i-1}, \tag{2.21}$$

and

$$\dot{\mathbf{u}}_i = \dot{\mathbf{u}}_{i-1} + (1 - a_2) \Delta \ddot{\mathbf{u}}_{i-1} + a_2 \Delta t \ddot{\mathbf{u}}_i, \tag{2.22}$$

respectively, in which a_1 and a_2 are Newmark parameters, which, when $a_1 \geq a_2 \geq 0.5$, guarantee unconditional stability of the Newmark scheme (we used $a_1 = a_2 = 0.6$). In such setting, the size of Δt is limited by accuracy of the results and convergence of the iterative optimization algorithm rather than stability of the time integration scheme.

Inserting the time discrete relation for $\ddot{\mathbf{u}}_i$, from (2.21) into (2.20) and integrating the resulting equation with respect to $\mathbf{u}_i$, the appropriate form of the dynamic energy π_{dyn} is

obtained as a function of the unknown displacement $\mathbf{u}_i$ as

$$\pi_{\text{dyn}} = \frac{1}{a_1 \Delta t^2} \int_{\Omega \setminus \Gamma_d} \rho \mathbf{u}_i \cdot (\mathbf{u}_i - 2\widehat{\mathbf{u}}_i)\, dV, \tag{2.23}$$

where the constant of integration is dropped since the energy minimizer is independent of a constant additive term. Once the solution $\mathbf{u}_i$ is obtained, Equations (2.21) and (2.22) may be used to update the acceleration and velocity fields at t_i, respectively.

2.6 Numerical simulations

The proposed numerical algorithm was implemented in 2D using quadratic triangular finite elements. The examples that follow focus on convergence properties of the method and on asserting the method in a quasistatic, a low velocity, and a highly dynamic simulation. Because accuracy of the crack path for this class of models has already been analyzed in, e.g., [118], we have not used isoperimetric or other special meshes in most of the simulations. Interface elements were placed everywhere in the mesh from the start of the simulations as potential sites of crack nucleation and propagation. Numerical integration on interface elements was performed with 3-point Gauss quadrature so that three points holding discontinuity degrees of freedom were introduced in each interface. Unless otherwise mentioned, the simulations were performed with 15 continuation steps and continuation parameters $\delta_e^0 = 0.1\delta_c$, $\delta_e^{\text{tol}} = 2^{-15}\delta_e^0$ and $\widehat{\delta}_c^0 = 500\delta_c$. The tolerances used for the trust region algorithm were $\text{tol}_{\mathbf{g}} = 1 \times 10^{-4}$ and $\text{tol}_{\pi} = 1 \times 10^{-5}$. In all simulations, the length of the cohesive zone was estimated as [12]

$$l_c = a \frac{E' G_c}{\sigma_c^2}, \tag{2.24}$$

where $E' = E$ for plain stress, $E' = E/(1-\nu^2)$ for plain strain, E is the Young's modulus, ν is Poisson's ratio, and a is a coefficient taken as $\pi/8$ according to Barenblatts cohesive crack theory [11].

2.6.1 Convergence studies

Spatial convergence study: rectangular block with a weak interface

In this problem, we study convergence of the finite element solution with mesh refinement. The problem considered for this purpose is that of a weak interface subjected to combined

loading, as summarized in Figure 2.6a. The horizontal and vertical displacements $\widetilde{u}_x$ and $\widetilde{u}_y$ applied to the top edge of the block are monotonically increased in a quasi-static fashion until complete failure of the interface, while the bottom edge is fixed in both directions. The problem was solved with a sequence of six meshes, each one being embedded in the former, with element size twice smaller. For simplicity, and since it does not affect crack propagation (the crack forms along the weak interface), structured meshes were used. Figure 2.6b shows an illustration of the first and second levels of refinement (shown in thick and thin lines, respectively). For the material properties considered, the length of the cohesive process zone, according to (2.24), is $l_c \simeq 0.52$ mm. This length is discretized with approximately one interface element in the coarsest mesh and 32 interface elements in the finest mesh so that adequate resolution is ensured with mesh refinement.

The finite element solution obtained using the finest (sixth) mesh is taken to be the "exact" solution, and the normalized error in the displacement norm is defined as

$$e_u = \frac{\sqrt{\int_{\Omega_h \setminus \Gamma_{d,h}} (\mathbf{u}_{\text{exact}} - \mathbf{u}_h) \cdot (\mathbf{u}_{\text{exact}} - \mathbf{u}_h)\, dV}}{\sqrt{\int_{\Omega_h \setminus \Gamma_{d,h}} \mathbf{u}_{\text{exact}} \cdot \mathbf{u}_{\text{exact}}\, dV}}. \tag{2.25}$$

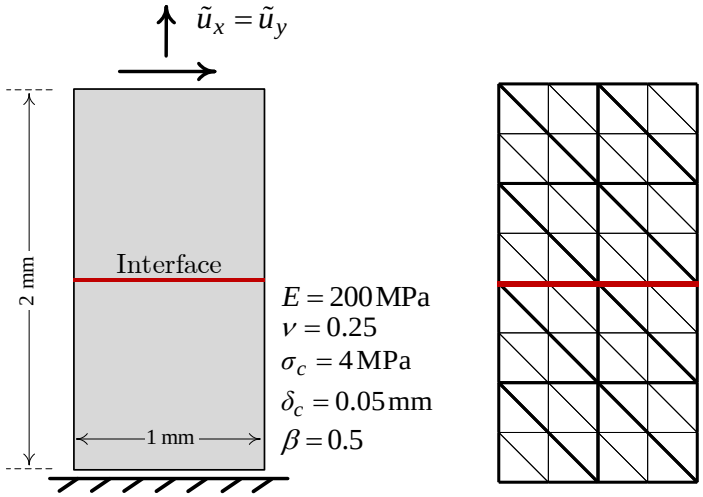

(a) (b)

Figure 2.6: a) schematic of a rectangular block with a horizontal weak interface and b) the first and second levels of mesh refinement used in the computation of convergence rates. The number of elements in mesh i is 4^{i+1} $(i = 1 : 6)$

The rate of convergence in the displacement error norm is computed at two different times t_1 and t_2, corresponding to pre- and post-failure of the interface, respectively. In addition, three values of $\chi = 2$, 5 and 10 in equation (2.8) have been considered in each case in order to show that the solution is independent of the penalty parameter η. Results are shown in Figure 2.7. Both pre- and post-failure, the estimated asymptotic rate of convergence in e_u is approximately 2.9, which is very close to the expected rate of 3 known for quadratic elements in the absence of cracks; robustness of the finite element solution is preserved in the post-failure regime and the opening of the interface does not introduce any degradation of convergence compared to the elastic condition. To provide further comparison, convergence results of the continuous Galerkin elastic problem (i.e., no interface elements) are also included in the figures. The rate of convergence is also independent of the penalty parameter, as shown in the figure.

Additionally, we define e_g, a measure of violation of the constraint $\boldsymbol{g}_h = \mathbf{0}$, as

$$e_g = \frac{\sqrt{\int_{\Gamma_{d,h}} \boldsymbol{g}_h \cdot \boldsymbol{g}_h \, dS}}{\sqrt{1 + \int_{\Gamma_{d,h}} \boldsymbol{\delta}_h \cdot \boldsymbol{\delta}_h \, dS}}. \tag{2.26}$$

Convergence of e_g to 0 with mesh refinement is shown in Figure 2.8. The rate of convergence is approximately 1.9 in the asymptotic region and is nearly insensitive to the magnitude of

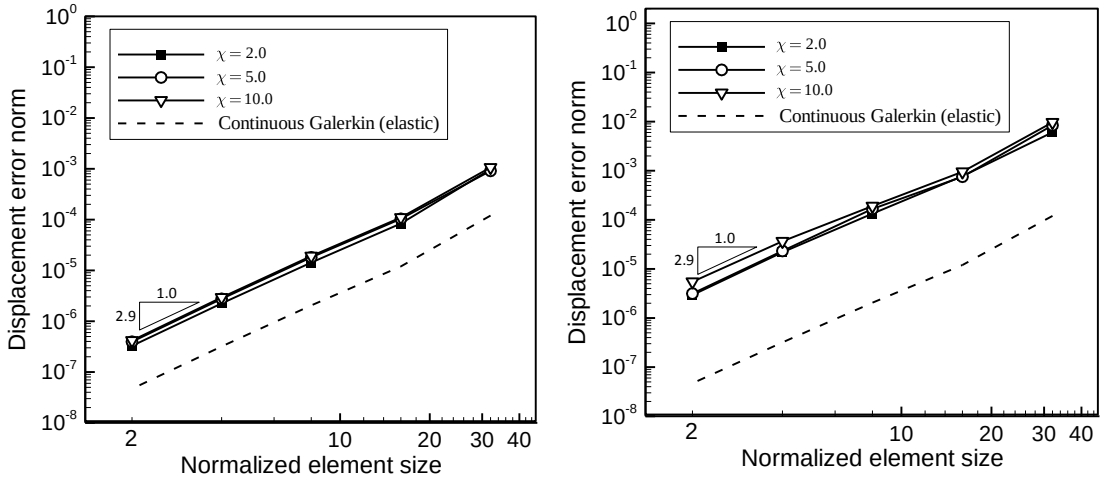

Figure 2.7: Convergence in displacement error norms for the square block with a horizontal weak interface at a) t_1 (pre-failure) and b) t_2 (post-failure)

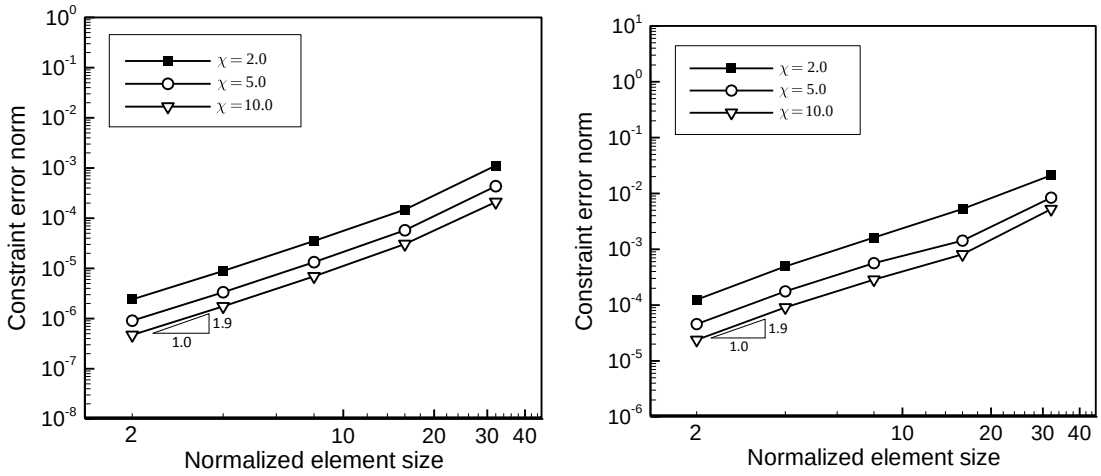

Figure 2.8: Convergence in constraint error e_g for the square block with a horizontal weak interface at a) t_1 (pre-failure) and b) t_2 (post-failure)

the penalty. This observation is a direct consequence of consistency and stability of the DG method and, together with the convergent behavior of e_u (Figure 2.7), ensures convergence of the local numerical flux $\boldsymbol{\lambda}_h^{\mathrm{DG}}$.

We note that there is no need to require σ_c/δ_c in order to guarantee convergence (in [91] $\eta \simeq 100\,\sigma_c/\delta_c$ is recommended). In our simulations, the penalty number η, equation (2.8) is as low as approximately $4\,\sigma_c/\delta_c$ in mesh 1, corresponding to $\chi = 2$. In all cases, the trust region algorithm converged within a reasonable number of iterations so that the maximum number of iterations encountered throughout the simulations was 12.

Figure 2.9 shows the variation of the vertical and horizontal forces with the applied displacements at the top of the block. Results are shown for the coarsest and finest meshes 1 and 6, respectively, using $\chi = 5$. The sum of areas under the vertical and horizontal force-displacement curves yields the work done on the applied displacements to complete failure of the interface, which equals 0.100042 N·mm for mesh 1 and 0.100013 N·mm for mesh 6. The computed external work agrees well with the energy dissipated at complete failure of the interface, whose value, obtained by multiplying the fracture energy by the area of the interface, is 0.1 N·mm.

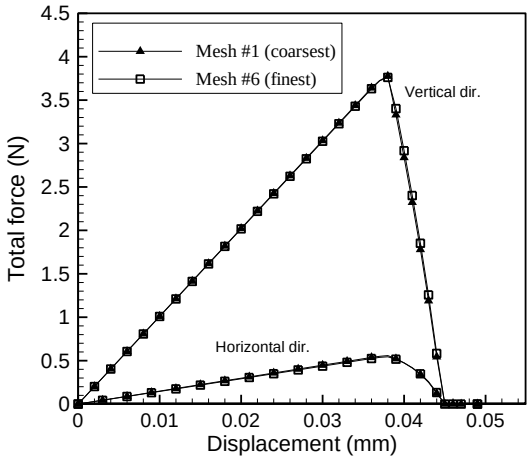

Figure 2.9: Force-displacement curves for the rectangular block with a weak interface

Time-continuity study: three-point bending test

We study temporal convergence in a mixed-mode problem of a beam subjected to impact loading in three-point bending. We note that time-continuity, as defined in [117], is an issue that affects temporal convergence in a dynamic mixed mode setting and does not affect mode-I crack propagation. Because the method herein does not correspond to a time discretization of a differential equation, the difficulty of time-discontinuity is bypassed, therefore we expect, although no proof of this yet exists, the rate of convergence with decreasing time step to be approaching quadratic.

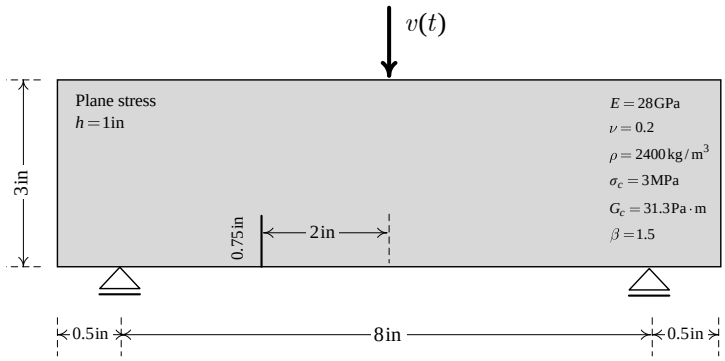

Figure 2.10: Time-continuity studies: schematic of the three-point bending test

The problem, summarized in Figure 2.10, was investigated experimentally by John and

Shah [76] and studied numerically by several authors [139, 140]. Dynamic loading due to impact at the top-centre of the beam is modeled by an imposed velocity boundary condition

$$v(t) = \begin{cases} v_0 t/t_r & t < t_r \\ v_0 & t \geq t_r \end{cases} \tag{2.27}$$

in which $v_0 = 0.05$ ms and the rise time is $t_r = 196\,\mu$s.

The FE mesh employed consists of 864 structured 6-noded triangles and 1248 6-noded interface elements with a total of 5184 nodal points. The obvious bias that the structured mesh introduces to the crack path is not important here since this example is only concerned with temporal convergence of the results and not with accuracy of the crack trajectories.

In order to perform the temporal convergence study, different time step sizes Δt_i were used, where $\Delta t_i = 1 \times 10^{-5}/2^i$ s, $i = 0:5$. The normalized error in the displacement field obtained with time step Δt_i is defined as $e_{\Delta t_i} = \|\mathbf{U}_i - \mathbf{U}_{\text{exact}}\|/\|\mathbf{U}_{\text{exact}}\|$, where $\mathbf{U}_{\text{exact}}$ is taken to be the solution obtained from the finest time step (i.e., $i = 5$). Figure 2.11 shows convergence of this norm at two instants of the simulation, $t_1 = 220\,\mu$s, which corresponds to a condition before any damage has initiated, and $t_2 = 1025\,\mu$s, which corresponds to a post-failure condition, as the time step size is refined. It is seen that the proposed nondifferentiable energy minimization algorithm exhibits the second order asymptotic rate of convergence expected of the Newmark scheme in both the pre- and post-failure regimes.

To provide further comparison, convergence results obtained from a hybrid DG-cohesive element method similar to that proposed in [129] are also plotted in the figure. A brief

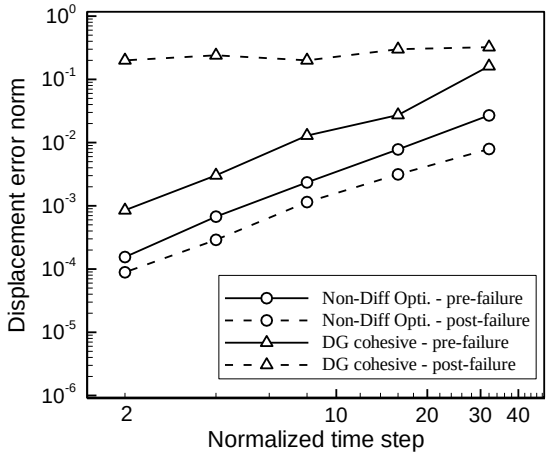

Figure 2.11: Temporal convergence results for the three-point bending test. The normalized time step is defined as Δt_i divided by the smallest time step

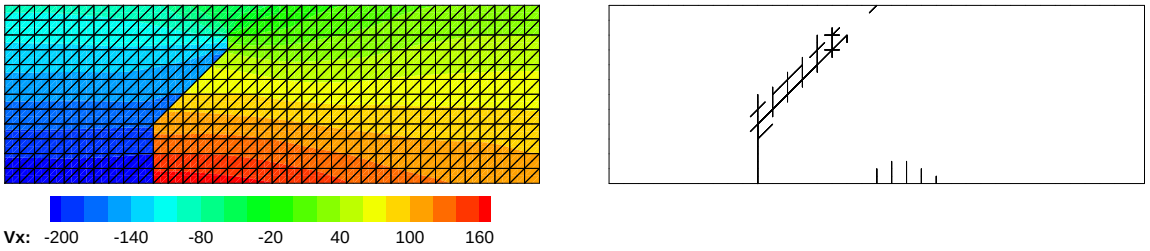

(a)

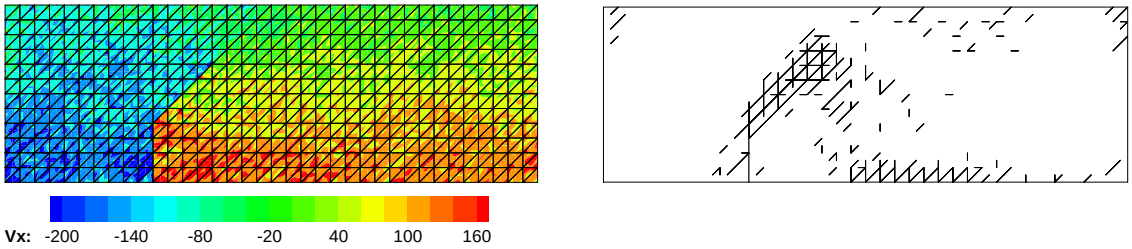

(b)

Figure 2.12: Contours of the horizontal component of the velocity field $\dot{u}_x$ (left) and activation patterns (right) for the a) time-continuous and b) time-discontinuous models at $t_2 = 1025\,\mu$s. Color bar in mm/s

description of our implementation of this method, which is time-discontinuous, is as follows. The DG method is used to tie together the element edges prior to the nucleation of cracks. Upon satisfaction of a fracturing criterion, the DG terms cease to operate and give place to the tractions computed from a cohesive traction-separation model. The time-stepping method employed to obtain the results with this method was the explicit central difference scheme with $\Delta t \simeq 0.1\Delta t_{\text{cr}}$, where Δt_{cr} is the critical time step size of the explicit scheme. An implicit time-stepping was not possible due to the interference of the failure criterion with the iterative solution algorithm. The DG-cohesive element method shows nonconvergent behavior in the post-failure regime, typical of the behavior resulting from discontinuity of internal forces at the time of activation [117, 140].

Figure 2.12 shows contours of the horizontal component of the velocity field $\dot{u}_x$ and the activation patterns obtained from (a) the proposed method and (b) the time-discontinuous method, both at time $t_2 = 1025\,\mu$s (post-failure). The results of the time-discontinuous model show nonphysical irregularities in the velocity contours and overactivation of interfaces. The irregularities do not disappear with mesh or time step refinement, indicative

of unphysical response resulting from numerical instability, namely the discontinuous dependence of internal forces on the deformation field creating unphysical "shocks" when an interface point activates. The shocks, in turn, lead to unphysical forces that may overactivate the interfaces at random locations. This is typical behavior of methods that rely on an extrinsic failure criterion, see e.g. [95].

2.6.2 Quasi-static simulation: single-edge notched beam

We reproduce here the experimental results of Galvez et al. [52] on mixed-mode crack propagation in a single-edge notched concrete beam. The problem setting, including relevant mechanical properties, boundary conditions, and dimensions is summarized in Figure 2.13. The characteristic length of the material obtained from (2.24) is $l_c = 84$ mm. This is comparable to a limiting geometrical dimension of the beam, and thus, the simulation corresponds to "large-scale" yielding conditions as is typical for concrete structures.

Two finite element meshes were used for the numerical simulation of the beam. The "coarse" mesh consists of 1575 triangular elements and 2304 interface elements, and the "fine" mesh consists of 3508 tiangular elements and 5172 interface elements. Both meshes are finer in a region ahead of the notch tip for better resolution of the crack path. The deformed geometry of the beam obtained using the fine mesh is shown in Figure 2.14. Figure 2.15 shows a comparison of the dominant crack trajectories, obtained using both meshes, with the experimental envelope reported by Galvez et al. [52]. Some interface activations at the top edge of the beam, either not shown or not visible in the figures, was observed, as also noted in the experiments of Galvez et al. [52]. Although the experimental crack path was challenging to reproduce with a randomly oriented mesh and some realignment was

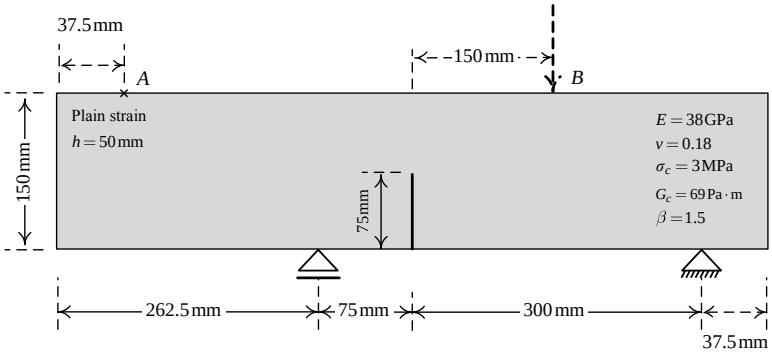

Figure 2.13: Single-edge notched beam; problem setting and relevant mechanical properties

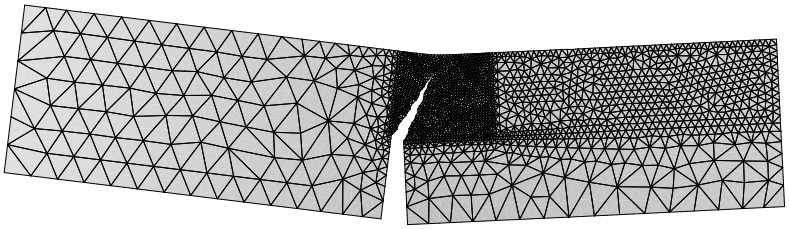

Figure 2.14: Deformed geometry (magnified by a factor of 100) of the single edge notched beam using the fine finite element mesh at 0.075 mm vertical displacement applied at point B

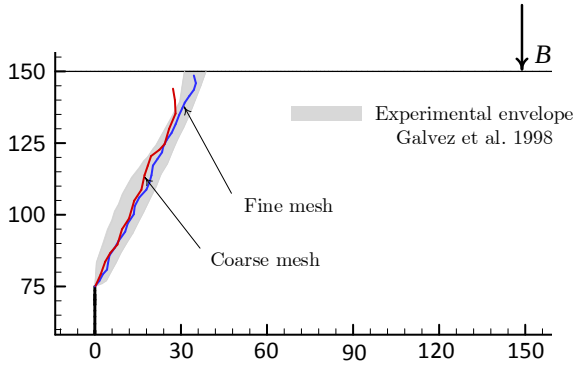

Figure 2.15: Comparison of the dominant crack trajectories with the experimental envelope of Galvez et al. [52]

necessary, the numerical and experimental results are in good agreement, which improves with mesh refinement. Special meshes [118, 122], which would facilitate the task, were not used in this simulation.

Figure 2.16 shows load-deflection curves at a point, denoted A in Figure 2.13, and load-crack mouth opening displacement (CMOD) curves obtained using the present method, along with the experimental envelopes reported by Galvez et al. [52] and numerical results reported by Areias and Belytschko [5], who used a 3D model with regularized unloading. Results show favorable agreement, and little mesh dependence is observed in the global response of the beam.

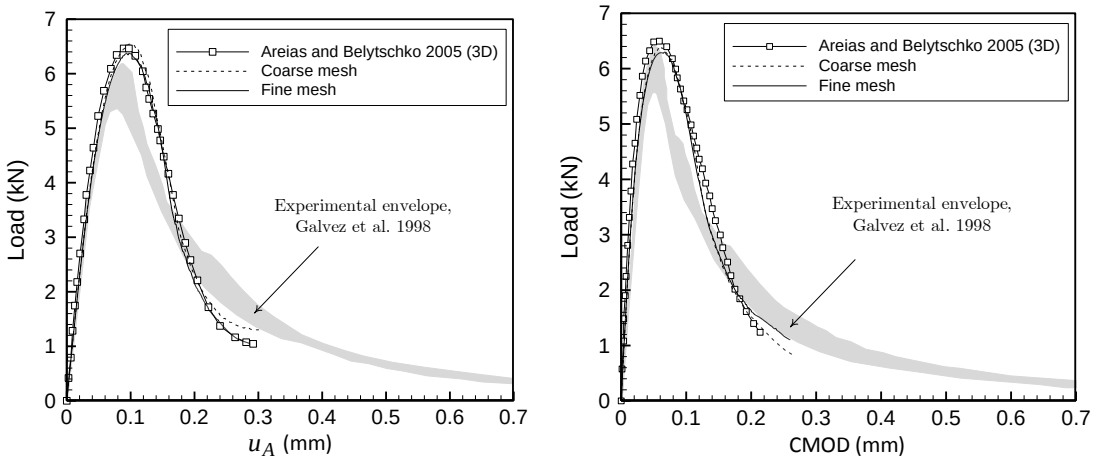

(a) (b)

Figure 2.16: a) load-displacement of point A and b) load-CMOD curves for the single edge notched beam. Experimental envelopes from the work of Galvez et al. [52] and numerical results reported by Areias and Belytschko [5] are also shown

2.6.3 Low-velocity impact: compact compression specimen

In this example, we model an unpublished experiment. on a Compact Compression Specimen (CCS) similar to the one performed by Rittel and Maigre [138]. This specimen is a horseshoe-shaped thin notched polymethymethacrylate sample, which is struck by a split-Hopkinson bar on one of its cantilever arms. The schematic of the experiment and specimen dimensions, together with the relevant material properties, are shown in Figure 2.17. A curved crack initiates at the tip of the notch and eventually splits the sample into two pieces. The Hopkinson bar strike is modeled by a time-dependent uniform pressure applied on the contact surface between the Hopkinson bar (diameter 12.7 mm) and the specimen. The time history of the resultant impact load used in the numerical simulation, shown in Figure 2.18, was obtained from experimental measurements made at 260 equally spaced times. Every other surface is traction free, and no displacement boundary condition is applied.

The finite element mesh used for the numerical simulation contains 822 bulk elements and 1171 interface elements. In order to capture the true crack path more accurately, most of the elements are clustered in the crack-path zone, the area ahead of the tip of the notch, see Figure 2.19. The mesh in the crack-path zone is chosen to be of the pinwheel isoperimetric type [118], which possesses the property that, for any curve in the computational

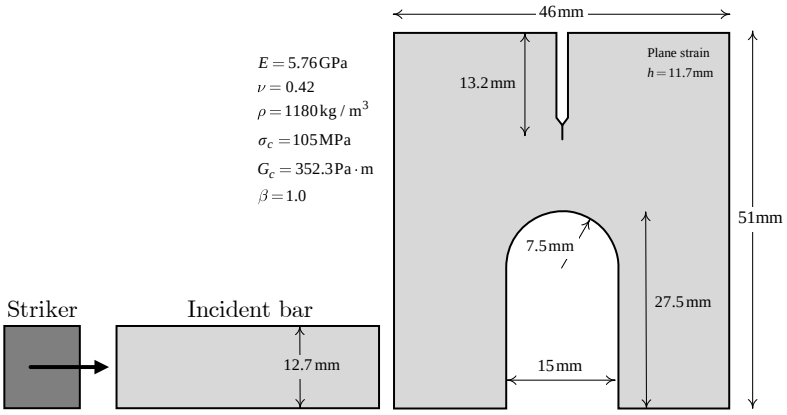

Figure 2.17: Compact compression specimen; experiment setup and model dimensions

domain, there is an approximation using mesh edges that tends to the curve, including a correct representation of its length, as the grid size tends to zero. It was shown [118, 55] that the isoperimetric property is a necessary condition for any possible spatial convergence proof in cohesive zone modelling in the general case that the crack path is not known in advance. The minimum andmaximum element sizes in the crack-path zone are $h_{\min} \simeq 0.0231$ mm and $h_{\max} \simeq 0.0512$ mm so that the cohesive process zone is discretized with adequate resolution in this area (the characteristic length is $l_c = 0.075$ mm). The remainder of the mesh is generated by Delaunay triangulation.

The impact velocity of the incident bar is low (approximately 30 m/s) compared to the dilatational wave speed in the material, which is $v_d = 2846$ m/s, as calculated from equation 4 of [60]. This justifies use of the implicit scheme proposed here. A time step $\Delta t = 0.2\,\mu$s was used in the computations for a total simulation time of $T = 110\,\mu$s, whereas an explicit time step would be limited by the time required for the dilatational wave to travel across the smallest element of the mesh, which is $h_{\min}/v_d \simeq 0.008\,\mu$s.

Figure 2.20 shows the final deformed shape of the specimen obtained from the numerical simulation and from the experiment. The numerical and experimental crack trajectories show excellent agreement; the overall crack path curves to the left, and the initiation angle is approximately 45° with respect to the vertical. In our simulations, the crack initiated at $t_0 = 56.4\,\mu$s, which is again in good agreement with the experimentally observed initiation time of $t_0 = 66\,\mu$s. Additionally, the numerical results obtained are consistent with the numerical results reported in other works [116, 118, 122].

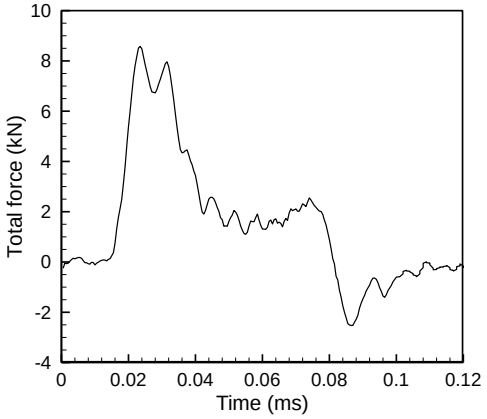

Figure 2.18: Time history of total impact load in the CCS experiment

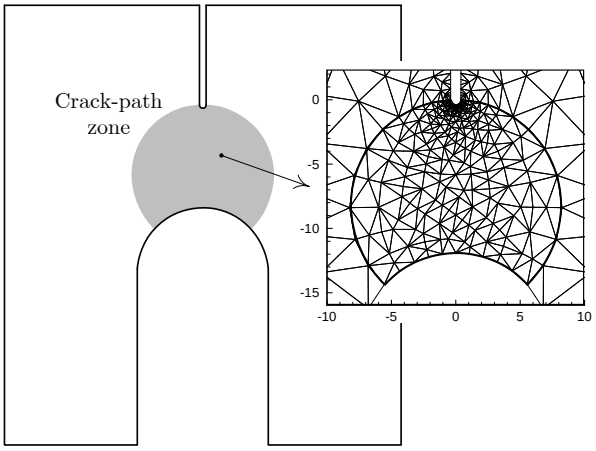

Figure 2.19: The crack-path zone is shaded in grey. This zone is meshed with a pinwheel isoperimetric mesh. The region of the CCS geometry outside the crack-path zone is meshed using Delaunay triangulation. Dimensions are in mm

2.6.4 Dynamic fragmentation of a thick cylinder

In order to demonstrate the capabilities of the proposed algorithm in modelling multiple crack growth problems, we consider the fragmentation of a thick cylinder subjected to an impulsive internal pressure, previously studied by Song and Belytschko [153]. The problem setup, material properties, and time history of the applied pressure are shown in Figure 2.21. The internal pressure decays exponentially with time as $p(t) = p_0 e^{t/t_0}$, where $p_0 = 400$

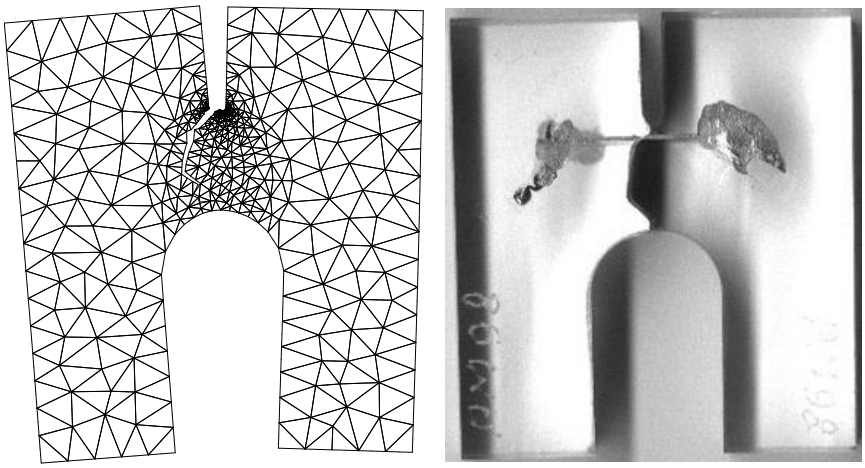

(a) (b)

Figure 2.20: Final deformed shape of the specimen obtained from a) numerical simulation and b) experiment by D. Rittel. Differences in deformation of the bulk may be due to modelling approximations, including those in modelling the striker

MPa and $t_0 = 100\,\mu$s. Similar problems have been studied previously by other researchers, see, e.g., [128].

The problem was solved using two meshes with different levels of refinement. The coarse mesh had 1692 bulk elements, 2394 interface elements, and a total of 17334 nodal points (displacement + opening). The fine mesh had 5844 bulk elements, 8472 interface elements, and a total of 60480 nodal points. The minimum and maximum element sizes were $h_{\min} \simeq 1.2$ mm, $h_{\max} \simeq 3.4$ mm in the coarse mesh and $h_{\min} \simeq 0.6$ mm, $h_{\max} \simeq 1.8$ mm in the fine mesh. The characteristic length of the material obtained from the parameters (Figure 21) is $l_c = 2.8$ mm. The size of the coarse mesh appears to be relatively large compared with this characteristic length. However, as will be shown below, results obtained by both meshes show convergent behavior in terms of the energy dissipated during fragmentation.

Because of the homogeneity of the material strength, cracks are expected to form everywhere along the inner surface of the cylinder when a critical level of loading is reached. Additionally, as finer meshes provide more sites for the initiation of cracks, one expects the number of crack nucleation sites to keep increasing with any level of mesh refinement, leading to obvious mesh dependence of the results. Zhou and Molinari [182] proposed a method to address mesh dependence, in which the strengths of cohesive elements were chosen to follow a modified weakest link Weibull distribution. In a somewhat similar ap-

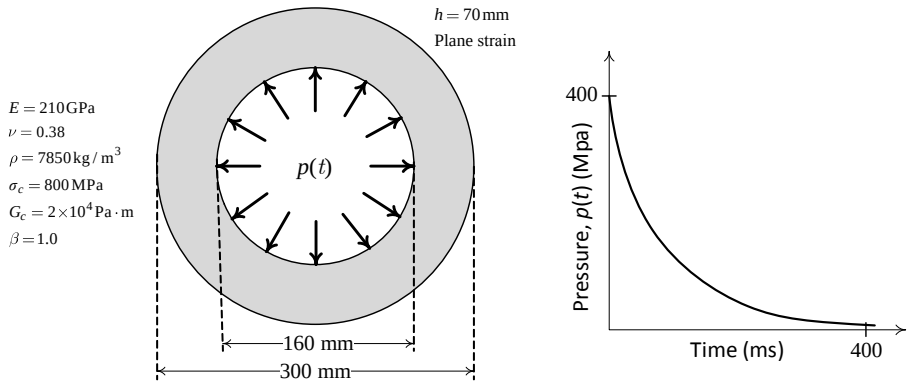

Figure 2.21: Problem setup for fragmentation of a thick cylinder under impulsive internal pressure

proach, we counter mesh dependence by introducing randomness in the critical strength of the cohesive model. The randomness introduced has a normal distribution over the computational domain with %2 standard deviation. So as to avoid mesh dependence of the random distribution, a background material mesh was constructed that serves to interpolate the random variable at each point of the domain using its nodal values. In this manner, the location and number of the fragments are dominated by the distribution of the material strength rather than by the configuration and size of the mesh.

Given that the dilatational wave speed in the material is $v_d = 5591$ m/s, an explicit time step would be limited by $h_{\min}/v_d \simeq 0.2\,\mu$s in the coarse mesh and $h_{\min}/v_d \simeq 0.1\,\mu$s in the fine mesh. We performed the simulations using $\Delta t = 0.3\,\mu$s for a total time within $T = 78\,\mu$s. This choice of the time step size was made to ensure the accuracy of the results and convergence of the trust region iterations. With the exception of the first continuation iteration within time steps involving multiple interface activations, which took up to 22 trust region iterations to converge, the trust region algorithm converged in at most 6 iterations throughout the computations for both meshes. Crack initiation along the inner surface of the cylinder started at around $33\,\mu$s in the coarse mesh and $32.1\,\mu$s in the fine mesh. Figure 2.22 shows the final deformed configuration and the activation patterns obtained by the two meshes. The overall fragmentation and failure patterns are similar in both cases even though arrested small cracks are more frequently observed in the fine mesh simulation. The number of fragments is 13 in the coarse mesh and 14 in the fine mesh, yet the approximate locations of fragments and failure patterns are in good agreement. We note that the fragmentation patterns obtained correspond to the particular distribution of the material strength considered. Other researchers have reported different numbers of

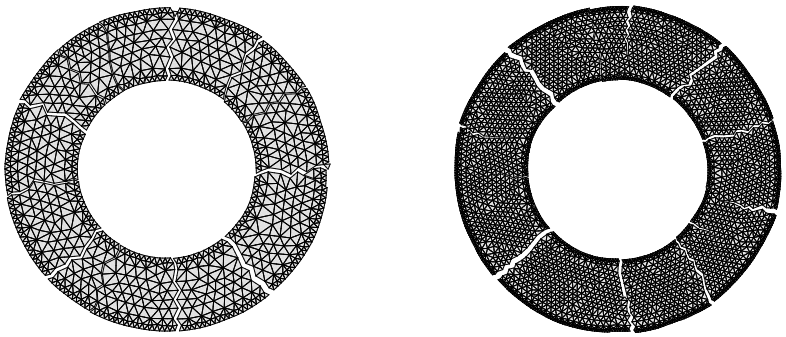

(a)

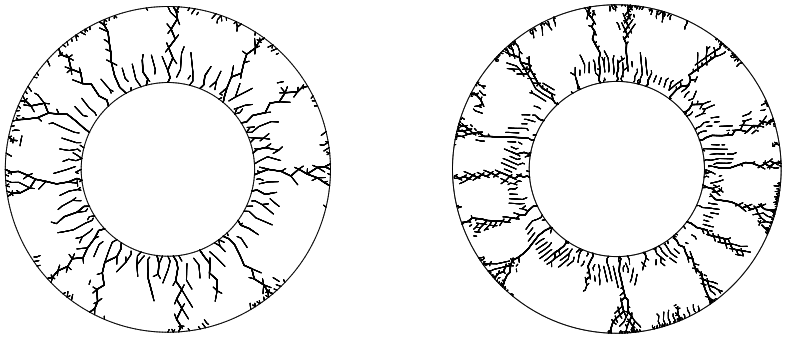

(b)

Figure 2.22: a) Final deformed configuration (magnified by a factor of 10) and b) interface activation patterns of the coarse and fine meshes at $t = 78\,\mu$s

fragments. For instance, 12 to 16 fragments were obtained by Rabczuk and Belytschko [128] whereas 18 to 20 fragments were obtained by Song and Belytschko [153] depending on the size of the meshes used.

Figure 2.23 shows the time histories of the cohesive fracture energy for the coarse and fine meshes. The rate of energy dissipation is very steep at the early stages of fragmentation but becomes nearly constant after most cracks are arrested. The dissipated fracture energies obtained from the two meshes are in good agreement, indicating that the dissipated energy is independent of the size of the mesh.These results are very encouraging and make the proposed nondifferentiable energy minimization approach an appealing candidate for tackling even more complicated crack propagation problems.

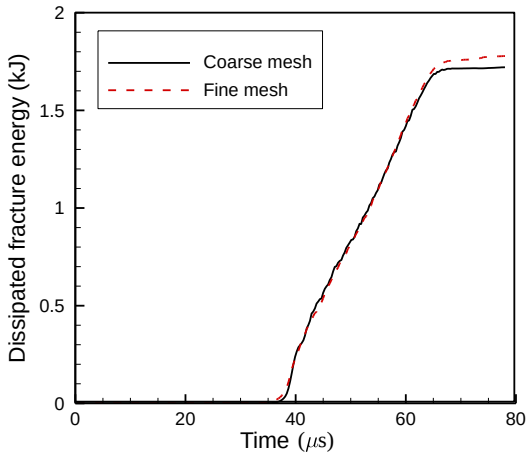

Figure 2.23: Time histories of dissipated cohesive energy for dynamic fragmentation of a thick cylinder

2.7 Conclusions

A nondifferentiable energy minimization approach for crack initiation and propagation involving initially rigid cohesive interfaces was proposed that does not require a fracturing criterion as a separate entity from the minimization process. In keeping with energy approaches to fracture, the approach has a firm physical basis and bypasses the time-discontinuity issue previously observed in the literature. This was demonstrated through mesh refinement and time convergence studies, and the smoothness of velocity contours. The proposed formulation incorporates momentum into the energy functional, extending the application of the energy minimization approach to dynamic problems. Unlike other methods for initially rigid cohesive fracture, the method is naturally amenable to implicit time-stepping.

The method preserves the consistency and stability of the numerical scheme in both pre-failure and post-failure conditions. In particular, the expected rate of convergence in displacement error norms was recovered in our numerical experiments. The capabilities of the method in modelling quasistatic to truly dynamic crack propagation problems were exemplified through various examples.

Chapter 3

Block coordinate descent energy minimization for dynamic cohesive fracture

This chapter is based on the following journal article:

Hirmand MR and Papoulia KD, Block coordinate descent energy minimization for dynamic cohesive fracture. *Computer Methods in Applied Mechanics and Engineering*, in review (2019), Manuscript ID: CMAME-D-18-01800.

This paper was co-authored by myself and my supervisor, Dr. Katerina Papoulia. I developed the mathematical and computational formulation and implemented a computer program to conduct the numerical simulations. I also wrote the manuscript. Dr. Papoulia provided supervisory guidance through overseeing formulations and editing the manuscript. At the time of this writing, the paper is under revision.

3.1 Introduction

The continuation strategy proposed in the previous chapter has its merits, particularly in quasi-static settings but is computationally expensive for large models. In the present chapter, we develop a new computational algorithm based on block coordinate descent (Block-CD) minimization within the discontinuous Galerkin finite element framework. The method allows a simple and robust implementation of the nondifferentiable energy minimization algorithm for rigid-cohesive fracture that can be easily implemented in standard finite element codes.

Block coordinate descent methods are iterative optimization algorithms, in which each iterate is obtained by minimizing the objective with respect to one *block* of unknowns while other blocks of unknowns are held fixed at their values from the previous iteration [175, 15]. As each sub-problem is a lower dimensional minimization problem, it can typically be solved more easily than the full problem. In recent years, block-CD methods have found increased popularity in data analysis and machine learning applications, see e.g., [137, 22]. In the context of structural analysis, and in particular in recent phase-field models of fracture, block-CD minimization methods are encountered as operator split or staggered iteration strategies , see e.g. [97]. Convergence of a block-CD method for nondifferentiable minimization was studied in [163].

In our setting, a block-CD algorithm proves significantly advantageous as it allows to efficiently separate the unknowns, in which the potential is nondifferentiable in small blocks from the block of unknowns, in which the potential is differentiable. Furthermore, both implicit and explicit time-stepping schemes can be used to advance the solution of the minimization problem in time. In each iteration or each explicit update, the algorithm minimizes the potential with respect to each crack opening displacement unknown and with respect to the block of deformation unknowns, sequentially. This decomposes minimization of the full nondifferentiable problem into a number of "small" nondifferentiable sub-problems that must be solved locally at the inter-element boundaries of the finite element mesh and an "easy" differentiable sub-problem that characterizes global equilibrium. As a consequence, nondifferentiablity can be treated with great flexibility using generalized differential calculus of nonsmooth optimization theories [32, 33]. On the basis of a convexity analysis of the proposed nondifferentiable energy functional, we obtain a minimum cohesive process zone resolution criterion, known empirically in the previous literature as a requirement for capturing correctly the amount of dissipated fracture energy. The method is free of any regularization parameters and preserves the discrete nature of fracture while allowing for a smooth transition at crack initiation. Robustness of the method is shown through several numerical examples of fragmentation and branching and through

comparisons with existing numerical and experimental results.

This chapter is structured as follows. Section 3.2 briefly presents the formulation of the energy approach for cohesive fracture. Section 3.3 presents the proposed block-CD algorithm for nondifferentiable energy minimization in a DG setting. The update of opening displacement unknowns entails solution of an algorithmic nondifferentiable energy minimization problem locally at the interface elements of the finite element mesh which is discussed in Section 3.4. Section 3.5 presents a number of numerical simulations which show the robustness of the method and exemplify its capabilities in modelling dynamic problems involving branching and fragmentation. Finally, Section 3.6 offers concluding remarks and suggests future research.

3.2 Formulation of the energy approach

A solid body $\Omega \subset \mathbb{R}^{n_{\text{dim}}}$ ($n_{\text{dim}} = 2, 3$) is considered, which is bounded externally by $\partial\Omega$ and contains an evolving $(n_{\text{dim}} - 1)$-dimensional surface $\mathcal{S}$ in the interior of its domain representing cracks, as shown in Figure 3.1. The external boundary $\partial\Omega$ consists of disjoint parts $\partial_u\Omega$ and $\partial_t\Omega$ ($\partial_u\Omega \cap \partial_t\Omega = \emptyset$ and $\partial_u\Omega \cup \partial_t\Omega = \partial\Omega$), on which the possibly time-dependent displacement $\widetilde{\mathbf{u}}$ and external traction $\widetilde{\mathbf{t}}$ are prescribed, respectively. Let $\mathbf{u}(\mathbf{x}, t) : \Omega \to \mathbb{R}^{n_{\text{dim}}} \times [0, T]$ be the displacement of the fractured body, which is continuous and differentiable everywhere in $\Omega \backslash \mathcal{S}$ except for nonzero jumps across $\mathcal{S}$. To overcome the complexities associated with treating crack surfaces $\mathcal{S}$ as an unknown of the energy minimization formulation, we restrict evolution of $\mathcal{S}$ to a set of *a priori* known discontinuity boundaries $\Gamma_d \subset \Omega$. These represent potential crack paths so that $\mathcal{S} \subseteq \Gamma_d$ throughout the course of crack propagation. Consistent with this assumption, the displacement is allowed to admit a jump $[\![\mathbf{u}(\mathbf{x}, t)]\!]$ everywhere on Γ_d. An auxiliary discontinuity opening displacement field $\boldsymbol{\delta}(\mathbf{x}, t) : \Gamma_d \to \mathbb{R}^{n_{\text{dim}}} \times [0, T]$ is then defined that tracks the evolution of $\mathcal{S}$ in Γ_d by requiring that

$$\boldsymbol{g}(\mathbf{u}, \boldsymbol{\delta}) \equiv [\![\mathbf{u}(\mathbf{x}, t)]\!] - \boldsymbol{\delta}(\mathbf{x}, t) = \mathbf{0} \quad \text{on } \Gamma_d. \tag{3.1}$$

It follows from the above formulation that $\mathcal{S}(t) = \{\mathbf{x} \in \Gamma_d \,|\, \boldsymbol{\delta}(\mathbf{x}, t) \neq \mathbf{0}\}$. The complete state of deformation and fracture of the body is thus described by two independent unknowns, namely $\mathbf{u}$ and $\boldsymbol{\delta}$.

The normal and sliding components of the opening are defined as $\delta_n = \boldsymbol{\delta} \cdot \mathbf{n}_d$ and $\boldsymbol{\delta}_s = \boldsymbol{\delta} - \delta_n \mathbf{n}_d$, where $\mathbf{n}_d$ is the normal to the discontinuity. For convenience of the subsequent presentation, we also define a unit tangent to the discontinuity, $\mathbf{m}_d$, and a scalar sliding component, δ_s, so that $\boldsymbol{\delta}_s = \delta_s \mathbf{m}_d$ and $|\delta_s| = \|\boldsymbol{\delta}_s\|$. A similar notation is

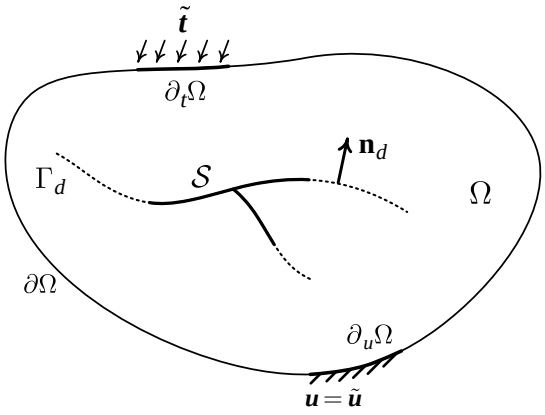

Figure 3.1: Schematic of a solid body Ω containing evolving crack surfaces $\mathcal{S}$. The discontinuity boundary Γ_d represents potential crack paths.

employed throughout this chapter for the normal and sliding components of other vector quantities (e.g., tractions).

In the context of quasi-brittle fracture, we assume infinitesimal deformation and consider the bulk of the material governed by the standard theory of linear elasticity for isotropic solids. The strain energy density function ψ is defined on the "uncracked" part of the body $\Omega\backslash\Gamma_d$ as $\psi(\boldsymbol{\varepsilon}(\mathbf{u})) = \frac{1}{2}\boldsymbol{\varepsilon}(\mathbf{u}) : \mathbf{D} : \boldsymbol{\varepsilon}(\mathbf{u})$, where $\mathbf{D}$ is the elasticity constitutive tensor and $\boldsymbol{\varepsilon}(\mathbf{u}) = \nabla^s\mathbf{u} \in \mathbb{R}^{n_{\text{dim}}} \times \mathbb{R}^{n_{\text{dim}}}$ is the strain tensor defined as the symmetric part of the displacement gradient. Further, we define a cohesive surface energy function $\psi_{\text{cohs}}(\boldsymbol{\delta})$, which, as mentioned in the introduction, depends nontrivially on $\boldsymbol{\delta}$ and is, in particular, a nondifferentiable function of $\boldsymbol{\delta}$ at $\boldsymbol{\delta} = \mathbf{0}$ before a crack initiates on Γ_d. The latter is a mandatory requirement for the model to produce zero opening displacement on Γ_d until a critical state of tensile stress is reached [30, 116]. Interpenetration of the crack faces is prohibited through the indicator function $I_{\mathbb{R}^+}(\delta_n)$, which introduces infinite energy for $\delta_n < 0$. The precise form of these functions will be discussed in a following subsection where an internal history variable is also introduced that takes into account the irreversibility of the fracturing processes.

An expression of the total potential energy of the body is obtained as a the sum of the strain energy due to bulk deformation $\pi_{\text{el}}(\mathbf{u})$, the dynamic energy due to momentum change $\pi_{\text{dyn}}(\mathbf{u})$, the energy due to opening of the interfaces $\pi_{\text{intf}}(\boldsymbol{\delta})$, and the energy due to the work of external forces $W_{\text{ext}}(\mathbf{u})$,

$$\pi(\mathbf{u}, \boldsymbol{\delta}) = \pi_{\text{el}}(\mathbf{u}) + \pi_{\text{dyn}}(\mathbf{u}) + \pi_{\text{intf}}(\boldsymbol{\delta}) - W_{\text{ext}}(\mathbf{u}), \tag{3.2}$$

where

$$\pi_{\text{el}}(\mathbf{u}) = \int_{\Omega\setminus\Gamma_d} \psi\left(\boldsymbol{\varepsilon}(\mathbf{u})\right)\, dV,$$
$$\pi_{\text{intf}}(\boldsymbol{\delta}) = \int_{\Gamma_d} \left(\psi_{\text{cohs}}(\boldsymbol{\delta}) + I_{\mathbb{R}^+}(\delta_n)\right)\, dS, \tag{3.3}$$
$$W_{\text{ext}}(\mathbf{u}) = \int_{\Omega\setminus\Gamma_d} \mathbf{u}\cdot\,\mathbf{b}\, dV + \int_{\partial_t\Omega} \mathbf{u}\cdot\,\widetilde{\mathbf{t}}\, dS,$$

and $\mathbf{b}$ is a vector of body forces per unit volume. Following [73, 116] and because a time-dependent potential is generally difficult to achieve, the dynamic potential $\pi_{\text{dyn}}(\mathbf{u})$ is chosen in such a way that the following relation holds at each time step within a time-discrete framework:

$$\nabla_{\mathbf{u}_i}\pi_{\text{dyn}} = \int_{\Omega\setminus\Gamma_d} \rho\ddot{\mathbf{u}}_i dV, \tag{3.4}$$

where ρ is the bulk density and the subscript i denotes the finite difference approximation to the unknown fields at time step t_i of discretized time domain. In contrast to [73, 116], the exact form of $\pi_{\text{dyn}}(\mathbf{u})$ does not need to be determined explicitly in our minimization algorithm as will be shown in Section 3.3.

The equilibrium of the fractured body is then characterized by the solution of the following constrained minimization problem that must be solved at each time step:

$$\text{find } (\mathbf{u}^\star, \boldsymbol{\delta}^\star) \in \mathcal{U}\times\mathcal{D} \text{ minimizing } \pi(\mathbf{u},\boldsymbol{\delta}) \text{ subject to } \boldsymbol{g}(\mathbf{u},\boldsymbol{\delta}) = \mathbf{0}, \tag{3.5}$$

where $\mathcal{U}$ and $\mathcal{D}$ are spaces of admissible solutions and $\boldsymbol{g}(\mathbf{u},\boldsymbol{\delta})$ is a linear constraint function defined in (3.1) accounting for the compatibility of deformation fields on Γ_d.

3.2.1 The rigid-cohesive surface energy function

The cohesive energy ψ_{cohs} is of the type introduced by Barenblatt. For an isotropic material, ψ_{cohs} should be made a function of δ_n and $\|\boldsymbol{\delta}_s\|$, starting from 0 and progressively growing up to Griffith's energy G_c when the norm of opening displacement grows from 0 to infinity [30]. Here, we consider a general class of such models proposed by Ortiz and Pandolfi [113]. A scalar effective opening displacement δ is defined as

$$\delta = \sqrt{(\delta_n^+)^2 + \|\beta\boldsymbol{\delta}_s\|^2}, \tag{3.6}$$

where $\delta_n^+ = \max(0, \delta_n)$, and $\beta > 0$ is a constant to be defined shortly. We note that the dependence of ψ_{cohs} on positive values of the normal opening implies that ψ_{cohs} introduces no resistance against interpenetration of crack faces (i.e., $\delta_n < 0$ does not contribute to the potential); the non-penetration in compression/contact is enforced solely via the indicator function discussed below. We further note that, as shown in [30], the use of δ is essential for modelling failure in a continuum. If ψ_{cohs} is made a direct function of δ_n^+ and $\|\boldsymbol{\delta}_s\|$, the model corresponds to an adhesive interface.

To model the physical requirement that the fracturing process is irreversible, a non-negative history variable $\delta_{\max}(t)$ is introduced, which represents the maximum opening attained up until time t. This allows the interface to "remember" the level of damage induced as the crack evolves. The variable is initially zero and evolves monotonically in time as

$$\dot{\delta}_{\max} = \begin{cases} \dot{\delta} & \text{if } \delta = \delta_{\max} \text{ and } \dot{\delta} \geq 0 \\ 0 & \text{otherwise,} \end{cases} \tag{3.7}$$

so that $\dot{\delta}_{\max}(t) \geq 0 \, \forall t \geq 0$. The first of the above corresponds to the case of an interface point undergoing loading, while the second to an interface point that is unloading or reloading.

Let δ_c be an effective opening displacement at which ψ_{cohs} reaches the Griffith surface energy G_c and the interface looses cohesion, i.e., $\psi_{\text{cohs}}(\boldsymbol{\delta}; \delta_{\max}) = G_c$ for $\delta_{\max} \geq \delta_c$. We assume elastic linear behaviour in unloading/reloading and linear softening interface response in loading when $\delta_{\max} \leq \delta_c$, for which the *irreversible* cohesive potential may be written as

$$\psi_{\text{cohs}}(\boldsymbol{\delta}; \delta_{\max}) = \begin{cases} \sigma_c \delta - \frac{1}{2} \frac{\sigma_c}{\delta_c} \delta^2 & \text{if } \delta = \delta_{\max} \text{ and } \dot{\delta} \geq 0 \\ \frac{1}{2} \sigma_c \delta_{\max} + \frac{1}{2} \frac{\sigma_c}{\delta_{\max}} (1 - \frac{\delta_{\max}}{\delta_c}) \delta^2 & \text{otherwise.} \end{cases} \tag{3.8}$$

The above expressions correspond to the shaded areas in Figures 3.2a and 3.2b, respectively. One can verify that the cohesive energy ψ_{cohs} is a continuous function of $\boldsymbol{\delta}$ at $\delta = \delta_{\max}$. At this point, the interface undergoes loading if $\dot{\delta} \geq 0$ and unloading otherwise.

Prior to the initiation of damage, i.e., at the origin with $\delta = \delta_{\max} = 0$, the cohesive potential ψ_{cohs} is not a differentiable function of $\boldsymbol{\delta}$. In this case, ψ_{cohs} admits directional derivatives in the directions ($\delta_n \searrow 0$, $\|\boldsymbol{\delta}_s\| = 0$) and ($\delta_n = 0$, $\|\boldsymbol{\delta}_s\| \to 0$), which are σ_c and $\beta\sigma_c$, respectively. As explained in [30], these directional derivatives represent the material strength under monotonous normal and sliding solicitations, respectively. It follows that β in the definition (3.6) is the shear to normal material strength ratio. The three material constants δ_c, σ_c and G_c are related as $G_c = \sigma_c \delta_c / 2$ (that is, only two can be chosen

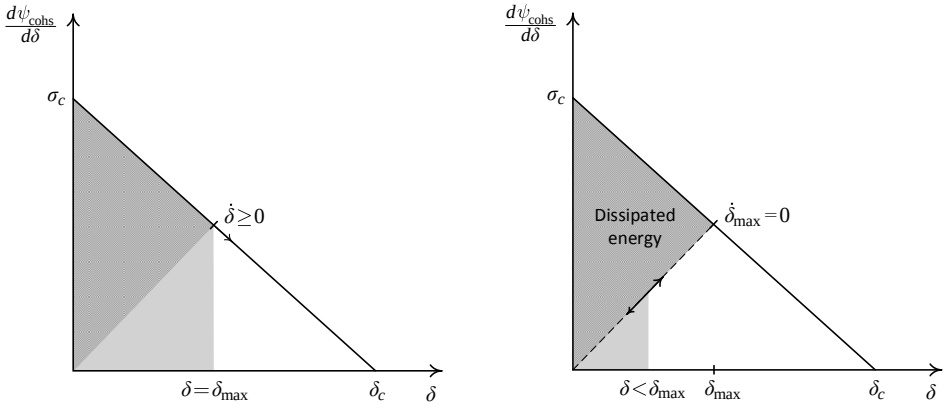

(a) (b)

Figure 3.2: Definition of the cohesive potential ψ_{cohs} for the case of a) loading and b) unloading or reloading. In each case, ψ_{cohs} equals to the total shaded area. The dissipated portion of the energy is shaded darker

independently). Before $\delta_{\max}$ reaches δ_c, the energy dissipated during the fracturing process is given by $\sigma_c \delta_{\max}/2$, see also Figure 3.2.

The indicator function (interpenetration penalty) $I_{\mathbb{R}^+}(\delta_n)$ is defined as

$$I_{\mathbb{R}^+}(\delta_n) = \begin{cases} \infty & \delta_n \in (-\infty, 0) \\ 0 & \delta_n \in [0, \infty). \end{cases} \tag{3.9}$$

With the above definition, negative displacement openings are not admissible as they would result in infinite energy, hence, not a minimum. Therefore, interpenetration of the crack faces is prohibited, i.e. $\delta_n \geq 0$. Again, we note that a gradient of the indicator function (3.9) is only properly defined for $\delta_n > 0$. Variation of the total interface potential $\phi = \psi_{\text{cohs}} + I_{\mathbb{R}^+}$ with δ_n and δ_s is shown in Figure 3.3, in which it is assumed that the interface undergoes loading and no unloading occurs.

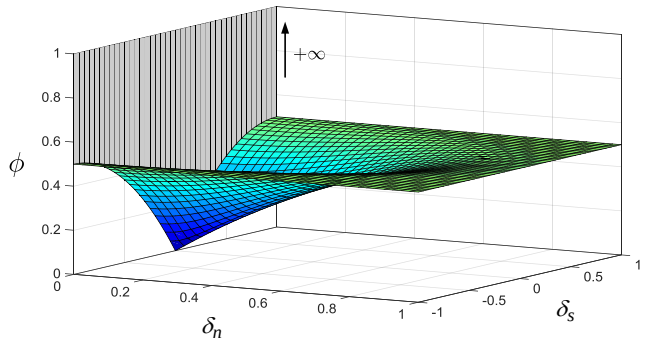

Figure 3.3: Variation of the total interface potential $\phi = \psi_{\text{cohs}} + I_{\mathbb{R}^+}$ as a function of δ_n and δ_s with $\sigma_c = 1.0$, $\delta_c = 1.0$ and $\beta = 1.0$. ϕ is not differentiable at $\boldsymbol{\delta} = \mathbf{0}$ and everywhere on the plane $\delta_n = 0$

3.3 Block coordinate descent algorithm for nondifferentiable energy minimization

As noted in [116, 73], passing to a weak form would not be a valid approach in the present setting because the interface potential π_{intf} in (3.2) is not globally differentiable. Instead, we apply finite element discretization directly to (3.5) to arrive at a sequence of finite-dimensional constrained nondifferentiable energy minimization problems defined at each time step in a time-discrete framework. In this section, we propose a solution method based on block coordinate descent algorithms for the nondifferentiable minimization problem obtained from a particular finite element discretization of (3.5).

3.3.1 Spatial discretization: the finite-dimensional problem

The infinite-dimensional spaces $\mathcal{U}$ and $\mathcal{D}$ in (3.10) are approximated by their finite-dimensional counterparts $\mathcal{U}_h$ and $\mathcal{D}_h$ containing finite element approximations constructed as described in Chapter 2.

Suppose that Ω is discretized by a finite element triangulation Ω_h. We take $\Gamma_{d,h}$ to be the set of all inter-element boundaries in Ω_h. This set is postulated *a priori* and assumed to not depend on the deformation (i.e., no re-meshing or realignment of the element edges occurs during the course of the simulation). Neighboring elements in Ω_h do not share nodal points and edges, allowing for a displacement jump $[\![\mathbf{u}_h]\!]$ on $\Gamma_{d,h}$, where $\mathbf{u}_h$ is the

element-wise continuous approximation of $\mathbf{u}$. Interface elements of dimension $n_{\text{dim}} - 1$ are placed at interelement boundaries providing a means for Gauss quadrature on $\Gamma_{d,h}$. The choice of $\Gamma_{d,h}$ is made for the convenience of the finite element implementation. However, the formulation can be applied to other discretization schemes such as XFEM [100, 99] that allow for the introduction of displacement jumps independent from the element edges. It is required that $\mathbf{u}_h = \widetilde{\mathbf{u}}_h$ on $\partial_u \Omega$.

In addition, a piece-wise constant approximation $\boldsymbol{\delta}_h$ of $\boldsymbol{\delta}$ is introduced. To this end, each Gauss point on $\Gamma_{d,h}$ is assigned an opening degree of freedom representing the constant value of the approximation in some vicinity of that Gauss point. The total number of Gauss points (opening nodal points) is denoted M and their coordinates are denoted $\boldsymbol{\xi}_I$, $I = 1, 2, ..., M$. We note that such approximation of $\boldsymbol{\delta}$, which is possible because no spatial derivatives of $\boldsymbol{\delta}$ exist in (3.10), makes the resulting finite-dimensional potential separable with respect to each nodal opening displacement unknown. This property is an essential ingredient of the proposed block-CD minimization algorithm presented in Section 3.3.3. In addition, the constraint (3.1) can be enforced on the Gauss point level, thus affording the possibility of sub-element crack resolution.

The constrained minimization problem (3.5) is now reduced to the following finite-dimensional problem that must be solved at each time step:

$$\min_{(\mathbf{U},\mathbf{d})} \left\{ \mathcal{L}^{\text{DG}}(\mathbf{u}_h, \boldsymbol{\delta}_h) = \pi(\mathbf{u}_h, \boldsymbol{\delta}_h) + \pi_g^{\text{DG}}(\mathbf{u}_h, \boldsymbol{\delta}_h) \right\}, \tag{3.10}$$

where $\mathbf{U}$ and $\mathbf{d}$ denote the global vector of nodal unknowns corresponding to $\mathbf{u}_h$ and $\boldsymbol{\delta}_h$, respectively, and π_g^{DG} is the discontinuous Galerkin constraint functional introduced to enforce the compatibility constraint $\boldsymbol{g} = \mathbf{0}$,

$$\pi_g^{\text{DG}}(\mathbf{u}_h, \boldsymbol{\delta}_h) = \int_{\Gamma_{d,h}} \boldsymbol{\lambda}_h^{\text{DG}} \cdot \boldsymbol{g}_h dS. \tag{3.11}$$

In the above, $\boldsymbol{\lambda}_h^{\text{DG}}$ is the DG numerical flux due to Nitsche [107] defined as a function of $\mathbf{u}_h$ and $\boldsymbol{\delta}_h$ as

$$\boldsymbol{\lambda}_h^{\text{DG}} = \langle \boldsymbol{\sigma}_h \rangle \, \mathbf{n}_d + \frac{1}{2} \eta \boldsymbol{g}_h, \tag{3.12}$$

where $\boldsymbol{\sigma}_h$ is the Cauchy stress tensor computed strongly from $\mathbf{u}_h$, η is a penalty number and $\langle * \rangle = \frac{1}{2}(*^+ + *^-)$. The penalty number is taken to be

$$\eta = \frac{\chi \mu}{h_s}, \tag{3.13}$$

in which μ is the shear modulus, h_s is the interface element size and χ is a parameter which must be taken sufficiently large to ensure stability of the DG method, typically $2 \leq \chi \leq 10$

[73, 129]. An augmented Lagrangian formulation is obtained if one replaces $\langle \boldsymbol{\sigma}_h \rangle \mathbf{n}_d$ with an independent Lagrange multiplier unknown as in [116, 91]. It was confirmed in Chapter 2 that convergence of the finite element method with mesh size and time step refinement is insensitive to the magnitude of the penalty in both the pre- and post-failure regimes.

The finite-dimensional minimization problem (3.10) is especially well suited for a block-CD minimization algorithm because of the separability of the objective $\mathcal{L}^{\mathrm{DG}}(\mathbf{u}_h, \boldsymbol{\delta}_h)$ with respect to each opening unknown $\mathbf{d}_I$, $I = 1, ...M$, and to the block of deformation unknowns $\mathbf{U}$.

3.3.2 Temporal discretization

Consider now a discretization of time domain with N time steps uniformly spaced with time intervals $\Delta t : t \in \{t_0 = 0, ..., t_i, t_{i+1}, t_N = T\}$. Suppose that a solution is known at t_i and a solution is sought at t_{i+1}. Let $\mathbf{U}_i$ and $\mathbf{d}_i$ denote the finite difference approximations to $\mathbf{U}(t_i)$ and $\mathbf{d}(t_i)$, respectively. Similarly, $\dot{\mathbf{U}}_i$ and $\ddot{\mathbf{U}}_i$ represent the finite difference approximations to $\dot{\mathbf{U}}(t_i)$ and $\ddot{\mathbf{U}}(t_i)$, respectively. We assume that the body is initially at rest and intact, that is $\mathbf{U}_0 = \mathbf{0}$, $\dot{\mathbf{U}}_0 = \mathbf{0}$ and $\mathbf{d}_0 = \mathbf{0}$. The evolution of the finite difference approximations to the time derivatives of the displacement unknowns in successive time steps t_i and t_{i+1} is described using the generalized Newmark scheme [104] as

$$\begin{aligned} \mathbf{U}_{i+1} &= \widehat{\mathbf{U}}_{i+1} + a_1 \frac{\Delta t^2}{2} (\ddot{\mathbf{U}}_{i+1} - \ddot{\mathbf{U}}_i) \quad \text{with } \widehat{\mathbf{U}}_{i+1} = \mathbf{U}_i + \Delta t \dot{\mathbf{U}}_i + \frac{\Delta t^2}{2} \ddot{\mathbf{U}}_i, \\ \dot{\mathbf{U}}_{i+1} &= \widehat{\dot{\mathbf{U}}}_{i+1} + a_2 \Delta t (\ddot{\mathbf{U}}_{i+1} - \ddot{\mathbf{U}}_i) \quad \text{with } \widehat{\dot{\mathbf{U}}}_{i+1} = \dot{\mathbf{U}}_i + \Delta t \ddot{\mathbf{U}}_i, \end{aligned} \tag{3.14}$$

where a_1 and a_2 are Newmark parameters. An implicit time-stepping scheme with unconditional stability corresponds to $a_1 \geq a_2 \geq 0.5$, whereas an explicit time-stepping scheme corresponds to $a_1 = 0$ and $a_2 = 0.5$.

Within the time-discrete framework, the loading conditions $\delta = \delta_{\max}$ and $\dot{\delta} \geq 0$ appearing in (3.7) and (3.8) are reduced to $\delta_{i+1} = \delta_{\max,i+1} \geq \kappa = \max\{\delta_0, ..., \delta_i\}$ and the cohesive potential is computed from the first of (3.8) with the current value of δ_{i+1}. Otherwise, i.e., in the case of unloading or reloading, the second of (3.8) is used to compute the cohesive potential with $\delta_{\max,i+1} = \delta_{\max,i}$. Accordingly, calculation of the cohesive potential in a time-step $i+1$ can be performed without use of $\delta_{\max,i+1}$ but, rather, by comparison of δ_{i+1} with $\delta_{\max,i}$ whose value is fixed at the beginning of a time-step. The time-discrete form of the cohesive potential may thus be written as

$$\psi_{\text{cohs}}(\boldsymbol{\delta}_{i+1};\delta_{\max}) = \begin{cases} \sigma_c\delta_{i+1} - \frac{1}{2}\frac{\sigma_c}{\delta_c}\delta_{i+1}^2 & \delta_{\max} \le \delta_{i+1} \le \delta_c \\ \frac{1}{2}\sigma_c\delta_{\max} + \frac{1}{2}\frac{\sigma_c}{\delta_{\max}}(1-\frac{\delta_{\max}}{\delta_c})\delta_{i+1}^2 & \delta_{i+1} < \delta_{\max} \le \delta_c \\ G_c & \delta_{\max} \ge \delta_c \text{ or } \delta_{i+1} \ge \delta_c, \end{cases} \tag{3.15}$$

where $\delta_{\max} = \delta_{\max,i}$. Here and subsequently, we shall omit the time step index i, for simplicity of presentation; the formulation that follows concerns solution of the minimization problem (3.10) at time step $i+1$.

3.3.3 The block coordinate descent algorithm

The block-separable structure of the finite-dimensional minimization problem (3.10) suggests the block strategy as follows. The minimization problem (3.10) is split into two sub-problems by solving for each $\mathbf{d}_I$, $I = 1, ..., M$ in one, and for $\mathbf{U}$ in the other in a decoupled manner, iteratively until convergence to a desired tolerance is achieved. In the following, we will present the formulation of the two-step scheme resulting from the above strategy for the update of the opening displacement unknowns and of the deformation unknowns in a typical iteration of the block-CD algorithm.

Considering the displacement unknowns $\mathbf{U}$, and therefore, π_{el}, π_{dyn} and W_{ext}, to be constant, minimization of the discrete potential (3.10) with respect to the opening unknowns $\mathbf{d}_I$ leads to the following set of "local" algorithmic minimization problems that serve to update the opening displacement unknowns $\mathbf{d}_I$:

$$\min_{\mathbf{d}_I} \left\{ \pi_\delta(\mathbf{d}_I;\mathbf{U}) = \psi_{\text{cohs}}(\mathbf{d}_I;\delta_{\max,I}) + I_{\mathbb{R}^+}(d_{n,I}) + \boldsymbol{\lambda}_{h,I}^{\text{DG}} \cdot \boldsymbol{g}_{h,I} \right\} \quad \text{for } I = 1:M. \tag{3.16}$$

In the above, $\boldsymbol{\lambda}_{h,I}^{\text{DG}}$ and $\boldsymbol{g}_{h,I}$ denote the corresponding variables evaluated at $\mathbf{x} = \boldsymbol{\xi}_I$; i.e., $\boldsymbol{g}_{h,I} = [\![\mathbf{u}_h(\boldsymbol{\xi}_I)]\!] - \mathbf{d}_I$ and $\boldsymbol{\lambda}_{h,I}^{\text{DG}} = \langle \boldsymbol{\sigma}_h(\boldsymbol{\xi}_I) \rangle \mathbf{n}_d + \frac{1}{2}\eta \boldsymbol{g}_{h,I}$. Each nondifferentiable energy minimization problem in (3.16) involves $\mathbf{d}_I$ as its unknown which is only of dimension $n_{\text{dim}} = 2, 3$. Solution of (3.16) will be discussed in detail in Section 3.4.

Next, for a known interface opening field $\mathbf{d}$ (thus treating the interface potential π_{intf} as constant), we minimize the discrete potential (3.10) with respect to $\mathbf{U}$ to obtain the following minimization problem used to update the block of deformation unknowns:

$$\min_{\mathbf{U}} \left\{ \pi_u(\mathbf{U};\mathbf{d}) = \pi_{\text{el}}(\mathbf{u}_h) + \pi_{\text{dyn}}(\mathbf{u}_h) - W_{\text{ext}}(\mathbf{u}_h) + \pi_g^{\text{DG}}(\mathbf{u}_h, \boldsymbol{\delta}_h) \right\}. \tag{3.17}$$

In contrast to the local minimization problems (3.16), the above minimization problem is quite straightforward as the algorithmic objective function π_u is quadratic and convex

in $\mathbf{U}$ and everywhere differentiable. The first order minimality condition for the global minimization problem (3.17) leads to the linear system of equations

$$\mathbf{R}_u(\mathbf{U};\mathbf{d}) \equiv \mathbf{M}\ddot{\mathbf{U}} + \mathbf{K}_{uu}\mathbf{U} - \mathbf{K}_{ud}\mathbf{d} - \mathbf{F}_{\text{ext}} = \mathbf{0}, \tag{3.18}$$

obtained by taking the gradient of the discrete objective function in (3.17) with respect to $\mathbf{U}$, in which the mass matrix $\mathbf{M}$, stiffness matrices $\mathbf{K}_{uu}$ and $\mathbf{K}_{ud}$ and the external force vector $\mathbf{F}_{\text{ext}}$ are given by

$$\begin{aligned}
\mathbf{M} &= \int_{\Omega_h \setminus \Gamma_{d,h}} (\mathbf{N}^u)^T \rho \mathbf{N}^u \, dV, \\
\mathbf{K}_{uu} &= \int_{\Omega_h \setminus \Gamma_{d,h}} \mathbf{B}^T \mathbf{D} \mathbf{B} \, dV + \int_{\Gamma_{d,h}} (\mathbf{N}^{[\![u]\!]})^T \eta \mathbf{N}^{[\![u]\!]} \, dS \\
&+ \int_{\Gamma_{d,h}} (\mathbf{N}^{[\![u]\!]})^T \bar{\mathbf{n}}_d \mathbf{D} \mathbf{B}^{\langle\sigma\rangle} \, dS + \int_{\Gamma_{d,h}} (\mathbf{B}^{\langle\sigma\rangle})^T \mathbf{D} \bar{\mathbf{n}}_d^T \mathbf{N}^{[\![u]\!]} \, dS, \\
\mathbf{K}_{ud} &= \int_{\Gamma_{d,h}} (\mathbf{N}^{[\![u]\!]})^T \eta \mathbf{N}^{\delta} \, dS + \int_{\Gamma_{d,h}} (\mathbf{B}^{\langle\sigma\rangle})^T \mathbf{D} \bar{\mathbf{n}}_d^T \mathbf{N}^{\delta} \, dS, \\
\mathbf{F}_{\text{ext}} &= \int_{\partial_t \Omega} (\mathbf{N}^u)^T \widetilde{\mathbf{t}} \, dS.
\end{aligned} \tag{3.19}$$

In the above, $\mathbf{N}^u(\mathbf{x})$ and $\mathbf{N}^{\delta}(\mathbf{x})$ are the matrices of finite element shape functions approximating $\mathbf{u}_h$ and $\boldsymbol{\delta}_h$, respectively; $\mathbf{B}$ is the strain-displacement matrix containing spatial derivatives of the displacement shape functions; $\mathbf{N}^{[\![u]\!]}$ and $\mathbf{B}^{\langle\sigma\rangle}$ contain traces of $\mathbf{N}^u$ and $\mathbf{B}$ on the interface $\Gamma_{d,h}$ and are defined to approximate the jump $[\![\mathbf{u}_u]\!]$ and average Cauchy stress $\langle\boldsymbol{\sigma}_h\rangle$ on $\Gamma_{d,h}$, respectively. $\mathbf{D}$ (by a slight abuse of notation) is the elasticity matrix and $\bar{\mathbf{n}}_d$ contains the components of the normal $\mathbf{n}_d$ and is defined for the transformation from tensorial to matrix formulation (see also Equation A.7). Equation (3.18) is essentially a standard finite element method with the added feature that interface openings $\mathbf{d}_I$ are imposed at the interelement boundaries of the finite element mesh.

The block-CD algorithm resulting from the above minimization strategy is outlined in Algorithm 3.1. As $\mathbf{U}$ and $\ddot{\mathbf{U}}$ are linked through the Newmark's time-marching scheme (3.14), one can solve (3.18) for either $\mathbf{U}$ or $\ddot{\mathbf{U}}$. In Algorithm 3.1, we solve for $\ddot{\mathbf{U}}$ in an incremental fashion whereby an increment $\Delta\ddot{\mathbf{U}}$, obtained by evaluating the residual $\mathbf{R}_u(\mathbf{U};\mathbf{d})$ at the current estimate solution, is used to update $\ddot{\mathbf{U}}$ in each iteration. The corresponding Jacobean matrix $\mathbf{J} = \partial\mathbf{R}_u/\partial\ddot{\mathbf{U}}$ is

$$\mathbf{J} = a_1 \frac{\Delta t^2}{2} \mathbf{K}_{uu} + \mathbf{M}. \tag{3.20}$$

Algorithm 3.1 Block-CD nondifferentiable energy minimization algorithm; the sub-script $i+1$ is omitted for simplicity of presentation

Given $\mathbf{U}_i$, $\dot{\mathbf{U}}_i$, $\ddot{\mathbf{U}}_i$ and $\mathbf{d}_i$

Update $\delta_{\max} = \max\{\delta_0, ..., \delta_i\}$ at all interface points $I = 1 : M$

Initiate block-CD iterations. Set *predictors*,

$\mathbf{U}^0 = \mathbf{U}_i + \Delta t \dot{\mathbf{U}}_i + \frac{\Delta t^2}{2} \ddot{\mathbf{U}}_i$
$\dot{\mathbf{U}}^0 = \dot{\mathbf{U}}_i + \Delta t \ddot{\mathbf{U}}_i$,
$\ddot{\mathbf{U}}^0 = \ddot{\mathbf{U}}_i$ and $\mathbf{d}^0 = \mathbf{d}_i$.

Loop on block-CD iteration $j = 0, 1, ...$

Update of opening field (Algorithm 3.2)

$\mathbf{d}_I^{j+1} = \underset{\mathbf{d}_I}{\operatorname{argmin}}\ \pi_\delta(\mathbf{d}_I; \mathbf{U}^j)$ for all $I = 1 : M$

Update $\mathbf{d}$: $\mathbf{d}^j \to \mathbf{d}^{j+1}$

Update of deformation field

$\Delta \ddot{\mathbf{U}}^{j+1} = -\mathbf{J}^{-1} \mathbf{R}_u(\mathbf{U}^j; \mathbf{d}^{j+1})$
$\ddot{\mathbf{U}}^{j+1} = \ddot{\mathbf{U}}^j + \Delta \ddot{\mathbf{U}}^{j+1}$

$\mathbf{U}^{j+1} = \mathbf{U}^j + a_1 \frac{\Delta t^2}{2} \Delta \ddot{\mathbf{U}}^{j+1}$
$\dot{\mathbf{U}}^{j+1} = \dot{\mathbf{U}}^j + a_2 \Delta t \Delta \ddot{\mathbf{U}}^{j+1}$

if *explicit*, **go to** next time step

if $\frac{\|\mathbf{R}_u(\mathbf{U}^{j+1}, \mathbf{d}^{j+1})\|}{\|\mathbf{R}_u(\mathbf{U}^0, \mathbf{d}^0)\|} \leq \text{tol}_R$ and $\frac{\|\mathbf{d}^{j+1} - \mathbf{d}^j\|}{\|\mathbf{d}^0\|} \leq \text{tol}_d$, **go to** next time step

End Loop on block-CD iterations

In an explicit time-stepping scheme ($a_1 = 0$) the Jacobian matrix simplifies to $\mathbf{J} = \mathbf{M}$. In that case, one can replace $\mathbf{M}$ with a lumped mass matrix as is typical in explicit time-stepping calculations. In linear elasticity, the Jacobian $\mathbf{J}$ remains constant throughout the calculations and needs to be factorized only once at the start of the simulation.

In implicit calculations, convergence of the block-CD iterations is determined based on the residual of the optimality condition (3.18) as well as on the difference between the opening unknowns $\mathbf{d}$ in successive block-CD iterations.

3.4 Update of the opening field

3.4.1 Characterization of a minimum at nondifferentiable points

For the solution of the nondifferentiable problem (3.16) we make use of the generalized differential calculus of nonsmooth optimization [32, 33], a brief description of which is presented in Appendix B for completeness of presentation.

Let us suppose that $\pi_\delta(\mathbf{d}_I;\mathbf{U})$ possesses a minimizer, i.e., it is a locally convex function of $\mathbf{d}_I$ in the domain of admissible solutions $\mathbf{d}_I \in \mathbb{R}^{n_{\text{dim}}}$ s.t. $d_{n,I} \geq 0$. We will get back to convexity of $\pi_\delta(\mathbf{d}_I;\mathbf{U})$ in general in Section 3.4.2. Using definition (B.3), the minimality condition of π_δ, equation (3.16), can, with use of (3.1) and (3.10), be expressed at each interface point I as: $\mathbf{d}_I^\star$ is a minimizer of π_δ if and only if

$$\mathbf{0} \in \partial\psi_{\text{cohs}}(\mathbf{d}_I^\star;\delta_{\max,I}) + \partial I_{\mathbb{R}}^+(d_{n,I}^\star) + \{\eta\mathbf{d}_I^\star - \boldsymbol{\tau}_I\}\,, \tag{3.21}$$

in which

$$\boldsymbol{\tau}_I = \langle\boldsymbol{\sigma}_I\rangle\cdot\mathbf{n}_d + \eta[\![\mathbf{u}_I]\!] \tag{3.22}$$

is a traction computed from the known deformation field at interface point I (here and in the remaining of this section, the subscript h is dropped for simplicity of presentation).

The generalized gradient of ψ_{cohs} is defined at the origin as

$$\partial\psi_{\text{cohs}}(\mathbf{0};0) = \left\{\mathbf{t}_{\text{cohs}}^0 \in \mathbb{R}^{n_{\text{dim}}} \mid t_{\text{cohs},n}^0 \geq 0 \;\text{ and }\; \left\|\mathbf{t}_{\text{cohs}}^0\right\|_\beta \leq \sigma_c\right\}, \tag{3.23}$$

where $\|\mathbf{t}_{\text{cohs}}^0\|_\beta$ is an effective norm of $\mathbf{t}_{\text{cohs}}^0$ defined as,

$$\left\|\mathbf{t}_{\text{cohs}}^0\right\|_\beta = \sqrt{(t_{\text{cohs},n}^0)^2 + \|\mathbf{t}_{\text{cohs},s}^0/\beta\|^2}. \tag{3.24}$$

We show in Figure 3.4, a graphical interpretation of $\partial\psi_{\text{cohs}}(\mathbf{0};0)$ in the plane $\delta_s = 0$ and in the plane $\delta_n = 0$. In the plane $\delta_s = 0$ (Figure 3.4a), the set of slopes $0 \leq t_{\text{cohs},n}^0 \leq \sigma_c$ of lines passing through the origin constitutes $\partial\psi_{\text{cohs}}(\mathbf{0};0)$. In the plane $\delta_n = 0$ (Figure 3.4b), the slopes that constitute $\partial\psi_{\text{cohs}}(\mathbf{0};0)$ are $-\sigma_c \leq t_{\text{cohs},s}^0/\beta \leq \sigma_c$. In the general case, the generalized gradient $\partial\psi_{\text{cohs}}(\mathbf{0};0)$ may be interpreted as the set of "tensile" cohesive tractions $\mathbf{t}_{\text{cohs}}^0 \in \mathbb{R}^{n_{\text{dim}}}$ whose effective norm is below the material strength σ_c. Anywhere else than the origin, the generalized gradient of ψ_{cohs} coincides with its gradient, i.e., $\partial\psi_{\text{cohs}}(\boldsymbol{\delta};\delta_{\max}) = \{\nabla\psi_{\text{cohs}}(\boldsymbol{\delta};\delta_{\max})\}$, where

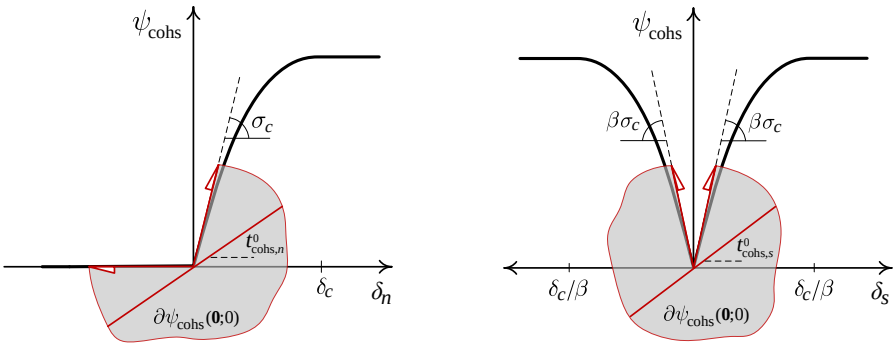

Figure 3.4: Graphical interpretation of $\partial\psi_{\text{cohs}}$ at the origin; a) in the plane $\delta_s = 0$ and b) in the plane $\delta_n = 0$

$$\nabla\psi_{\text{cohs}}(\boldsymbol{\delta};\delta_{\max}) \equiv \mathbf{t}_{\text{cohs}}(\boldsymbol{\delta};\delta_{\max}) = \frac{t_{\text{cohs}}(\delta;\delta_{\max})}{\delta}\left(\delta_n^+\mathbf{n}_d + \beta^2\boldsymbol{\delta}_s\right), \tag{3.25}$$

in which $t_{\text{cohs}}(\delta;\delta_{\max}) = d\psi_{\text{cohs}}/d\delta$ is a scalar cohesive traction.

Next, the generalized gradient of $I_{\mathbb{R}^+}$ at $\delta_n = 0$ is expressed as

$$\partial I_{\mathbb{R}^+}(0) = \left\{t_{\text{cont}}\mathbf{n}_d \in \mathbb{R}^{n_{\text{dim}}} \mid t_{\text{cont}} \leq 0\right\}. \tag{3.26}$$

A schematic of the generalized gradient $\partial I_{\mathbb{R}^+}(0)$ is shown in Figure 3.5. Each member of $\partial I_{\mathbb{R}^+}(0)$ corresponds to the negative slope $t_{\text{cont}} \leq 0$ of a line passing through the origin. In fact, the above generalized gradient implies that interpenetration is precluded through a normal contact stress t_{cont}, whose value is, however, not uniquely defined. Note that the normal $\mathbf{n}_d$ appears in (3.26) because the generalized gradient is taken with respect to $\boldsymbol{\delta}$. For $\delta_n > 0$, the generalized gradient of $I_{\mathbb{R}^+}$ is $\{\mathbf{0}\}$ whereas it is the empty set $\emptyset$ for $\delta_n < 0$ [32, 33].

In view of the above, two cases require special attention when obtaining a minimum solution through (3.21): 1) at the origin, where both ψ_{cohs} and $I_{\mathbb{R}^+}$ are nondifferentiable, 2) at points away from the origin, at which $d_{n,I} = 0$, so that only $I_{\mathbb{R}^+}$ is nondifferentiable. Considering the minimality condition (3.21) at these points, the following propositions are deduced:

Proposition 1. Suppose that $\delta_{\max,I} = 0$. A minimizer of π_δ occurs at $\mathbf{d}_I^\star = \mathbf{0}$ (i.e., at the origin) if and only if $\tau_I \leq \sigma_c$, where τ_I is an effective norm of the tensile part of $\boldsymbol{\tau}_I$

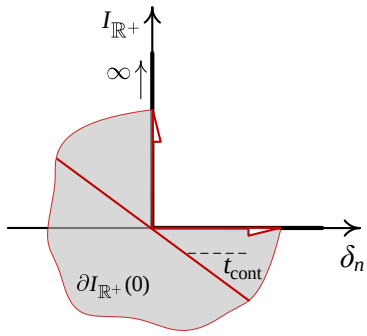

Figure 3.5: Graphical interpretation of $\partial I_{\mathbb{R}^+}$ at $\delta_n = 0$

defined as

$$\tau_I \equiv \|\boldsymbol{\tau}_I^+\|_\beta = \sqrt{(\tau_{n,I}^+)^2 + \|\boldsymbol{\tau}_{s,I}/\beta\|^2}. \tag{3.27}$$

Proof. We will show this by verifying that $p_I \leq \sigma_c$ guarantees that the minimality condition (3.21) holds at $\mathbf{d}_I = \mathbf{0}$,

$$\mathbf{0} \in \partial\psi_{\text{cohs}}(\mathbf{0}; 0) + \partial I_{\mathbb{R}^+}(0) + \{-\boldsymbol{\tau}_I\}\,.$$

The summation $\partial\psi_{\text{cohs}}(\mathbf{0}; 0) + \partial I_{\mathbb{R}^+}(0)$ on the RHS of the above expression is denoted $\partial\phi(\mathbf{0})$ and can be expressed as

$$\partial\phi(\mathbf{0}) = \left\{\mathbf{t}_{\text{intf}} \in \mathbb{R}^{n_{\text{dim}}} \mid \left\|\mathbf{t}_{\text{intf}}^+\right\|_\beta \leq \sigma_c\right\}.$$

The minimality condition now reads

$$\mathbf{0} \in \partial\phi(\mathbf{0}) + \{-\boldsymbol{\tau}_I\} \;\Rightarrow\; \boldsymbol{\tau}_I \in \partial\phi(\mathbf{0}),$$

which is ensured with $\tau_I \leq \sigma_c$. At the minimizer $\mathbf{d}_I^\star = \mathbf{0}$, $\mathbf{t}_{\text{intf}}^\star = \boldsymbol{\tau}_I$.

Proposition 2. Suppose that the minimizer $\mathbf{d}_I^\star$ occurs not at the origin. Then, $d_{n,I}^\star = 0$ if and only if $\tau_{n,I} \leq 0$.

Proof. The minimality condition of π_δ equation (3.21) is expressed at $(d_{n,I} = 0, \mathbf{d}_{s,I})$ as

$$\mathbf{0} \in \partial I_{\mathbb{R}^+}(0) + \{\mathbf{t}_{\text{cohs}}(\mathbf{d}_{s,I}; \delta_{\max,I})\} + \{\eta\mathbf{d}_{s,I} - \boldsymbol{\tau}_I\}\,.$$

In the above, the cohesive traction $\mathbf{t}_{\text{cohs}}$, given by (3.25), is a function of $\mathbf{d}_{s,I}$ only since $d_{n,I} = 0$. Noting that the normal components of $\eta\mathbf{d}_{s,I}$ and $\mathbf{t}_{\text{cohs}}(\mathbf{d}_{s,I}; \delta_{\max,I})$ are both zero,

one obtains $\tau_{n,I}\mathbf{n}_d \in \partial I_{\mathbb{R}^+}(0)$ from the above minimality condition, which is ensured when $\tau_{n,I} \leq 0$. In that case, $t^\star_{\text{cont}} = p_{n,I}$ at the minimizer $d^\star_{n,I} = 0$. In the sliding direction, the minimizer satisfies $\mathbf{t}_{\text{cohs}}(\mathbf{d}^\star_{s,I}; \delta_{\max,I}) + \eta\mathbf{d}^\star_{s,I} = \boldsymbol{\tau}_{s,I}$.

The first proposition serves as an initiation criterion, whereas the second proposition serves to identify the case an interface undergoes contact (compression) after a crack has formed. In fact, the above propositions readily determine if a minimizer of π_δ occurs at a nondifferentiable point. If not, solution is sought in a domain where π_δ is differentiable using a smooth minimization algorithm such as the trust region method. Accordingly, we propose Algorithm 3.2 for the solution of the minimization problem (3.16).

Algorithm 3.2 Update of opening at node I

Compute $\boldsymbol{\tau}_I = \langle \boldsymbol{\sigma}_I \rangle \cdot \mathbf{n}_d + \eta[\![\mathbf{u}_I]\!]$, equation (3.22)
Compute $\tau_I = \sqrt{(\tau^+_{n,I})^2 + \|\boldsymbol{\tau}_{s,I}/\beta\|^2}$, equation (3.27)
if $\tau_I \leq \sigma_c$, and $\delta_{\max,I} = 0$, **then**
    pre-activation state with $\mathbf{d}^\star_I = \mathbf{0}$ (Proposition 1)
else
    if $\tau_{n,I} \leq 0$, set $d^\star_{n,I} = 0$ (Proposition 2) and solve (3.16) for $\mathbf{d}_{s,I}$ only,
    else, declare $d^\star_{n,I} > 0$ and solve (3.16) for $\mathbf{d}_I$
end

3.4.2 Convexity and existence of a minimum

As already pointed out, the underlying assumption in the above presentation is that π_δ attains a minimum at $\mathbf{d}^\star_I$, which would be the case only if π_δ were a convex function of $\mathbf{d}_I$. However, the cohesive potential ψ_{cohs} as defined in (3.15) is a strictly concave function of the opening in its loading branch. The convexity of π_δ, therefore, depends on the magnitude of the penalty parameter η as the term $\boldsymbol{\lambda}^{\text{DG}}_{h,I} \cdot \boldsymbol{g}_{h,I}$ in (3.16) introduces a quadratic term $\frac{1}{2}\eta\mathbf{d}_I \cdot \mathbf{d}_I$ in π_δ. To further investigate this, let us consider the simple 1D case of only normal (axial) deformation (i.e., $\mathbf{d}_{s,I} = \mathbf{0}$) and assume that a crack has not yet formed, i.e., $\delta_{\max,I} = 0$. The generalized gradient of π_δ may be expressed in the domain of admissible solutions (i.e., $d_{n,I} \geq 0$) as

$$\partial\pi_\delta(d_{n,I}) = \begin{cases} \{t_{\text{intf},n} - \tau_{n,I} \mid t_{\text{intf},n} \leq \sigma_c\} & d_{n,I} = 0 \\ \{\sigma_c - \tau_{n,I} + (\eta - H_c)d_{n,I}\} & d_{n,I} \in (0, \delta_c) \\ \{\eta d_{n,I} - \tau_{n,I}\} & d_{n,I} \in [\delta_c, \infty), \end{cases} \tag{3.28}$$

where $H_c = \sigma_c/\delta_c$. The above expression implies that π_δ is convex in $(0, \delta_c)$ if $\eta > H_c$ (this would change to $\eta > \beta^2 H_c$ if the sliding direction was considered) and in $[\delta_c, \infty)$ if $\eta > 0$. While the latter condition is automatically satisfied thanks to the definition (3.13), the former is not readily guaranteed. Let us suppose now that $\tau_{n,I} \leq \sigma_c$ (including negative values). In this case, it is easily seen that $d^\star_{n,I} = 0$ is a global minimizer of π_δ only if $\eta > H_c$ (one can verify this by noting that the sub-gradient cannot be 0 in $(0, \delta_c)$ or in $[\delta_c, \infty)$ in this case). If $\eta > H_c$ does not hold, then convexity is lost in $(0, \delta_c)$ and $d^\star_{n,I} = 0$ would only be a local minimizer of π_δ (note that π_δ is zero at $d_{n,I} = 0$, infinite for negative values of $d_{n,I}$ and greater than zero in some positive neighbourhood of $d_{n,I} = 0$, hence a local minimum). In that case, the other candidate for a local minimizer of π_δ lives in $[\delta_c, \infty)$ where π_δ is convex. This minimizer would be an undesirable, physically questionable solution as it implies premature crack nucleation. In addition, it is generally not clear which of the two cases corresponds to a global minimizer of π_δ.

A similar argument could be made for the case of $\tau_{n,I} > \sigma_c$. In that case, the minimizer can no longer occur at $d_{n,I} = 0$ as $0 \notin \{t_{\text{intf},n} - \tau_{n,I} \mid t_{\text{intf},n} \leq \sigma_c\}$ and must be sought within $(0, \infty)$, i.e., a crack nucleates. Again, a global minimum exists only if $\eta > H_c$. Otherwise, convexity is lost in $(0, \delta_c)$ and a local minimum is obtained in $[\delta_c, \infty)$. This implies an immediate transition to complete loss of cohesion and would lead to dissipation of incorrect amount of fracture energies from a physical point of view. In the general case, the condition for convexity of π_δ may be expressed as

$$\eta > \max(H_c, \beta^2 H_c). \tag{3.29}$$

Remark 1. The characteristic lengths of the cohesive process zone, l_c, can be expressed as [12]

$$l_c = 4a\nu' \frac{\mu}{H_c}, \tag{3.30}$$

where μ is the shear modulus as mentioned previously, $\nu' = \frac{1}{1-\nu}$ for plane strain, $\nu' = 1+\nu$ for plane stress, ν is the Poissons ratio and $a = \pi/8$ according to Barenblatts cohesive crack theory [11]. With $0 \leq \nu \leq 0.5$, one has $\frac{\pi}{2} \leq 4a\nu' \leq \pi$. It has been observed that for the crack to capture the correct amount of dissipated fracture energy, the characteristic length l_c must be adequately resolved by the discretization, i.e., $h_s < l_c$, see, e.g., [25]. We show that the above requirement is closely related to the convexity condition (3.29). By recourse to the definition of η equation (3.13), and assuming $\beta = 1$, equation (3.29) may be recast in form of $h_s \leq l_b$, where

$$l_b = \chi \frac{\mu}{H_c}. \tag{3.31}$$

By taking $2 \leq \chi \leq 10$ for stability of the DG method, the condition defined by l_b slightly relaxes the one defined by l_c. In fact, l_c would be just about the lower bound of l_b. In consequence, it may be argued that convexity is ensured with $2 \leq \chi \leq 10$ when $h_s < l_c$. Under such conditions, the role of the penalty parameter remains only a stabilizer of the DG method. The present discussion would still be valid if an augmented Lagrangian approach [116, 91] was used rather than a DG formulation, provided that the penalty is defined through (3.13).

3.4.3 Trust region algorithm for smooth optimization

The smooth minimization problems encountered in the "Else" block of Algorithm 3.2 are solved using the trust region minimization algorithm. The trust region iteration is initialized with an estimate $\mathbf{d}_I^0$, which is taken to be the converged solution of the previous block-CD iteration, and with a trust region radius Δ_0 taken to be the real-space size of the interface element under consideration. This value is reset at the beginning of each block-CD iteration. The trust region algorithm seeks the solution to the following constrained minimization sub-problem in each of its iterations:

$$\min_{d\mathbf{d}_I} m_k(d\mathbf{d}_I) \;\; \text{s.t.} \;\; \|d\mathbf{d}_I\| \leq \Delta_k, \tag{3.32}$$

in which k is the iteration index, and $m_k(d\mathbf{d}_I) = \pi_\delta(\mathbf{d}_I^k) + \nabla\pi_\delta(\mathbf{d}_I^k) \cdot d\mathbf{d}_I + \frac{1}{2} d\mathbf{d}_I \cdot \nabla^2(\mathbf{d}_I^k) \cdot d\mathbf{d}_I$, obtained from the first three terms of the Taylor series expansion of π_δ around the current solution estimate $\mathbf{d}_I^k$. We recall that the solution is being sought in a domain where π_δ is differentiable and the gradient $\nabla\pi_\delta$ and Hessian $\nabla^2\pi_\delta$ are properly defined. In order to solve the trust region sub-problem (3.32), the nearly exact method of More and Sorensen [108] has been employed, which is particularly capable of handling indefinite Hessians (i.e., nonconvex potentials). For further details regarding the trust region algorithm, the reader is referred to [108].

The trust region algorithm always converges to a solution. It is known that the second order necessary conditions for minimality (i.e., convexity) will be satisfied at the termination point of the trust region iteration. In consequence, the condition presented in Section 3.4.2 is not a requirement for convergence of the trust region iterations. In our computational experiments, the trust region algorithm took at most 10 iterations to converge when proper initial estimates were used, irrespective of the magnitude of the penalty η.

Remark 2. With $\beta = 1$, it is possible to obtain a closed form expression for the solution of the smooth minimization problems. In that case, the minimizer $\mathbf{d}_I^\star$ may be

expressed in a compact form as

$$\mathbf{d}_I^\star = \frac{\boldsymbol{\tau}_I^+}{p_I} d_I^\star, \tag{3.33}$$

where

$$d_I^\star = \begin{cases} \frac{\tau_I}{\eta + \sigma_{\max,I}/\delta_{\max,I}} & \tau_I \leq \tau_{\max,I} \ \text{ and } \delta_{\max,I} \leq \delta_c \\ \frac{\tau_I - \sigma_c}{\eta - H_c} & \tau_{\max,I} < \tau_I \leq \eta\delta_c \ \text{ and } \delta_{\max,I} \leq \delta_c \\ \frac{\tau_I}{\eta} & \tau_I \geq \eta\delta_c \ \text{ or } \delta_{\max,I} \geq \delta_c, \end{cases} \tag{3.34}$$

and $\tau_{\max,I} = \sigma_{\max,I} + \eta\delta_{\max,I}$. In the above, it is assumed that the convexity condition equation (3.29) is fulfilled. In cases that $\beta \neq 1$, the above solution may be used as an initial estimate for initiation of the trust region iterations when the crack first nucleates.

Remark 3. We note that the method presented in this section automatically recovers the case of linear elastic fracture mechanics (i.e., no cohesion after a crack forms) in the limit when $\delta_c \to 0$. In that case, Propositions 1 and 2 remain valid as nucleation and contact criteria but a minimizer of π_δ would always occur in $(\delta_c \simeq 0, \infty)$ for any finite $\eta > 0$ in the post-failure stage. Accordingly, the post-failure crack opening displacement may be expressed for a linear elastic fracture mechanics model simply as $\mathbf{d}_I^\star = \boldsymbol{\tau}_I^+/\eta$.

3.5 Numerical simulations

In this section, we simulate a variety of problems involving fragmentation and branching using the proposed block-CD algorithm. Unless otherwise stated, the coefficient χ in the definition of the penalty number (3.13) was taken as 10 and the characteristic length of the cohesive crack model, l_c, was adequately resolved by the finite element discretization so that $h_s \ll l_c$. In consequence, convexity of the interface potential and robustness of the numerical results were ensured, see Section 3.4.2.

3.5.1 Fragmentation of a thick cylinder

We consider the fragmentation of a thick cylinder subjected to impulsive internal pressure. The problem set-up and material properties are shown in Figure 3.6a. The internal pressure decays exponentially with time as $p(t) = p_0 e^{-t/t_0}$, where $p_0 = 400$ MPa and $t_0 = 100$ μs. The problem has been previously studied by Song and Belytschko [153] using an XFEM algorithm and by Hirmand and Papoulia [73] using the present energy approach but with a continuation-trust region minimization strategy, as well as by Geelen et al.

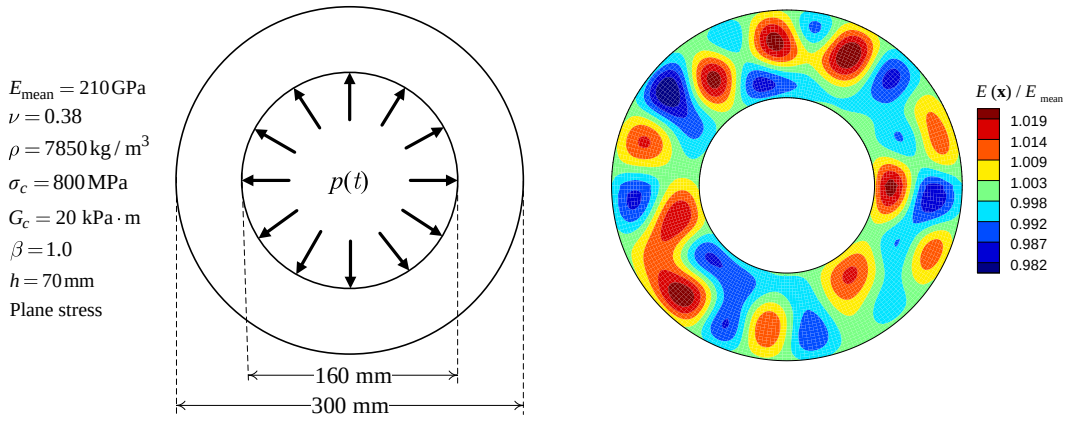

Figure 3.6: Fragmentation of a thick cylinder; a) problem definition and relevant properties and b) distribution of the random modulus used in the computations

[62] using a phase-field regularized cohesive algorithm. Zhou and Molinari [182] produced a detailed study of mesh dependence of the results. In order to break the symmetry of the model and counter mesh dependence, the material was considered nonhomogeneous by introducing randomness to the elastic modulus $E(\mathbf{x})$. The random field was discretized on a background material mesh by making use of the Karhunen- Loève (KL) expansion [148] with a squared exponential covariance function. Figure 3.6b shows one sample of the random fields used in our computations, which was generated using a length scale of 5 mm and standard deviation of 0.05. In the following, we show results using the implicit scheme. Our experiments with the explicit scheme, not reported here, led to similar conclusions.

We considered three meshes with different levels of refinement, containing 20042, 30258 and 40654 6-noded triangular elements with average element size 0.25 mm, 0.19 mm and 0.15 mm, respectively. The length of the fracture process zone obtained from (3.30) is $l_c = 2.8$ mm, which is discretized with adequate resolution by all meshes. In all cases, a three-point Gauss quadrature scheme was used for numerical integration along interface elements (i.e., three nodal opening unknowns per interface). We performed implicit time-stepping with $\Delta t = 2\Delta t_{\text{cr}}$, where Δ_{cr} is the critical time step of the explicit scheme, for a total simulation time of $T = 85$ μs. This choice of time step size was made based on accuracy considerations and in order to facilitate convergence of the block-CD algorithm within a reasonable number of iterations (this topic will be discussed further in what follows). The convergence tolerances (see Algorithm 3.1) were set to $\text{tol}_R = 5 \times 10^{-3}$ and $\text{tol}_d = 10^{-7}$.

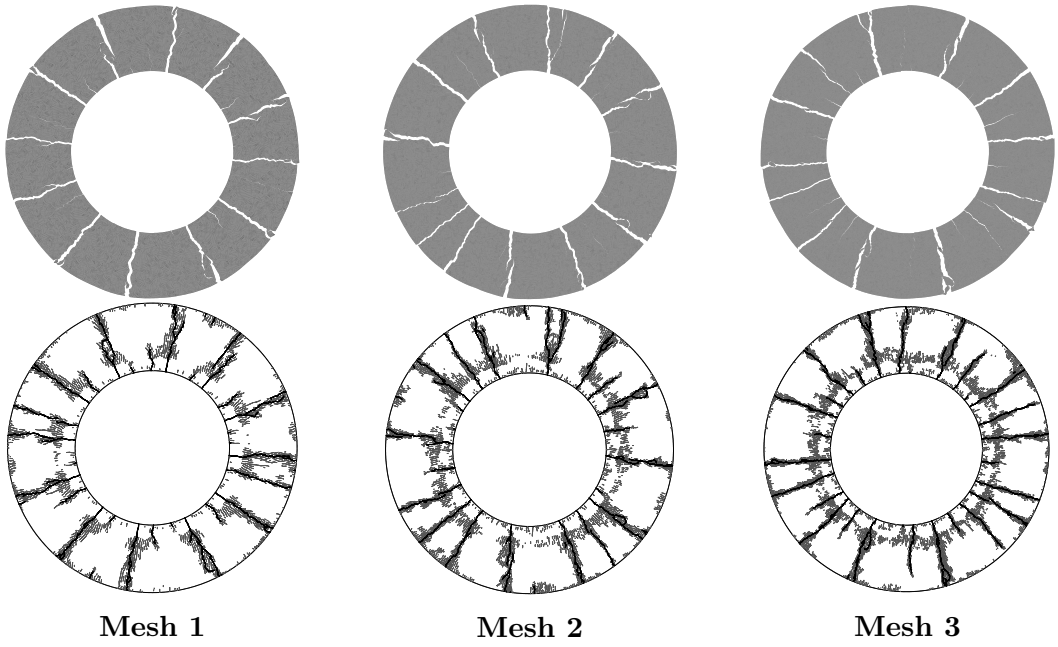

Figure 3.7: Final deformed meshes (magnified 10 times) and activated interfaces obtained for fragmentation of a thick cylinder at $T = 85$ μs

The final deformed configurations and activation patterns obtained by the three meshes are shown in Figure 3.7. In all simulations, fragmentation initiates at around 37 μs at the inner surface of the cylinder and continues until the cracks reach the outer surface at about 78 μs. Results obtained with different meshes are generally in good agreement and, even though some mesh dependence is observed in terms of the location, shape and size of the fragments, different meshes appear to produce a consistent number of $13 - 15$ fragments (the number also depends on the method of counting). More importantly, the time histories of the dissipated fracture energy and the elastic strain energy, shown in Figure 3.8, exhibit convergence with mesh refinement. Our numerical experiments with other samples of the random field and with meshes of different element orientations led to similar observations.

In all simulations, convergence of the block-CD iterations was achieved in a maximum of 8 iterations after initiation of cracks; the algorithm converged to machine precision in only one iteration prior to activation of the interfaces. An alternative to setting predetermined tolerances as convergence criteria of the block-CD algorithm in implicit computations would be to use $\Delta t \leq \Delta t_{\text{cr}}$ and allow for only one passing of iterations (i.e., $j = 1$ in Algorithm 3.1). A similar approach has been common particularly in the so-called staggered solutions

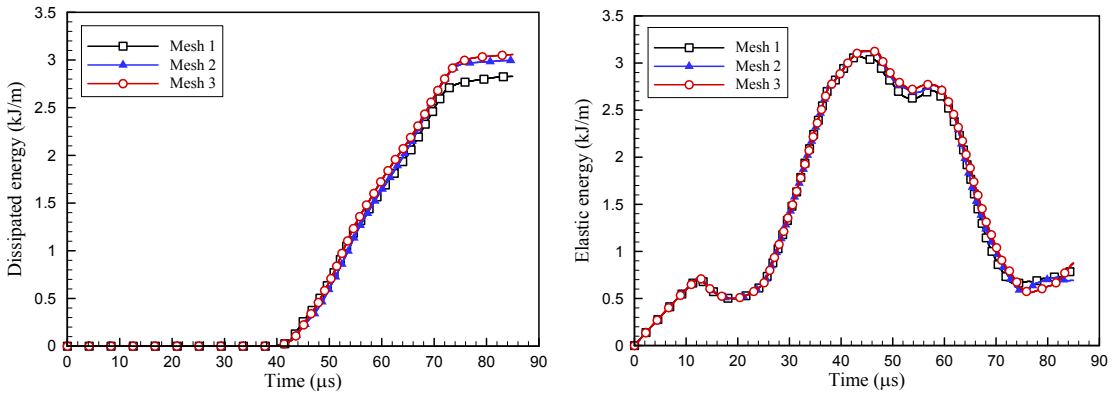

(a) (b)

Figure 3.8: Time histories of the a) dissipated fracture energy and b) elastic strain energy obtained for fragmentation of a thick cylinder

of phase-filed models of fracture [18, 90, 97]. The final deformed geometries and the crack activation patterns obtained using such scheme with $\Delta t = 0.95\Delta t_{\text{cr}}$ are shown in Figure 3.9. Results obtained are seemingly identical with the converged results shown previously in Figure 3.7. A similar statement could be made for the time histories of dissipated fracture energy and stored elastic energy which are, however, not shown here for the sake of conciseness. The present scheme reduces the computational cost of implicit computations significantly while offering desirable accuracy.

In order to show that the numerical results are insensitive to the penalty number, we repeated the implicit computation for mesh 1 with $\chi = 2$ and $\chi = 5$ in addition to the previously used value of $\chi = 10$. The smallest penalty used, i.e. the one corresponding to $\chi = 2$, is as low as, approximately, $75H_c$. The final activated interfaces and the time histories of the dissipated fracture energy and stored elastic energy obtained with different values of χ exhibit excellent agreement, as shown in Figures 3.10 and 3.11. In Figure 3.12a we also report convergence profiles of the block-CD iteration at a representative time after initiation of cracks. Robustness of the algorithm is not affected by the magnitude of the penalty and a similar stable behavior is observed for different values of χ. We, however, note that the number of iterations required for convergence increases with the size of the time step. For instance, typical convergence profiles corresponding to $\Delta t = 5\Delta_{\text{cr}}$ and $\Delta t = 2\Delta_{\text{cr}}$ are compared in 3.12b. The average number of iterations was 19 for $\Delta t = 5\Delta_{\text{cr}}$.

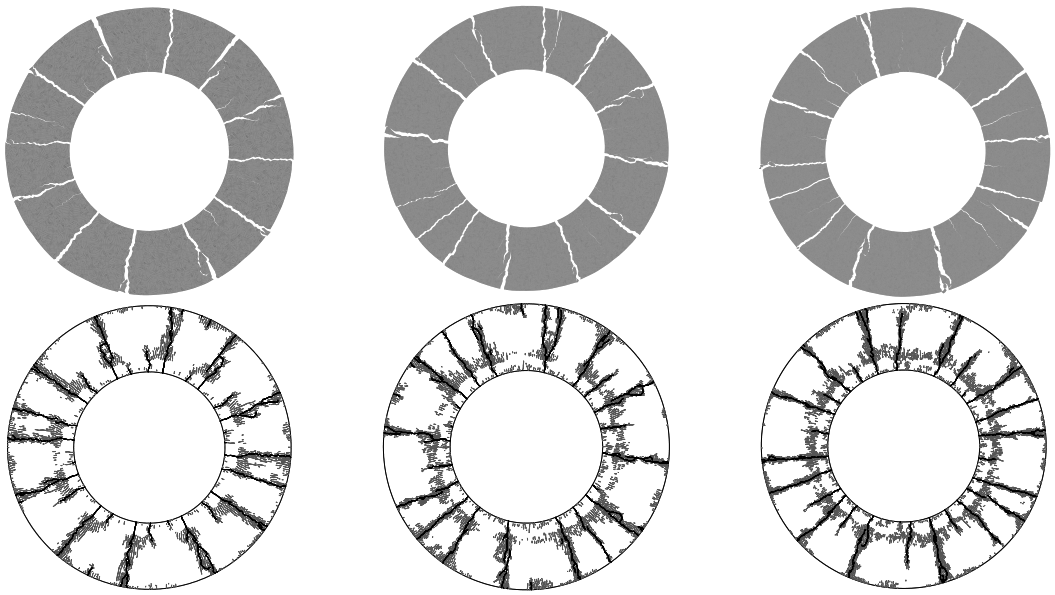

Figure 3.9: Final deformed meshes (magnified 10 times) and activated interfaces obtained in the alternative implicit computations (nonconverged, with one passing of block-CD iterations) at $T = 85$ μs

3.5.2 Dynamic crack branching instability

In this example, we consider crack branching in a pre-cracked block loaded dynamically in tension. Experimental test results have been reported by Sharon and Fineberg [130, 149] and the problem has been extensively studied numerically using different methods including XFEM and cohesive element methods [13, 105, 121], phase field [18, 97, 106] and peridynamics [16, 67]. Ganguly [53] and Ganguly and Papoulia [54] reported in detail on the mesh sensitivity of a similar problem. The geometric configuration and material properties taken from Nguyen and Wu [106] are summarized in Figure 3.13. These material properties lead to a characteristic fracture process length of $l_c = 0.27$ mm obtained from equation (3.30). A uniform tension $\sigma_0 = 1.0$ MPa is applied at the top and bottom edges of the specimen as a step function in time.

The mesh used consists of 28106 elements which are more refined in an area ahead of the notch-tip with an average size of 0.08 mm. For this problem, we used both implicit and explicit time-stepping schemes for a total simulation time of $T = 80$ μs. Explicit computations were performed using $\Delta t = 0.8\Delta_{\text{cr}}$, whereas implicit computations were performed

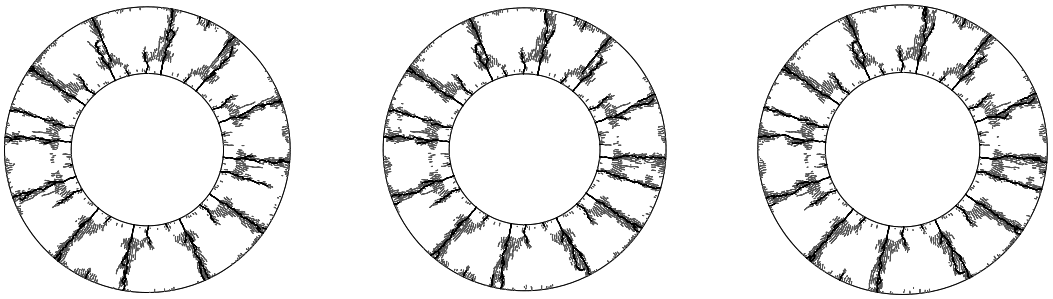

$\chi = 2$ $\chi = 5$ $\chi = 10$

Figure 3.10: Comparison of activation patterns obtained with different magnitudes of the penalty number for fragmentation of a thick cylinder using mesh 1

using $\Delta t = 2\Delta t_{\text{cr}}$ with $\text{tol}_R = 5 \times 10^{-3}$ and $\text{tol}_d = 10^{-7}$. The final deformed geometries and crack activation patterns obtained by the two schemes were seemingly identical. We show the results obtained by the explicit scheme in Figure 3.14. Slight differences between the upper and lower branches of the crack are due to asymmetry of the mesh. Some micro-branching right before the major branching occurs could be the signature of roughening of crack faces [130, 149] and resembles the widening of smeared crack/damaged zone in phase filed [18] and peridynamic simulations [67]. It is worth mentioning that a minimum of four Gauss points was found necessary for numerical integration along interface elements (i.e., four opening nodes per interface) to obtain satisfactory results in this simulation. We note that, in our setting, each interface Gauss point is a potential site of crack nucleation. The minimum number of Gauss points was not chosen based on accuracy of the numerical integration but, rather, for increased resolution in the representation of potential loci of crack branching along the major crack-tip trajectory.

We report the global response of the plate obtained using implicit and explicit schemes in Figures 3.15 and 3.16. These include the time histories of the stored elastic energy and the dissipated fracture energy and the time history of the crack-tip velocity, respectively. In both implicit and explicit schemes, the cracks initiate from the notch-tip at around 11.2 μs and propagate for a length of approximately 14.6 mm until major branching occurs at around 29.6 μs. The tips of the lower and upper crack branches reach to the right edge of the plate at around 71.1 μs. The crack-tip velocities always remain below the Rayleigh wave speed $v_R = 2125$ m/s [121] with a maximum of approximately $0.66v_R = 1400$ m/s. These results are all in good agreement with numerical results reported previously in the literature, e.g., [106, 121, 18, 16].

In order to further exemplify the capabilities of the method in modelling multiple

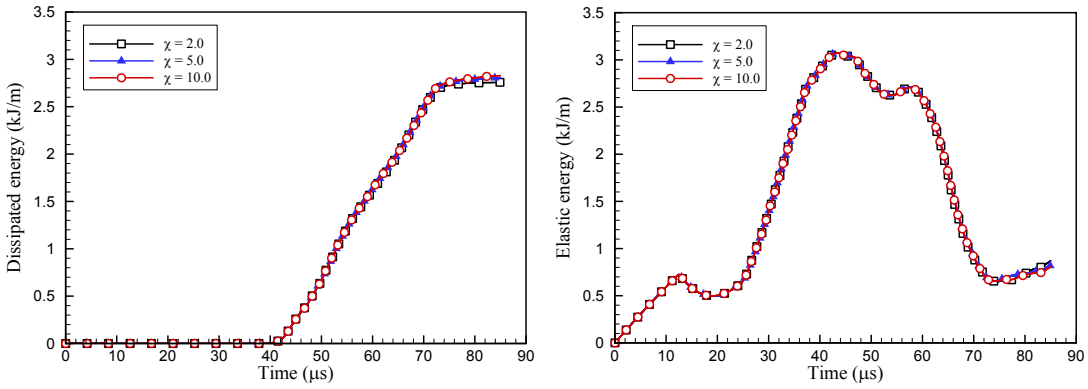

(a) (b)

Figure 3.11: Comparison of a) dissipated fracture energies and b) stored elastic energies obtained with different magnitudes of the penalty number for fragmentation of a thick cylinder using mesh 1

branches, we repeated the simulation with $\sigma_0 = 3$ MPa using explicit time-stepping. For this simulation, we introduced randomness in the material strength to break the symmetry of the model and facilitate crack branching at random locations of the mesh. The randomness introduced follows the modified weakest link Weibull distribution proposed by Zhou and Molinari [182], in which the probability of introducing a weak cohesive element is set to increase with element size. The Weibull modulus m in the modified Weibull distribution (see [182]) was taken to be 25. The activation patterns given in Figure 3.17 at different instants of the simulation show multiple branches and suggest that crack branching happens earlier than in the case of $\sigma_0 = 1.0$ MPa and at a smaller angle. Similar observations were reported in [16, 106].

3.5.3 Mixed-mode crack propagation under impulsive loading: the Kalthoff test

A doubly notched specimen under impact loading is investigated in this final example. The problem set up together with the relevant material properties and boundary conditions are shown in Figure 3.18a. This problem was originally proposed by Kalthoff and Winkler [77], who investigated failure mode transition from brittle fracture at an angle of approximately 70° to shear band formation at an angle of about −10° by varying the loading rate. Here, we focus on brittle fracture which occurs at relatively lower loading rates by imposing a

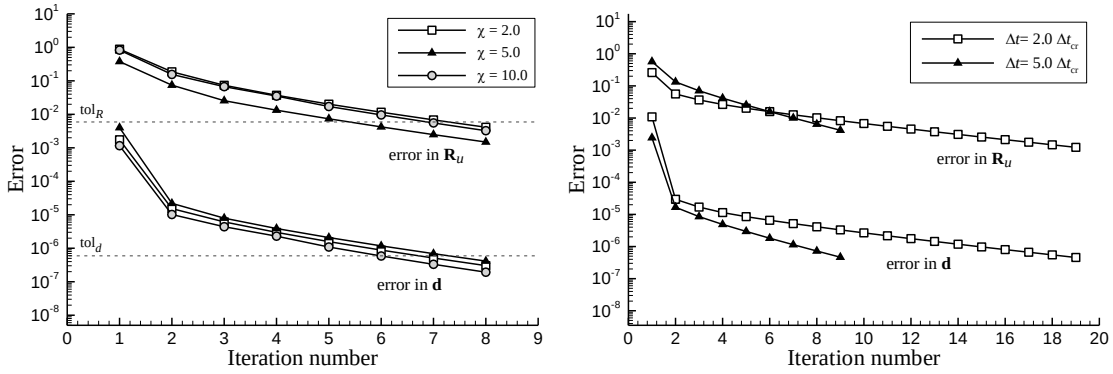

(a) (b)

Figure 3.12: Convergence profiles of the block-CD iterations a) for $\Delta t = 2\Delta t_{\mathbf{cr}}$ and different values of χ and b) for different values of Δt with $\chi = 10$

velocity boundary condition of $v_0 = 16.54$ m/s [121] at the bar-specimen interface. By taking advantage of the twofold symmetry of the experimental setup, only half of the specimen is considered in numerical simulations, see Figure 3.18b. The problem has also been simulated numerically by several researchers using different methods, see e.g. Park et al. [121] (interface elements), Song and Belytschko [153] (XFEM), Borden et al. [18] and Nguyen and Puh [106] (phase field). The characteristic length of the cohesive process zone is $l_c = 0.61$ mm. Material properties and other input parameters were taken from Park et al. [121].

We considered two meshes and performed time-stepping explicitly with $\Delta t = 0.8\Delta t_{\text{cr}}$ for a total simulation time of $T = 85$ μs. In both meshes, most elements are clustered in the "crack zone", the upper-right block of the domain where a crack is expected (see Figure 3.18b). The average element size in the crack zone is approximately 0.17 mm in the "coarse" mesh and 0.11 mm in the "fine" mesh. A comparison of the final crack paths obtained by the two meshes together with the final deformed geometry of the specimen obtained using the fine mesh are shown in Figure 3.19. In both cases, the crack initiates from the notch-tip at around 19.5 μs and reaches the top boundary of the specimen at around 78.9 μs. The crack trajectories are not generally straight and the propagation angles become slightly smaller at intermediate stages of the simulation. Nonetheless, the overall crack path remains fairly close to the experimental observation in both meshes so that that the average angle is 67.2° in the fine mesh and 65.3° in the coarse mesh.

Next, in Figure 3.20 we show the time histories of the dissipated fracture energy and of the stored elastic energy. Results of the two meshes are in good agreement so that

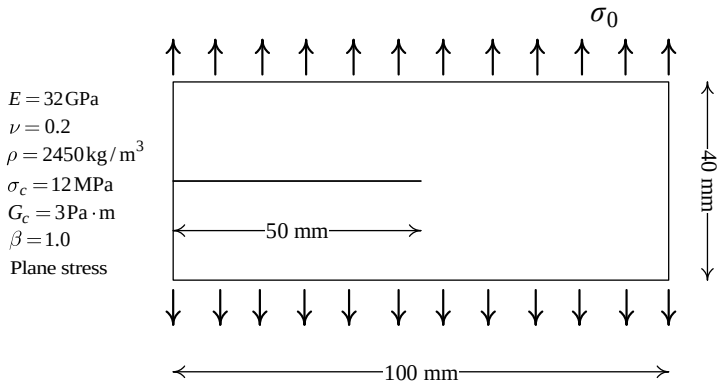

Figure 3.13: Dynamic crack branching instability; problem definition and relevant properties

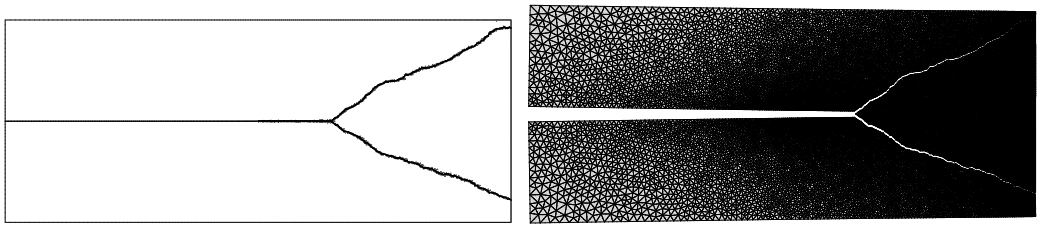

Figure 3.14: Dynamic crack branching instability; final deformed geometry (magnified 20 times) and crack activation patterns

the total dissipated energy (i.e., the final values of dissipated energy at the end of the simulation) obtained by the two meshes show less than %5 difference. Finally, we show in Figure 3.21 the time histories of the crack-tip velocities obtained using the coarse and fine meshes. Consistent with existing numerical simulation results [121, 153], the crack propagation velocities remain well below the Rayleigh wave speed $v_R = 2800$ m/s with an average of approximately $0.55 v_R = 1550$ m/s.

3.6 Conclusion

In keeping with recent developments of energy approaches to fracture, the proposed method has a firm physical basis and significantly simplifies the numerical implementation of initially-rigid cohesive zone models. In each of its iterations, the algorithm obtains crack opening displacements at each interface Gauss point locally through minimization of a

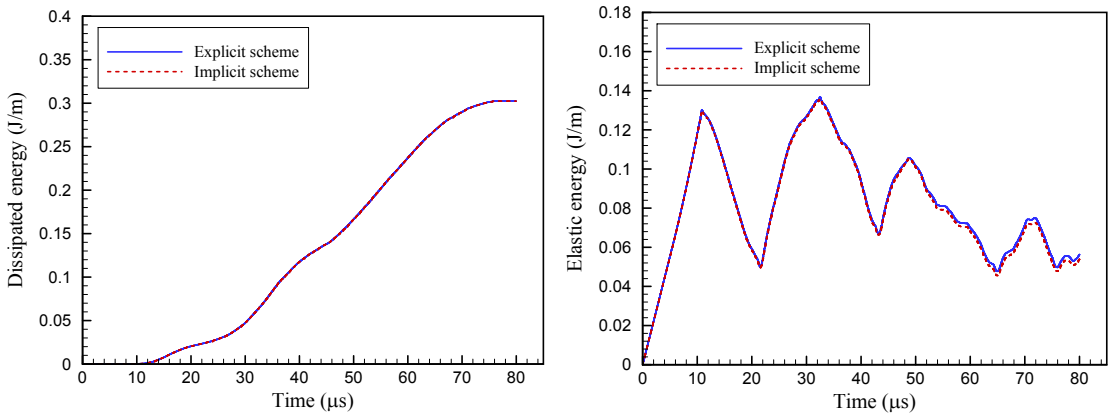

(a) (b)

Figure 3.15: Time histories of the a) dissipated fracture energy and b) stored elastic energy obtained using explicit and implicit schemes for dynamic crack branching instability

nondifferentiable functional. These are then enforced, in a numerically consistent manner, on the deformation of the finite element mesh at the inter-elements boundaries. Notably, both implicit and explicit time-stepping schemes are possible for advancing the solution of the nondifferentiable energy minimization problem in time. Furthermore, the method offers desirable exibility from a computer programming perspective: it can be implemented within an existing solid mechanics finite element code with minimal effort. Robustness of the method was shown by presenting various numerical simulation results obtained with both explicit and implicit time-stepping schemes for a range of problems involving branching and fragmentation.

In the present work, potential crack paths were *a priori* limited to the set of inter-element boundaries of the finite element triangulation. In a more general analysis, the orientation of the cracks (or the finite element triangulation itself) may be viewed as an additional unknown field in the context of optimization. Future efforts may be made in the direction of such analysis by using adaptive schemes or other discretization methods such as the extended finite element method.

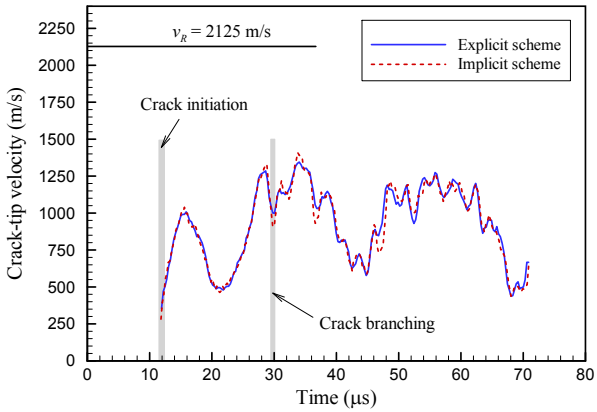

Figure 3.16: Time histories of the crack-tip velocity obtained using explicit and implicit schemes for dynamic crack branching instability. After branching, the reported crack-tip velocity is that of the lower branch

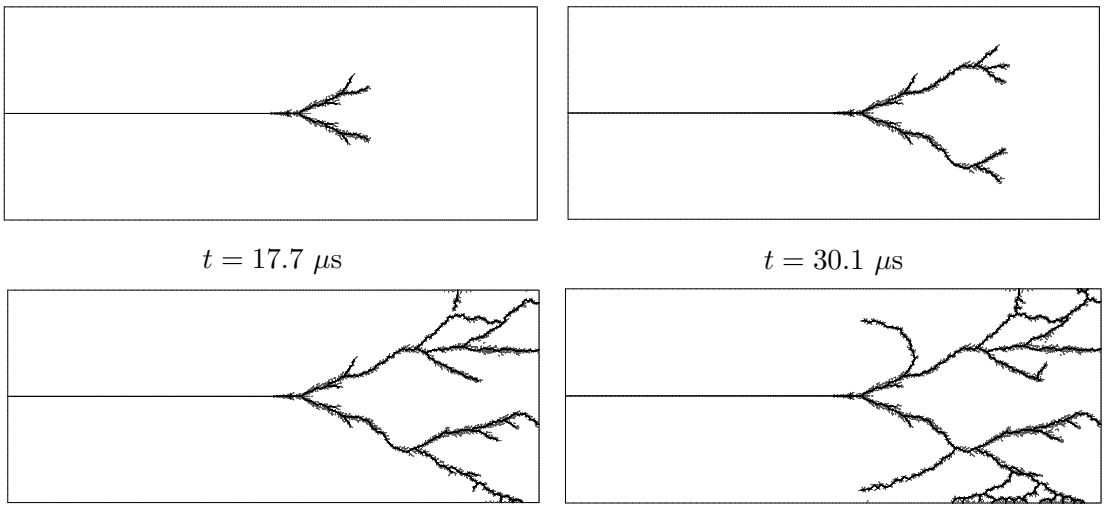

Figure 3.17: Dynamic crack branching instability; crack patterns at different instants obtained with $\sigma_0 = 3.0$ MPa

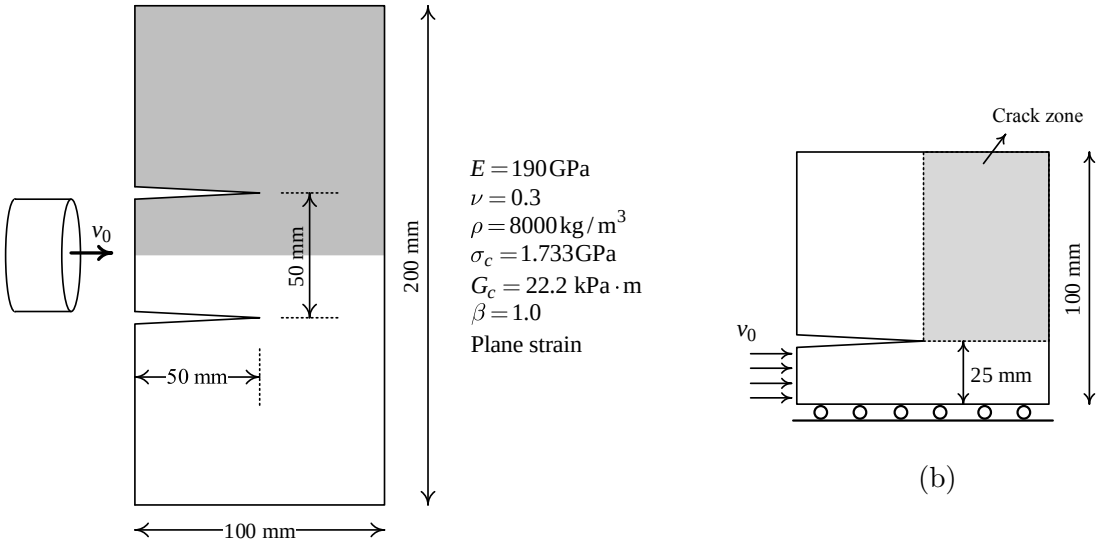

(a) (b)

Figure 3.18: Mixed mode crack propagation under impulsive loading (the Kalthoff test); a) problem definition and relevant properties, b) computational set up

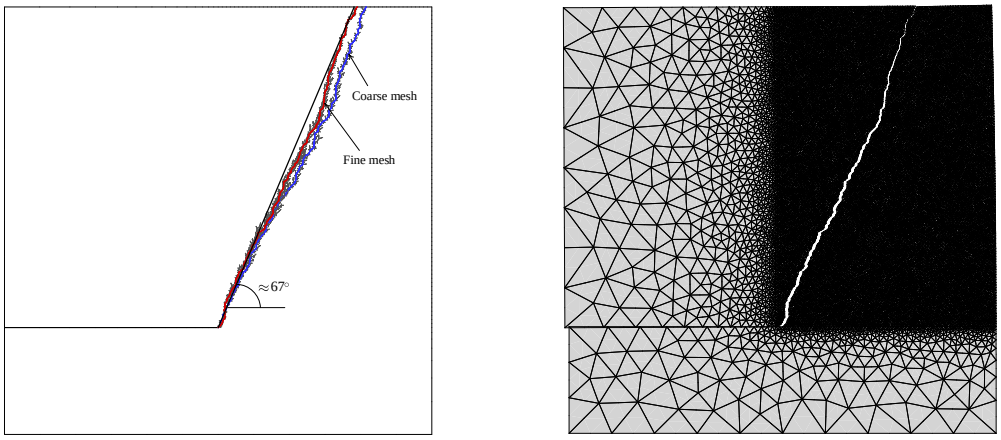

(a) (b)

Figure 3.19: Mixed mode crack propagation under impulsive loading (the Kalthoff test); a) crack activation patterns obtained using the fine and coarse meshes, b) final deformed geometry obtained using the fine mesh

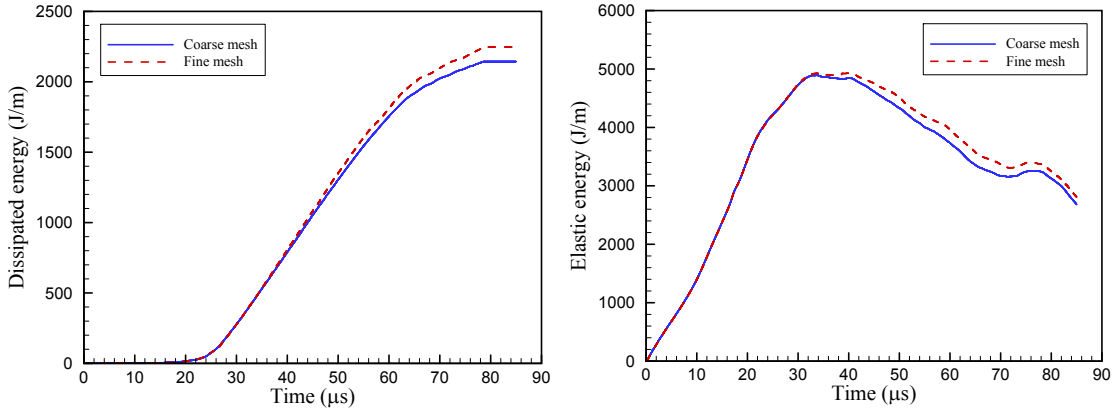

(a) (b)

Figure 3.20: Time histories of a) dissipated fracture energy and b) stored elastic energy for mixed mode crack propagation under impulsive loading (the Kalthoff test)

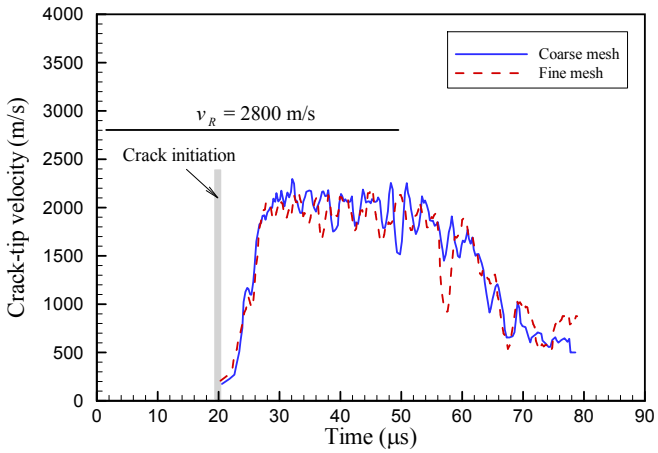

Figure 3.21: Time histories of the crack-tip velocity obtained using coarse and fine meshes for mixed mode crack propagation under impulsive loading

Chapter 4

Robust simulation of hydraulically driven fracture networks in naturally fractured impermeable media

This chapter is based on the following journal article:

Hirmand MR, Vahab M, Papoulia KD and Nasser K, Robust simulation of hydraulically driven fracture networks in naturally fractured impermeable media. *Computer Methods in Applied Mechanics and Engineering*, in review (2019), manuscript ID: CMAME-D-19-00248.

This paper was co-authored by myself, my supervisor, Dr. Papoulia, and by our research collaborators, Dr. Nasser Khalili, Professor of Geotechnical Engineering, and Dr. Mohammad Vahab, post-doctoral fellow, in the Department of Civil and Environmental Engineering at the University of New South Wales, Australia. As the first author, I designed the collaborative work, developed the computational formulation and wrote the manuscript. I also worked with the second author (Dr. Mohammad Vahab) in the implementation of the proposed algorithms and conducted the numerical simulations. Dr. Papoulia and Dr. Khalili were involved in overseeing the formulation and editing the manuscript. At the time of this writing, the paper is under revision.

4.1 Introduction

Hydraulic fracturing, a.k.a. fracking, is the process of injecting a highly-pressurized water mixture into subterranean rocks to generate a permeable fracture network. Hydraulic fracturing treatments have been widely used as a well-stimulation technique in low-permeability oil and gas reservoirs to make economic exploitation possible [158]. Among other examples of hydraulically driven fractures one can name structural failure in gravity concrete and rock-fill dams [145, 81, 79]. In that case, hydraulically driven fractures form due to an over-topping wave acting on the body of the dam.

Besides analytical solutions proposed for simplified hydraulic fracture settings [63, 155, 40, 41], different numerical methods have been used to model hydraulic fracturing including interface element methods [17, 145, 2, 28], mesh-free methods [168, 65, 160, 141], extended finite element methods [87, 135, 136, 81, 64], and phase-field methods [170, 98, 171], among many others. For a more comprehensive review of the numerical modelling of hydraulic fracturing, the interested reader is referred to a recent review by Lecampion et al. [86]. Schrefler and coworkers pointed out that a fully-dynamic simulation should be applied "in most fracturing events" [26] and that "there should be no restriction on the fracture velocity" [126] in a physically sound hydraulic fracturing model.

Time-discontinuity is especially problematic in the context of dynamic hydraulic fracturing and, as we show later in this chapter, a solution may not be obtained if a time-discontinuous fracture model is used. The reason is that the mass balance equation governing fluid flow within the hydro-fractures is dependent on the crack opening velocity field, whose numerical solution shows spurious oscillations in any time-discontinuous model. One expects that similar issues may be encountered in any coupled, multi-physics problem in which crack opening velocity fields play a role in the distribution of the local interfacial fields, e.g., rate dependent [183, 19] or thermo-chemo-mechanical fracturing processes [162, 58]. Most previous hydraulic fracturing models have simply sought to avoid this issue by neglecting inertial effects and by keeping the crack fixed within the computations of a solution step. This is not a coincidence but a manifestation of the robustness issues in previous hydraulic fracturing implementations using time-discontinuous crack propagation algorithms. The non-differentiable energy minimization approach avoids spurious velocity fields thus makes possible robust implementation of dynamic hydraulic fracturing in a way that no additional restriction is made on the crack-tip velocity.

We will assume in our hydro-mechanical modelling that the hydraulic fracturing process occurs in an impermeable domain in a short period of time. Accordingly, the fluid flow is defined only on the hydro-fracture network boundaries. The set of coupled hydro-mechanical equations governing the hydraulic fracturing problem is solved using a block-CD

solution strategy similar to the one proposed in Chapter 3. It is understood that sequential solution methods sometimes suffer from convergence issues in hydraulic fracturing problems especially in cases that the fracture toughness is relatively low [64, 119]. To avoid such complexities and focus our attention to issues arising form lack of time continuity, we restrict our simulations to "toughness dominated" hydraulic fracturing (i.e., relatively high fracture toughness). In addition, we use adequately small time steps so that an accurate solution can be obtained in only one passing of block-CD iterations in each time increment.

Another limitation in the hydraulic fracture literature is that the problem set up is in most cases limited to a single hydro-fracture approaching one or a few pre-existing discontinuities, see e.g., [82, 159, 181, 80, 83]. Despite the large body of work in this area, realistic simulation of hydraulic fracturing in naturally fractured formations still remains a formidable task. In our setting, multiple discontinuities can initiate and propagate along the inter-element boundaries (interface elements) anywhere in the mesh. Thus, the method offers desirable flexibility in modelling multiple hydraulic fractures in naturally fractured media. Identifying the set of pressurized fractured interfaces would not be a trivial task in this context and requires analyzing the complex topological information of the fractured interfaces in the finite element mesh. We propose a search algorithm on the basis of graph theory to identify, among all, the set of fractured interfaces subjected to the fracturing fluid pressure. The versatility of graph theory in tracking complex fracture networks is demonstrated in the literature by several authors, see e.g., [34, 179]. A consequence of this approach is that different interaction scenarios including coalescence, diversion of flow into the faults, offset crack propagation, etc. can be modelled in a unified fashion in the present approach.

This chapter is organized as follows. In Section 4.2, we state the problem and assumptions made. Formulation of the energy approach to hydraulic fracturing and its discontinuous Galerkin finite element implementation are presented in Section 4.3. In section 4.4, we present the coupled block-CD algorithm proposed for the solution of the coupled hydro-mechanical problem. The algorithm involves a two-step scheme in each iteration, in which the set of mechanical and hydraulic unknowns are updated sequentially. Section 4.5 is devoted to numerical simulation results which show the robustness of the proposed computational algorithm in modelling multiple hydraulic fracture growth in naturally fractured media. Finally, concluding remarks are presented in Section 4.6.

4.2 Problem statement and assumptions

Consider a quasi-brittle impermeable solid body $\Omega \subset \mathbb{R}^{n_{\text{dim}}}$ in 2D ($n_{\text{dim}} = 2$), containing a set of evolving *hydro-fractures* driven by injection of a fracturing fluid as well as a set of pre-existing fractures and/or weak surfaces, as shown in Figure 3.1. We assume that the evolution of hydro-fractures is restricted to a set of *a priori* known internal discontinuity boundaries $\Gamma_d \subset \Omega$. To allow for the hydro-fractures to merge/collide with the pre-existing discontinuities in the body, we require Γ_d to encompass all preexisting discontinuity boundaries, if any exist. We denote by p_{inj} the possibly time-dependent injection pressure and let the injection point be $\mathbf{x}_{\text{inj}} \in \Gamma_d$.

The deformation of the fracturing body is described by a displacement field $\mathbf{u}(\mathbf{x}, t) : \Omega \to \mathbb{R}^{n_{\text{dim}}} \times [0, T)$ admitting a jump $[\![\mathbf{u}(\mathbf{x}, t)]\!]$ on Γ_d. On the basis of the non-differentiable energy minimization approach to cohesive fracture, the evolution of cracks with nonzero displacement jumps within Γ_d is tracked by defining an auxiliary discontinuity opening displacement field $\boldsymbol{\delta}(\mathbf{x}, t) : \Gamma_d \to \mathbb{R}^{n_{\text{dim}}} \times [0, T)$ and requiring that

$$\boldsymbol{g}(\mathbf{u}, \boldsymbol{\delta}) \equiv [\![\mathbf{u}(\mathbf{x}, t)]\!] - \boldsymbol{\delta}(\mathbf{x}, t) = \mathbf{0} \quad \text{on } \Gamma_d. \tag{4.1}$$

The normal and sliding components of the displacement jump are defined as $[\![u_n]\!] = [\![\mathbf{u}]\!] \cdot \mathbf{n}_d$ and $[\![\mathbf{u}_s]\!] = [\![\mathbf{u}]\!] - [\![u_n]\!]\mathbf{n}_d$, where $\mathbf{n}_d$ is the unit normal to the discontinuity. Similar definitions are made for the auxiliary opening field $\boldsymbol{\delta}$.

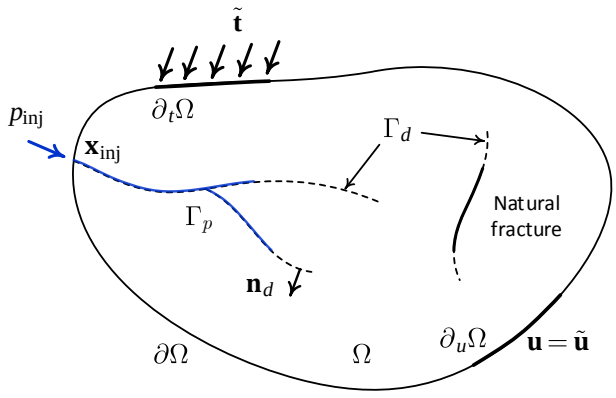

Figure 4.1: Schematic of a naturally fractured body Ω. Γ_d represents potential sites of cracks and discontinuities whereas $\Gamma_p \subseteq \Gamma_d$ represents the hydro-fractures pressurized by the fracturing fluid. The external boundary $\partial\Omega$ consists of disjoint parts $\partial_u\Omega$ and $\partial_t\Omega$ ($\partial_u\Omega \cap \partial_t\Omega = \emptyset$ and $\partial_u\Omega \cup \partial_t\Omega = \partial\Omega$), on which the displacement $\widetilde{\mathbf{u}}$ and external force $\widetilde{\mathbf{t}}$ are prescribed, respectively

We assume infinitesimal deformations and consider the standard theory of linear elasticity for isotropic solids. The strain energy density function ψ is defined on the "uncracked" part of the body $\Omega \backslash \Gamma_d$ as

$$\psi(\boldsymbol{\varepsilon}(\mathbf{u})) = \frac{1}{2}\boldsymbol{\varepsilon}(\mathbf{u}) : \mathbf{D} : \boldsymbol{\varepsilon}(\mathbf{u}), \tag{4.2}$$

where $\mathbf{D}$ is the elasticity constitutive tensor and $\boldsymbol{\varepsilon}(\mathbf{u}) = \nabla^s \mathbf{u} \in \mathbb{R}^{n_{\text{dim}}} \times \mathbb{R}^{n_{\text{dim}}}$ is the infinitesimal strain tensor. Further, we define an opening-dependent cohesive surface energy function $\psi_{\text{cohs}}(\boldsymbol{\delta}; \delta_{\max})$ and an indicator function $I_{\mathbb{R}^+}(\delta_n)$ on Γ_d. The surface energy function ψ_{cohs} involves three material constants, σ_c, δ_c and β, which represent material strength under normal tensile load, critical effective opening displacement at loss of cohesion and shear to normal material strength ratio, respectively. Furthermore, $\delta_{\max}$ is a history variable taking into account the irreversibility of the fracturing process. The indicator function $I_{\mathbb{R}^+}$ is introduced to prohibit interpenetration of the crack faces. We recall that both of these functions are nondifferentiable at their origins as a requirement for modelling the initially-rigid behavior on Γ_d. For the precise forms of ψ_{cohs} and $I_{\mathbb{R}^+}$ used here, the reader is referred to Chapters 2 and 3.

The hydraulic response of the fluid within the hydro-fractures is described by introducing a scalar fluid pressure field $p(\mathbf{x}, t) : \Gamma_p \to \mathbb{R} \times [0, T)$, where $\Gamma_p(t) \subseteq \Gamma_d$ denotes the set of hydro-fracture boundaries pressurized by the fracturing fluid. We consider that Γ_p is formed of a subset of inter-connected, fully-cracked surfaces in Γ_d that are linked to the fluid injection point $\mathbf{x}_{\text{inj}}$. Thus, $\mathbf{x}_{\text{inj}} \in \Gamma_p$. We further assume that the entire length of Γ_p is filled with fluid; that is, the so called *fluid-lag* zone is assumed to be of negligible size [56, 57]. It is noted that the interaction of the hydraulically driven fractures with each other and with pre-existing discontinuities may lead to the formation of cracks away from the hydraulically driven fractures which are not in Γ_p. Thus, the domain Γ_p is not known *a priori* in the present setting.

We assume that the fracturing fluid is incompressible and that the flow within the hydro-fractures is fully-developed and laminar at any instance of time during fracturing. Furthermore, we assume that the fluid flow within the hydro-fractures is one-dimensional and that the flow exchange between the hydro-fracture and the surrounding medium is insignificant compared to the one-dimensional flow within the hydro-fracture. Consider the local Cartesian coordinate system (s, r) defined on Γ_p as shown in Figure 4.2. The directions of s and r are aligned with the tangent and normal to the discontinuity boundary, respectively. The longitudinal rate of flow q within a fracture is described by Darcy's law as

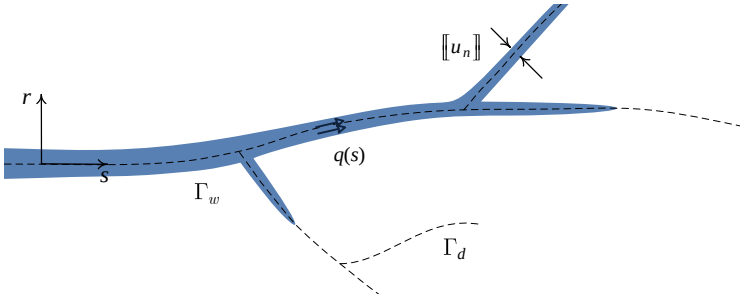

Figure 4.2: Schematic of the hydro-fracture and relevant definitions

$$q = -k\frac{dp}{ds}, \tag{4.3}$$

in which k is the longitudinal permeability of the flow canal between the hydro-fracture faces. In the above, the pressure field p is taken to be positive in compression. By Poiseuille's law, the hydro-fracture permeability k may be related to its opening by

$$k = \frac{h_H^3}{12\mu_f} \simeq \frac{1}{f}\frac{[\![u_n]\!]^3}{12\mu_f}, \tag{4.4}$$

in which h_H is the so-called *hydraulic aperture* of the crack, μ_f is the fracturing fluid viscosity, and $1.04 \leq f \leq 1.65$ is a coefficient that accounts for the deviation from the ideal conditions of parallel, smooth hydro-fracture faces [172, 184]. To summarize, the complete hydro-mechanical response of the hydraulically fractured body is described by three independent variables $\mathbf{u}$, $\boldsymbol{\delta}$ and p.

4.3 Formulation of the hydraulic fracturing problem

4.3.1 The coupled hydro-mechanical model

The complete hydro-mechanical response of the hydraulically fractured body is described by two equations, one describing the mechanical equilibrium of the fractured body and the other describing mass balance of the fluid within the hydro-fractures. An expression of the total mechanical energy of the body is obtained as the sum of energy due to elastic strain of the body $\pi_{\text{el}}(\mathbf{u})$, dynamic energy due to inertial forces $\pi_{\text{dyn}}(\mathbf{u})$, energy due to opening of the interfaces $\pi_{\text{intf}}(\boldsymbol{\delta})$ and energy due to work of the fluid pressure on the crack faces $W_{\text{fluid}}(\mathbf{u}; p)$:

$$\pi(\mathbf{u},\boldsymbol{\delta};p)=\pi_{\text{el}}(\mathbf{u})+\pi_{\text{dyn}}(\mathbf{u})+\pi_{\text{intf}}(\boldsymbol{\delta})-W_{\text{ext}}(\mathbf{u})-W_{\text{fluid}}(\mathbf{u};p), \tag{4.5}$$

where

$$\begin{aligned}
\pi_{\text{el}}(\mathbf{u}) &= \int_{\Omega\setminus\Gamma_d} \psi\left(\boldsymbol{\varepsilon}(\mathbf{u})\right)\, dV,\\
\pi_{\text{intf}}(\boldsymbol{\delta}) &= \int_{\Gamma_d} \left(\psi_{\text{cohs}}(\boldsymbol{\delta})+I_{\mathbb{R}^+}(\delta_n)\right)\, dS,\\
W_{\text{ext}}(\mathbf{u}) &= \int_{\Omega\setminus\Gamma_d} \mathbf{u}\cdot\mathbf{b}\, dV+\int_{\partial_t\Omega}\mathbf{u}\cdot\widetilde{\mathbf{t}}\, dS,\\
W_{\text{fluid}}(\mathbf{u};p) &= \int_{\Gamma_p}[\![\mathbf{u}]\!]\cdot p\mathbf{n}_d\, dS,
\end{aligned} \tag{4.6}$$

and the dynamic energy term $\pi_{\text{dyn}}(\mathbf{u})$ is chosen in such a way that the following relation holds at each time step in a time-discrete framework

$$\nabla_{\mathbf{u}_i}\pi_{\text{dyn}}(\mathbf{u}_i)=\int_{\Omega\setminus\Gamma_d}\rho\ddot{\mathbf{u}}_i dV, \tag{4.7}$$

where the subscript i denotes finite difference approximation to the corresponding unknown. In the definition of W_{ext}, $\mathbf{b}$ is the body force vector and $\widetilde{\boldsymbol{\tau}}$ is the prescribed traction on $\partial_t\Omega$. The mechanical equilibrium of the fractured body is characterized by the following constrained minimization problem at each time step:

$$\text{find } (\mathbf{u}^\star,\boldsymbol{\delta}^\star)\in(\mathcal{U}\times\mathcal{D}) \text{ minimizing } \pi(\mathbf{u},\boldsymbol{\delta};p) \text{ s.t. } \boldsymbol{g}(\mathbf{u},\boldsymbol{\delta})=\mathbf{0}, \tag{4.8}$$

where $\mathcal{U}$ and $\mathcal{D}$ are spaces of admissible solutions and $\boldsymbol{g}(\mathbf{u},\boldsymbol{\delta})$ is a linear constraint function defined in (4.1).

The above mechanical equilibrium equation is complemented by the following mass balance boundary value problem that governs variation of the fluid pressure field p within the hydro-fractures [80],

$$\frac{dq}{ds}+[\![\dot{u}_n]\!]=0 \text{ on } \Gamma_p;\quad p(\mathbf{x}_{\text{inj}})=p_{\text{inj}}. \tag{4.9}$$

We note that the hydro-mechanical coupling between the deformation of the fractured body and the fluid pressure is achieved by the introduction of the work of pressure field W_{fluid} in the total energy functional (4.7) and the dependence of the fluid pressure p on $[\![u_n]\!]$ through (4.4) and (4.9).

Remark 1. The crack opening displacement field $\boldsymbol{\delta}$ could be used instead of the displacement jump $[\![\mathbf{u}]\!]$ in the definition of W_{fluid} and in equations (4.4) and (4.9). In numerical experiments, we found that results are at least seemingly identical, even though the computational algorithm proposed in Section 4.4 would be slightly different if the coupling between the solid and the fluid problem is made through $\boldsymbol{\delta}$.

4.3.2 Finite element discretization

The coupled problem defined by the system of equations (4.8) and (4.9) is solved by means of finite element discretization. The finite element discretization is applied directly to the minimization problem (4.8) to arrive at the finite-dimensional minimization problem describing equilibrium and fracture in the body. This equation is solved simultaneously with the discrete form of the mass balance equation (4.9) obtained through a standard finite element weak formulation.

The finite element discretization of $\mathbf{u}$ and $\boldsymbol{\delta}$ follows the DG scheme presented in Chapters 2 and 3. The finite element triangulation is denoted Ω_h, and $\Gamma_{d,h}$ is taken to be the union of nonexterior surfaces of the bulk elements in Ω_h. The finite element approximation $\mathbf{u}_h$ allows for a displacement jump $[\![\mathbf{u}_h]\!]$ on $\Gamma_{d,h}$. Furthermore, each Gauss point of the interface elements in $\Gamma_{d,h}$ is assigned a nodal opening displacement unknown to construct $\boldsymbol{\delta}_h$. The total number of Gauss points (opening nodal points) is denoted M and their coordinates are denoted $\boldsymbol{\xi}_I$, $I = 1, 2, ..., M$.

Next, the finite element discretization is completed by approximating the pressure filed p with a C^0-continuous approximation p_h on the domain of flow continuity equation $\Gamma_{p,h}$. The $(n_{\text{dim}} - 1)$-dimensional mesh constructed on $\Gamma_{p,h}$ for this purpose is assumed to be conforming to the underlying finite element mesh. That is, the nodal points that serve to interpolate the pressure field on $\Gamma_{p,h}$ are located at the vertices of the elements in Ω_h. In the subsequent presentation, $\mathbf{U}$, $\mathbf{d}$ and $\mathbf{P}$ denote the global vector of nodal unknowns corresponding to $\mathbf{u}_h$, $\boldsymbol{\delta}_h$ and p_h, respectively. Note that it is required that $\mathbf{u}_h = \widetilde{\mathbf{u}}$ on $\partial_u\Omega$ and $p_h(\mathbf{x}_{\text{inj}}) = p_{\text{inj}}$ for admissibility of the approximate solution fields.

The discontinuous Galerkin method is used to obtain the spatially discretized form of the constrained minimization problem (4.8) as

$$\min_{(\mathbf{U},\mathbf{d})} \left\{ \mathcal{L}^{\text{DG}}(\mathbf{u}_h, \boldsymbol{\delta}_h; p_h) = \pi(\mathbf{u}_h, \boldsymbol{\delta}_h; p_h) + \int_{\Gamma_{d,h}} \boldsymbol{\lambda}_h^{\text{DG}} \cdot \boldsymbol{g}_h dS \right\}, \tag{4.10}$$

in which $\boldsymbol{\lambda}_h^{\mathrm{DG}}$ is the DG numerical flux defined as

$$\boldsymbol{\lambda}_h^{\mathrm{DG}} = \langle \boldsymbol{\sigma}_h \rangle \, \mathbf{n}_d + \frac{1}{2}\eta \boldsymbol{g}_h. \tag{4.11}$$

In the above, $\boldsymbol{\sigma}_h$ is the Cauchy stress tensor computed strongly from $\mathbf{u}_h$, $\langle * \rangle = \frac{1}{2}(*^+ + *^-)$ and $\eta > 0$ is a sufficiently large penalty number (see Chapters 2 and 3 for a detailed discussion of the role of η regarding accuracy and convergence within the present formulation).

The mass balance equation (4.9) is solved for p simultaneously with (4.10) using a standard finite element discretization. Following the usual steps of the Bubnov-Galerkin technique, the finite dimensional weak form of the flow boundary value problem (4.9) that governs the evolution of the fluid pressure on $\Gamma_{p,h}$ is expressed as [80]

$$\int_{\Gamma_{p,h}} \frac{d\widehat{p}_h}{ds} k \frac{dp_h}{ds} \, dS - \int_{\Gamma_{p,h}} \widehat{p}_h [\![\dot{u}_n]\!] \, dS = 0, \tag{4.12}$$

which must be satisfied for any admissible test pressure function $\widehat{p}_h$. The test function $\widehat{p}_h$ is approximated similar to p_h except that $\widehat{p}_h(\mathbf{x}_{\mathrm{inj}}) = 0$. In the above, dS is a differential area which would be equal to Bds in a 2D setting, where B is the width of the hydro-fracture.

Note that, as mentioned previously, the domain $\Gamma_{p,h}$ is not known *a priori* within the present setting which naturally allows for the propagation of multiple hydro-fractures and pre-existing discontinuities in the mesh. In fact, $\Gamma_{p,h}$ needs to be determined as part of the solution by analyzing the topological information of the fully-cracked interface elements in $\Gamma_{d,h}$ within the present DG finite element discretization. As mentioned in the introduction, we propose a search algorithm on the basis of graph theory to identify the set of pressurized interface elements forming $\Gamma_{p,h}$, which will be discussed in further details in Section 4.4.2.

4.4 Computational procedure: coupled block-CD algorithm

In this section, we propose an iterative solution algorithm for the solution of the coupled system of hydro-mechanical equations defined by equations (4.10) and (4.12). The algorithm involves solution of the equilibrium problem (4.10) using a block-CD energy minimization in a way proposed in Chapter 3 simultaneously with the mass balance weak form (4.12).

We now categorize the set of unknowns to be obtained to two groups. The first group, denoted *mechanical unknowns*, consists of $\mathbf{U}$ and $\mathbf{d}$, and the second, denoted *hydraulic*

unknowns, involves $\Gamma_{p,h}$ and $\mathbf{P}$. Consider the time-discrete case, with uniform time step increments Δt, and suppose that the sets of mechanical and hydraulic unknowns $\{\mathbf{U}_i; \mathbf{d}_i\}$ and $\{(\Gamma_{p,h})_i; \mathbf{P}_i\}$ are known at time step t_i and sought at time step t_{i+1}. Each iteration of the algorithm involves a *mechanical update* step, which updates the mechanical unknowns by solving (4.8) with fixed hydraulic unknowns, followed by a *hydraulic update* step, which updates the hydraulic unknowns through the solution of (4.12) using the updated values of the mechanical unknowns.

The algorithm resulting from the above solution strategy, with a Newmark scheme [104] for the time integration of the displacement unknowns, is outlined in Algorithm 4.1. In the two subsections that follow, we discuss each of the mechanical and hydraulic update steps involved in the algorithm. In order to simplify the presentation, we shall omit the time step index i and the coupled block-CD iteration index j; the formulation that follows concerns a typical iteration of the algorithm at time step t_{i+1}.

4.4.1 Mechanical update step

The mechanical update step itself involves two sub-steps, in which $\mathbf{d}$ and $\mathbf{U}$ are updated sequentially assuming that the hydraulic unknowns $\{\Gamma_{p,h}, \mathbf{P}\}$ are fixed at their current values. These sub-steps are obtained using the block-CD algorithm as explained in Chapter 3.

The opening displacement unknowns are updated locally at each nodal point I defined on $\Gamma_{d,h}$ through the following algorithmic nondifferentiable minimization problem

$$\min_{\mathbf{d}_I} \left\{ \pi_\delta(\mathbf{d}_I, \mathbf{U}) = \psi_{\text{cohs}}(\mathbf{d}_I; \delta_{\max,I}) + I_{\mathbb{R}^+}(d_{n,I}) + \boldsymbol{\lambda}_{h,I}^{\text{DG}} \cdot \boldsymbol{g}_{h,I} \right\} \text{ for } I = 1 : M, \tag{4.13}$$

in which $\mathbf{d}_I$ is the nodal opening displacement at node (interface Gauss point) I. Because ψ_{cohs} and $I_{\mathbb{R}^+}$ are not globally differentiable, a straightforward solution of (4.13) is not readily available. A thorough explanation of the solution of (4.13) using generalized differential calculus is given in Chapter 3. The traction $\boldsymbol{\tau}_I$ appearing in the algorithm is computed strongly from the deformation field at interface Gauss point I as

$$\boldsymbol{\tau}_I = \langle \boldsymbol{\sigma}_h(\boldsymbol{\xi}_I) \rangle \, \mathbf{n}_d + \eta [\![\mathbf{u}_h(\boldsymbol{\xi}_I)]\!]. \tag{4.14}$$

In addition, τ_I is an effective norm of the tensile part of $\boldsymbol{\tau}_I$ defined as

$$\tau_I = \sqrt{\max(\tau_{n,I}, 0)^2 + \|\boldsymbol{\tau}_{s,I}/\beta\|^2}. \tag{4.15}$$

Algorithm 4.1 Coupled block-CD algorithm for hydraulic fracture propagation; the subscript $i+1$ is omitted for simplicity of presentation

Given mechanical unknowns $\{\mathbf{U}_i, \dot{\mathbf{U}}_i, \ddot{\mathbf{U}}_i, \mathbf{d}_i\}$ and hydraulic unknowns $\{\mathbf{P}_i, (\Gamma_{p,h})_i\}$

Update $\delta_{\max} = \max\{\delta_{\max,0}, ..., \delta_{\max,i}\}$ at all interface points $I = 1 : M$

Initiate iterations:

Mechanical unknowns: set $\mathbf{d}^0 = \mathbf{d}_i$ and Newmark's scheme *predictors*

$\mathbf{U}^0 = \mathbf{U}_i + \Delta t \dot{\mathbf{U}}_i + \frac{\Delta t^2}{2}\ddot{\mathbf{U}}_i$ and $\dot{\mathbf{U}}^0 = \dot{\mathbf{U}}_i + \Delta t \ddot{\mathbf{U}}_i$.

Hydraulic unknowns: set $\mathbf{P}^0 = \mathbf{P}_i$ and $\Gamma^0_{p,h} = (\Gamma_{p,h})_i$.

Loop on iterations $j = 0, 1, ...$

Mechanical update step

Update $\mathbf{d}$. For all interface points $I = 1 : M$ on $\Gamma_{d,h}$:

if $\tau_I^j \leq \sigma_c$, and $\delta_{\max,I} = 0$, **then**

pre-activation state with $\mathbf{d}_I^{j+1} = \mathbf{0}$

else

if $\tau_{n,I}^j \leq 0$, set $d_{n,I}^{j+1} = 0$ (contact case) and solve (4.13) for $\mathbf{d}_{s,I}^{j+1}$ only,

else, declare $d_{n,I}^{j+1} > 0$ and solve (4.13) for $\mathbf{d}_I^{j+1}$

end

Update $\mathbf{U}$:

$\Delta\ddot{\mathbf{U}}^{j+1} = -\mathbf{J}^{-1}\mathbf{R}_u(\mathbf{U}^j; \mathbf{d}^{j+1}, \mathbf{P}^j)$; then $\ddot{\mathbf{U}}^{j+1} = \ddot{\mathbf{U}}^j + \Delta\ddot{\mathbf{U}}^{j+1}$

$\mathbf{U}^{j+1} = \mathbf{U}^j + a_1 \frac{\Delta t^2}{2}\Delta\ddot{\mathbf{U}}^{j+1}$

$\dot{\mathbf{U}}^{j+1} = \dot{\mathbf{U}}^j + a_2 \Delta t \Delta\ddot{\mathbf{U}}^{j+1}$

Hydraulic update step

Update fluid pressure domain: $\Gamma^j_{p,h} \to \Gamma^{j+1}_{p,h}$

Identify fully-cracked interfaces, then form $\mathbf{G} = \{\mathbf{V}, \mathbf{E}\}$ and $\mathbf{C}$

Identify isolated sub-graphs $\overline{\mathbf{G}}_k = \left(\overline{\mathbf{V}}_k, \overline{\mathbf{E}}_k\right) \subseteq \mathbf{G}$

Find $\overline{\mathbf{V}}_{k'}$ s.t. $\gamma_{\text{inj}} \in \overline{\mathbf{V}}_{k'}$, then set $\Gamma_{p,h} = \overline{\mathbf{V}}_{k'}$

Update $\mathbf{P}$:

$\mathbf{P}^{j+1} = \left(\mathbf{H}^{j+1}\right)^{-1}\left(\mathbf{Q}_{pu}^{j+1}\dot{\mathbf{U}}^{j+1}\right)$

Set negative values in $\mathbf{P}^{j+1}$ to zero

Check for convergence:

if $\frac{\|\mathbf{R}_u^{j+1}\|}{\|\mathbf{R}_u^0\|} \leq \text{tol}_R$ and $\Gamma^{j+1}_{p,h} - \Gamma^j_{p,h} = \emptyset$, **go to** next time step

End Loop on iterations

Next, the displacement unknowns are updated through the solution of the following system of equations for $\mathbf{U}$,

$$\mathbf{R}_u(\mathbf{U};\mathbf{d},\mathbf{P}) \equiv \mathbf{M}\ddot{\mathbf{U}} + \mathbf{K}_{uu}\mathbf{U} - \mathbf{K}_{ud}\mathbf{d} - \mathbf{Q}_{up}\mathbf{P} - \mathbf{F}_{\text{ext}} = \mathbf{0}, \tag{4.16}$$

which characterizes the global equilibrium of the body subjected to opening displacements $\mathbf{d}$ and fluid pressure $\mathbf{P}$ at element edges. We refer the reader to Chapter 3 for definitions of the mass matrix $\mathbf{M}$, the stiffness matrices $\mathbf{K}_{uu}$, $\mathbf{K}_{ud}$ and the external forces vector $\mathbf{F}_{\text{ext}}$. The hydro-mechanical coupling matrix $\mathbf{Q}_{up}$ is defined as

$$\mathbf{Q}_{up} = \int_{\Gamma_{p,h}} (\mathbf{N}^{[\![u]\!]})^T \mathbf{n}_d \mathbf{N}^p \, dS, \tag{4.17}$$

in which $\mathbf{N}^{[\![u]\!]}$ and $\mathbf{N}^p$ are the matrices of finite element shape functions approximating $[\![\mathbf{u}_h]\!]$ and p_h, respectively. Equation 4.16 can be solved either implicitly or explicitly depending on the values of the Newmark scheme parameters a_1 and a_2 used (see Algorithm 4.1). An implicit scheme with unconditional stability corresponds to $a_1 \geq a_2 \geq 0.5$, whereas an explicit time-stepping scheme corresponds to $a_1 = 0$ and $a_2 = 0.5$. In Algorithm 4.1, we solve for $\ddot{\mathbf{U}}$ in an incremental fashion whereby an increment $\Delta\ddot{\mathbf{U}}$, obtained by evaluating the residual $\mathbf{R}_u$ at the current estimate of the solution, is used to update $\ddot{\mathbf{U}}$ in each iteration. The corresponding Jacobean matrix $\mathbf{J} = \partial\mathbf{R}_u/\partial\ddot{\mathbf{U}}$ is expressed as

$$\mathbf{J} = a_1 \frac{\Delta t^2}{2} \mathbf{K}_{uu} + \mathbf{M}. \tag{4.18}$$

4.4.2 Hydraulic update step

For a given set of mechanical unknowns $\{\mathbf{U}, \mathbf{d}\}$, fixed at their values obtained in the mechanical update step, we first construct the domain $\Gamma_{p,h}$ and then solve the weak from (4.12) for the pressure field on $\Gamma_{p,h}$.

The algorithm proposed for the construction of $\Gamma_{p,h}$ relies on concepts of graph theory. An undirected simple graph is constructed as an ordered pair $\mathbf{G} = (\mathbf{V}, \mathbf{E})$, in which $\mathbf{V}$ is the set of vertices and $\mathbf{E}$ is the set of edges. Each "vertex" in $\mathbf{V}$ is a fully-cracked interface element of the mesh. By fully-cracked we mean complete loss of cohesion ($\delta_{\max} \geq \delta_c$) at all Gauss points of the interface element. Edges in $\mathbf{E}$ are defined on the basis of the connectivity of interface elements; any two fully-cracked interface elements with at least one end point (in 2D) or boundary edge (in 3D) are linked by an "edge". Accordingly, an adjacency matrix $\mathbf{C}$ is defined in which $C_{ij} = 1$ if vertices (interfaces) i and j are

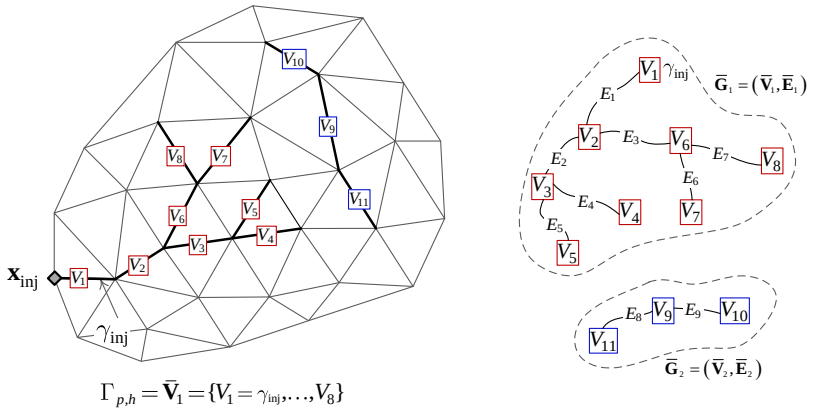

Figure 4.3: Example of the construction of the domain $\Gamma_{p,h}$ in a 2D mesh. The mesh is shown on the left and the associated graph, in which $K = 2$, is shown on the right. The thicker edges of the mesh denote fully-cracked interface elements

linked by an edge and $C_{ij} = 0$ otherwise. Using the pathway search algorithm introduced by Segdewick [146], the connectivity matrix is then used to identify the set of connected components (*isolated* sub-graphs) $\overline{\mathbf{G}}_k = \left(\overline{\mathbf{V}}_k, \overline{\mathbf{E}}_k\right) \subset \mathbf{G}$, $k = 1, .., K$, where K is the number of connected components, each formed by a subset of fully-cracked interface elements of the mesh. In a MATLAB script, this can be simply achieved using the "conncomp" command. Assuming a single crack emanating from the injection point (perforation), let γ_{inj} denote the interface element representing that crack. The set of interface elements defining $\Gamma_{p,h}$ is determined by the vertices of the isolated sub-graph that contains γ_{inj}; that is, one finds $\overline{\mathbf{V}}_{k'}$ s.t. $\gamma_{\text{inj}} \in \overline{\mathbf{V}}_{k'}$, $k' \in \{1, ..., K\}$, then sets $\Gamma_{p,h} = \overline{\mathbf{V}}_{k'}$. The above algorithm applies to a single injection point; however, it can be easily extended to the case of multiple injection points and/or multiple cracks emanating from each injection point. The algorithm described above is schematically shown in Figure 4.3

With $\Gamma_{p,h}$ constructed, the system of discrete finite element equations corresponding to (4.12), i.e., the system used to compute the distribution of the pressure field on $\Gamma_{p,h}$ reads

$$\mathbf{R}_p(\mathbf{P}; \mathbf{U}) \equiv \mathbf{H}\mathbf{P} - \mathbf{Q}_{pu}\dot{\mathbf{U}} = \mathbf{0}, \tag{4.19}$$

in which $\mathbf{Q}_{pu} = \mathbf{Q}_{up}^T$ and $\mathbf{H}$ is the hydro-fracture permeability matrix given by

$$\mathbf{H} = \int_{\Gamma_{p,h}} (\mathbf{B}^p)^T k \mathbf{B}^p \, dS, \tag{4.20}$$

with $\mathbf{B}^p = d\mathbf{N}^p/ds$ containing spatial derivatives of $\mathbf{N}^p$. Note that the domain $\Gamma_{p,h}$ may change from one iteration to the next. In consequence, the size of the system of equations (4.19) is not generally fixed within the iterations.

Convergence of the coupled block-CD algorithm is checked at the end of the hydraulic update step on the basis of the residual norm of the global equilibrium equation (4.16) and variation of $\Gamma_{p,h}$ in successive iterations.

Remark 2. *Treatment of fluid-lag.* The assumption of zero fluid-lag in $\Gamma_{p,h}$ may lead to relatively large negative values of fluid pressure (i.e., suction) in a vicinity of the hydrofracture tip due to the presence of a singularity in the pressure field [56]. Estimates in practical hydraulic fracture treatments with large solid toughness show that the fluid-lag zone is in fact of very small size [57]. The common practice in many hydraulic fracturing simulations has been to consider the fluid vapour pressure as a cut-off value of the solution obtained using a zero-lag assumption, see e.g., [165]. A similar approach was taken in the present work, whereby the fluid vapour pressure is taken to be zero, i.e., negative nodal pressure values obtained from (4.19) are set to zero (see Algorithm 4.1). Nonetheless, it is possible to account for fluid-lag within the present framework, e.g., by taking the "wetted" portion of the cracks as an additional unknown as in [87, 165] or by introducing a nonnegative pressure field constraint as in [151].

Remark 3. *Convergence of the sequential iterative solver.* As mentioned in the introduction, we avoid the complexities associated with the convergence of sequential solution schemes in hydraulic fracturing problems [64, 119] by restricting the simulations presented in Section 4.5 to "toughness dominated" hydraulic fracturing (i.e., relatively large fracture toughness). This allows to focus our attention to the issues caused by lack of time-continuity in previous stress-based methods and to demonstrate the capabilities of the method in modelling multiple hydraulic fractures in naturally fractured media. In addition, adequately small time steps are used ($\Delta t \leq \Delta t_{\text{cr}}$) so that an accurate solution can be obtained in only one passing of block-CD iterations (i.e., $j = 1$ in Algorithm 4.1) in each time increment.

4.5 Numerical simulation results

In this section, we present numerical simulation results in plane strain, which show the robustness and versatility of the proposed hydraulic fracturing computational algorithm. In all simulations, six-noded triangular elements are used and interface elements are inserted everywhere in the mesh as potential sites of crack nucleation and propagation. The numerical integration on the interface elements is performed using a three-point Gauss quadrature

scheme (i.e., three opening displacement nodes per interface element). In addition, linear interpolation is used for the pressure field along each interface element in $\Gamma_{p,h}$. In all simulations, material properties used are Young's modulus $E = 10\text{GPa}$, Poissons ratio $\nu = 0.2$, and material density $\rho = 2500\text{kg/m}^3$. Cohesive fracture model properties used are critical stress $\sigma_c = 1\text{MPa}$, critical opening displacement $\delta_c = 0.1\text{mm}$, and mode-mixity parameter $\beta = 1$. The fracturing fluid is assumed to be water with dynamic viscosity $\mu = 10^{-3}\text{Pa}\cdot\text{s}$ and the coefficient f in equation (4.4) is taken to be 1.05.

In all simulations, it is assumed that the injection pressure p_{inj} is increased from zero to a critical value within a relatively short time so that the hydraulic fracturing process has a duration of approximately 30$\sim$100 milliseconds. Such dynamic loading conditions occur in, e.g., pulsating hydraulic fracturing [71] or dynamic structural failure in gravity dams [145]. Nonetheless, the method and conclusions remain valid for slower loading conditions as well. It is understood that the use of element boundaries as potential crack surfaces introduces a degree of obvious mesh dependence. We have not performed mesh convergence analysis in the simulations presented as this subject has been already addressed in previous chapters.

4.5.1 Effect of time-continuity on stability and robustness

With this example, we examine the effect of time-continuity on the robustness of the hydraulic fracturing simulation algorithm. We show that a numerical solution fails to be obtained with a time-discontinuous extrinsic model of cohesive fracture due to instability of the algorithm. The problem considered is that of a rectangular block of dimensions 10m $\times$ 4m containing a perforation (pre-notch) of length 3m in the middle of its left edge, as shown in Figure 4.4. The fracturing fluid is injected into the perforation with an injection pressure p_{inj} increased linearly from 0 to 1.0MPa in 100ms. The FE mesh used in the simulations, also shown in Figure 4.4, contains 7140 elements and 42840 (7140×6) nodal points.

The problem was solved with the present time-continuous algorithm and a time-discontinuous algorithm which is in essence similar except that the mechanical update step, which concerns deformation and fracture of the body, is replaced by a time-discontinuous, hybrid DG-cohesive element method similar to [129]. In the hybrid DG-cohesive element algorithm, the DG method is used to tie together the element edges prior to the nucleation of cracks. Upon satisfaction of an extrinsic fracturing criterion, the DG terms cease to operate and give place to the tractions computed from a cohesive traction-separation model. Fluid pressure is incorporated in the equilibrium equations of the fractured body as an external force applied on the fully-cracked interface elements of the mesh. The

time-discontinuous method cannot be used with implicit time-stepping due to the interference of the above interface activation criteria with the iterations [73]. Thus, both of the simulations were performed explicitly with $\Delta t = 0.8\Delta t_{\text{cr}}$.

Figure 4.5 shows velocity contours in a vicinity of the hydro-fracture obtained by the proposed method and by the hybrid DG-cohesive element method at a hydro-fracture propagation length of approximately 0.6m. In addition, Figure 4.6 shows time histories of the opening velocity of the hydro-fracture mouth (i.e., point A in Figure 4.4) obtained by the two methods. The time-discontinuous model (hybrid DG-cohesive element) exhibits nonphysical, spurious oscillations in both space and time. This is typically observed behaviour of time-discontinuous models and it emanates from the formation of unphysical shocks in the body at crack nucleation due to discontinuity of the force vector. Because the mass balance equation (4.9) is dependent on the normal crack opening velocity field $[\![\dot{u}_n]\!]$, unphysical solutions are obtained for the fluid pressure field exhibiting extremely large values (i.e., high gradients) with spurious oscillations in time. These pathological behaviours eventually lead to instability of the algorithm and failure to obtain a solution in subsequent time steps because the elements on the two sides of the hydro-fracture become extremely distorted by the applied pressures.

In contrast to the time-discontinuous model, no sign of instability was observed in solutions obtained with the proposed time-continuous algorithm. The final hydro-fracture trajectory together with the distribution of the pressure field obtained are shown in Figure 4.7 (negative pressure values in the fluid-lag zone are removed from the profile of the fluid pressure distribution). In addition, Figure 4.8 shows the time history of the crack-tip velocity. The hydro-fracture initiates from the perforation tip at $t = 11.5$ms and branches into two tips at $t = 20.3$ms after it has propagated for approximately 1.65m.

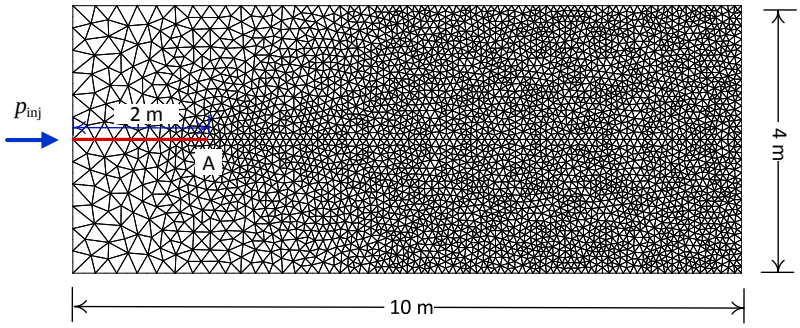

Figure 4.4: Hydro-fracture propagation in a rectangular domain; problem definition, boundary conditions and FE mesh

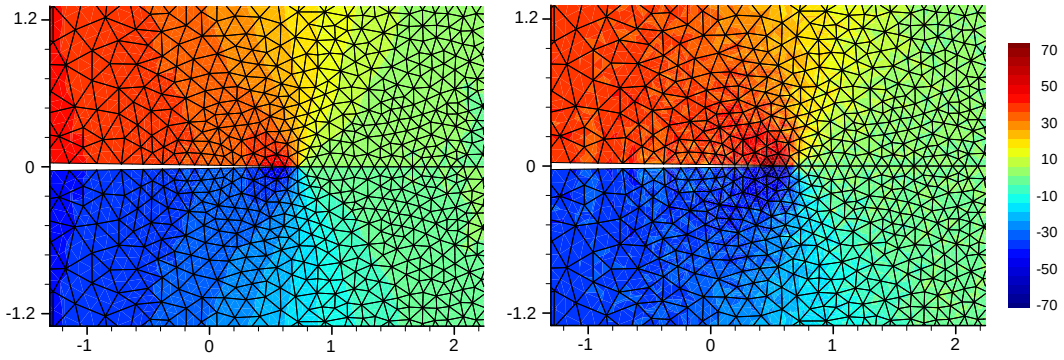

Figure 4.5: Contours of the vertical component of the velocity field $\dot{u}_y$ (color bar in mm/s) obtained with a) the time-continuous coupled block-CD algorithm and b) the time-discontinuous hybrid DG-cohesive element method. Deformation magnified 100 times. Dimensions in m

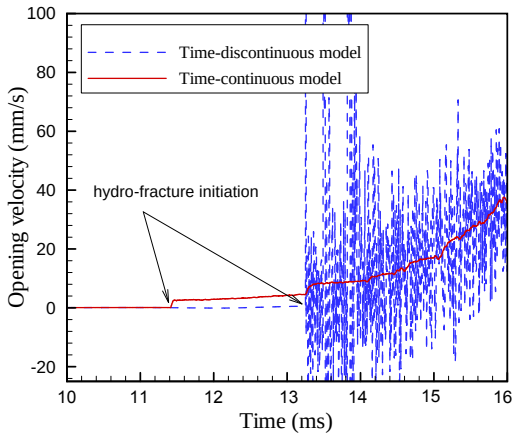

Figure 4.6: Time histories of the hydro-fracture mouth opening velocity obtained by the time-continuous (coupled block-CD) and time-discontinuous (hybrid DG-cohesive element) methods in $10 < t < 16$ ms

The branching of the hydro-fracture tip allows the deformable block to dissipate excessive input energy under the dynamic loading conditions [47]. The maximum crack propagation velocity attained is estimated to be $0.4v_R \simeq 480$ m/s, where v_R is the Rayleigh wave speed in the material which is approximated as $v_R \simeq 1200$m/s [59]. The upper and lower tips propagate symmetrically and eventually reach the boundaries of the domain at

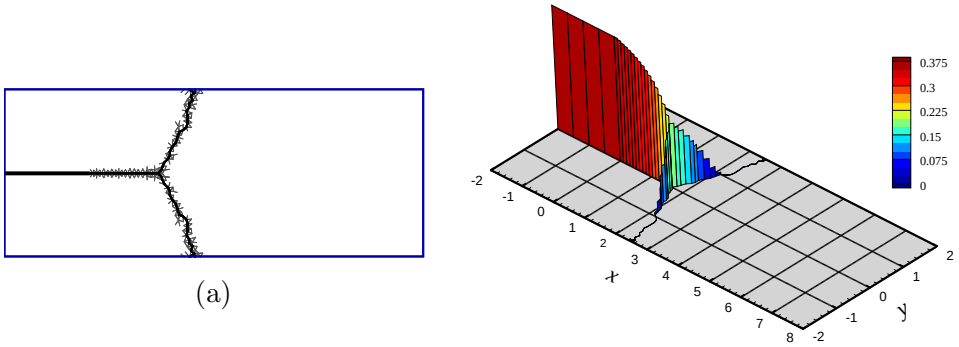

(a) (b)

Figure 4.7: a) Crack propagation trajectory and b) profile of the fracturing fluid pressure (colour bar in MPa) obtained for hydro-fracture propagation in a rectangular block at $t = 35.8$ms

$t = 35.8$ms. The overall response of the hydraulically driven crack agrees well with the expected behaviour known from theoretical and experimental findings in previous dynamic fracture literature [130, 149]. In addition, we performed a temporal convergence study by solving the hydraulic fracturing problem with different time step sizes $\Delta t_i = 0.8\Delta t_{\text{cr}}/2^i$ s, $i = 0 : 4$. The normalized error in the velocity and pressure fields obtained with time step Δt_i is defined as $e_u = \|\dot{\mathbf{U}}_i - \dot{\mathbf{U}}_{\text{exact}}\|/\|\dot{\mathbf{U}}_{\text{exact}}\|$ and $e_p = \|\mathbf{P}_i - \mathbf{P}_{\text{exact}}\|/\|\mathbf{P}_{\text{exact}}\|$, respectively, in which the solution obtained from the finest time step size ($i = 4$) is taken to be the exact solution (denoted by the subscript "exact"). Results of the temporal convergence study obtained at hydro-fracture propagation length of approximately 0.5m are shown in Figure 4.9. Convergent behaviour is observed, indicative of the numerical soundness of the computational algorithm. Similar results could also be obtained with the implicit time-stepping scheme which are, however, not shown here for the brevity of the presentation.

4.5.2 Simultaneous hydro-fracture growth in an intact domain

The simultaneous growth of hydro-fractures has been analyzed previousely by Pierce and Bunger [124] and Vahab and Kalili [164], among many others. It has been shown that, in a uniformly spaced cluster of initial perforations, the so called stress shadowing effect leads to the arrest of hydro-fracture growth from the middle perforations whereas hydro-fractures propagate from the outer perforations in a diverging fashion. In this example, we verify the predictive capabilities of the proposed method by simulating an example of

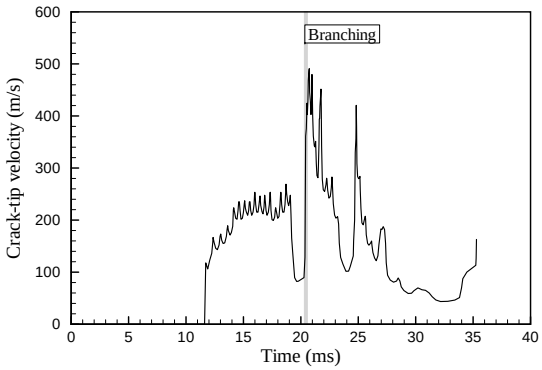

Figure 4.8: Time history of the crack-tip velocity. After branching, the reported crack-tip velocity is that of the upper branch. The velocity was obtained from the crack length vs. time curve produced by considering only the time steps at which crack propagation occurs

simultaneous hydro-fracture growth from multiple perforations.

A 10m×10m square block is considered in plane strain with traction free boundaries. The block contains three perforations of length 0.5m at its left edge with lateral spacing of 1.0m. The three perforations are subjected to fracturing fluid pressure p_{inj} which is increased linearly from zero to 1.5MPa in 50ms. The time stepping is performed implicitly using $\Delta t = 0.99\Delta t_{\text{cr}}$. The FE mesh used in the analyses consists of 6593 triangular elements and 39558 nodal points. The mesh is more refined in an area ahead of the perforation tips for better resolution of crack trajectories. Figure 4.10 shows the problem definition and the FE mesh.

The hydro-fracture trajectories along with the contours of maximum principal stress σ_1 obtained at different instants of the simulation are shown in Figure 4.11. In addition, the profile of the fracturing fluid pressure along the hydro-fractures obtained at the end of the simulation is shown in Figure 4.12. The hydro-fractures are propagated from the off-center perforations only and little crack propagation occurs from the middle perforation tip. In addition, the hydro-fracture tips propagate symmetrically in a diverging fashion. Note that the stress shadowing effect is apparent in the contours of the maximum principal stress (Figure 4.11b). The stress field ahead of all perforation tips is tensile at early stages of the simulation. As the off-centre hydro-fractures grow, tensile stresses reduce significantly at the middle perforation tip and eventually become compressive, suppressing further hydro-fracture propagation. The numerical results obtained are in overall agreement with the expected behaviour known from previous literature [124, 24, 164].

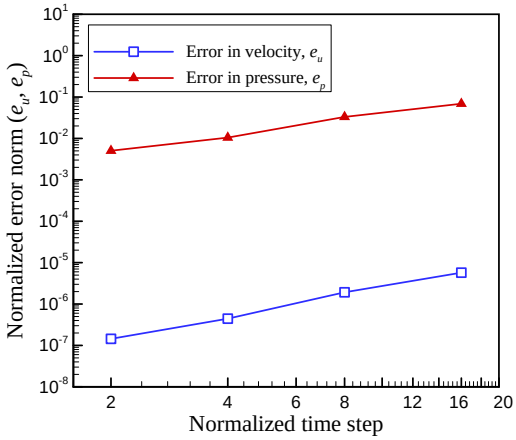

Figure 4.9: Temporal convergence in velocity and pressure error norms for the hydro-fracture propagation in a rectangular domain. The asymptotic rate of convergence is estimated to be approximately 1.93 in the velocity error norm and 1.28 in the pressure error norm

4.5.3 Hydraulic fracturing in a cemented naturally fractured domain

We consider again a 10m×10m square block in plane strain with traction free boundaries. The block is subjected to fluid injection from a perforation of initial length 0.5m which is located at the middle of the left edge of the block. To mimic the conditions in reservoirs with bedding planes and weak interfaces, the domain contains 20 uniformly-spaced naturally-cemented fractures, each of length $\sqrt{2}$m and oriented at an angle of 45° with respect to the horizontal. These naturally-cemented fractures are assumed to have different fracture properties from the medium surrounding them. We take the strength of the natural fractures to be $\alpha\sigma_c$, where σ_c is the cohesive strength of the domain, and analyze two cases $\alpha = 0.1$ and $\alpha = 0.5$. In both cases, the critical opening displacement δ_c is taken to be the same as that of the rest of the domain. The injection pressure p_{inj} is increased linearly from zero to 1.5MPa in 50ms. The problem definition and the FE mesh used in the simulations are shown in Figure 4.13.

The hydro-fracture propagation trajectories obtained with the two natural fracture strengths are shown in Figure 4.14 at different instants during the solution. Figure 4.15 shows the final deformed geometries together with contours of the principal stress σ_1 obtained at the end of the simulation. In the case $\alpha = 0.1$, propagation of the hydro-fracture activates the cemented discontinuities away from the pressurized hydro-fractures as they

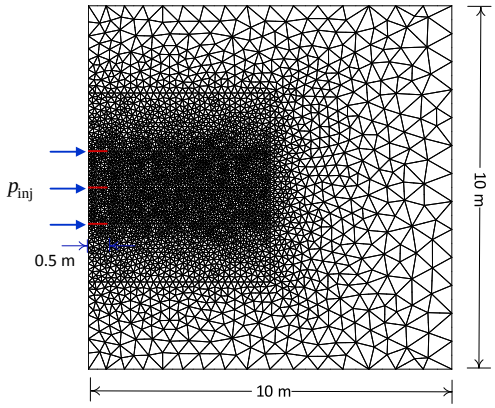

Figure 4.10: Simultaneous hydro-fracture growth in an intact domain; problem definition and FE mesh

have little strength compared to the rest of the domain. It is observed that the hydraulically driven cracks generally tend to deflect toward a direction normal to the pre-existing interfaces. In the case $\alpha = 0.5$, on the other hand, little fracture activation occurs away from the fracturing zone and a different propagation path is obtained compared to the one when $\alpha = 0.1$. Results obtained clearly indicate the capabilities of the proposed method in handling different interaction scenarios such as activation of natural faults, coalescence of discontinuities in the domain and offset crack propagation.

Furthermore, Figure 4.16 shows the time histories of the total hydro-fracture length (i.e., the length of pressurized interfaces $\Gamma_{p,h}$) obtained with the two natural fracture strengths. The final length of the induced network of hydro-fractures is approximately 30% larger for $\alpha = 0.1$. This is in accordance with previously reported observations that hydraulic fracturing treatments in formations with strongly bonded natural discontinuities require higher injection pressures [159].

It is worth noting that the hydro-fracture lengths show a step-wise evolution as can be seen in Figure 4.16. This type of behaviour is in agreement with experimental observations and field data [27]. Schrefler and coworkers pointed out that to capture such nonsmooth behaviour, the model must include dynamics [26] and put no restriction on crack velocity, i.e., be free of pre-determined crack increment lengths [126]. The majority of numerical hydraulic fracturing models fail to capture such nonsmooth behaviour [126].

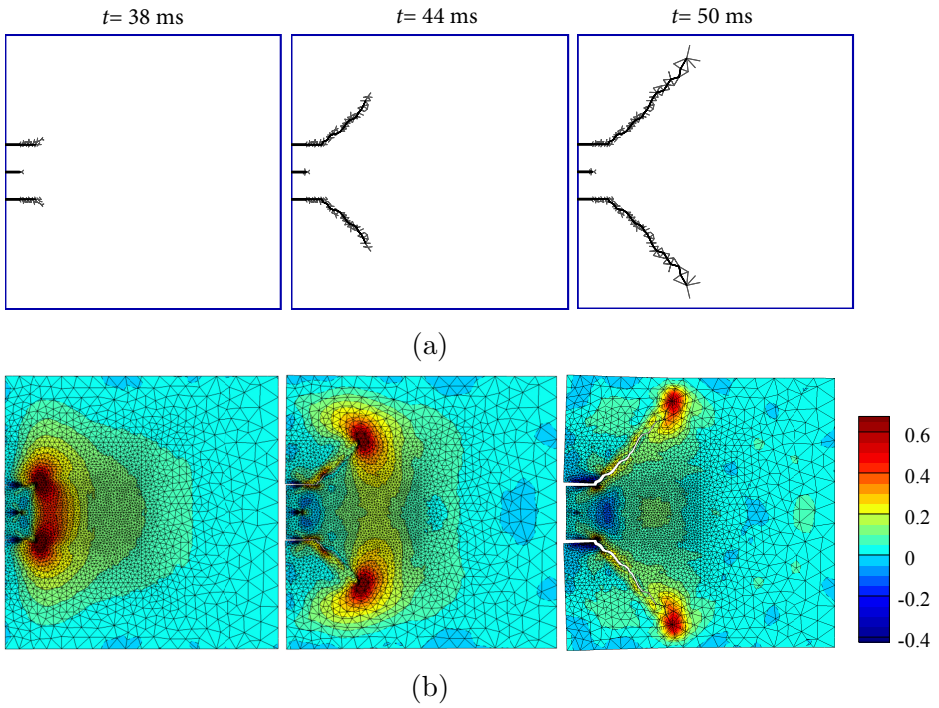

Figure 4.11: Simultaneous hydro-fracture growth in an intact domain; a) hydro-fracture growth trajectories, b) contours of maximum principal stress

4.5.4 Multiple hydro-fracture growth in a heavily fractured domain

Nearly all geological formations heavily bear natural discontinuities and fractures. Hydraulic fracturing in such formations has been studied numerically using a variety of algorithms, e.g., [85, 112]. In this final example, we further demonstrate the capabilities of the method by modelling an example of hydraulically driven fracture networks in a heavily fractured domain. As shown in Figure 4.17, the 10m×10m domain considered has traction-free boundaries and is populated by one hundred randomly oriented pre-existing fractures that have zero strength in both tension and shear. The lengths of the pre-existing fractures were sampled from a normal distribution with a mean value of 0.5m and standard deviation of 12.5cm. A trial and error scheme was implemented to ensure that all fractures have a minimum center-to-center distance of 0.75m from each other. The fluid is injected into the domain through four perforations of initial length 0.25m oriented at 0°, 90°, 180° and 270° with respect to the horizontal in a wellbore of diameter 0.5m located at the center

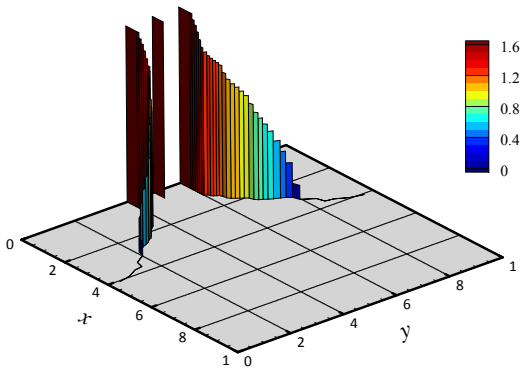

Figure 4.12: Profile of the fracturing fluid pressure (colour bar in MPa) obtained for simultaneous hydraulic fracturing in a square block at $t = 50$ ms. Dimensions in m

of the domain. The injection pressure p_{inj} is increased linearly from zero to 2.25MPa in 50ms.

The evolution of the discontinuities in the domain during the hydraulic fracturing process is shown in Figure 4.18. As can be observed, hydraulic fracture propagation starts from the bottom perforation tip earlier than from the other three perforations. This is due to the heterogeneity induced by the pre-existing fractures, which leads to delayed attainment of the critical stress at the right, top and left perforation tips (i.e., those oriented at 0°, 90° and 180°, respectively). In subsequent time steps, however, the hydro-fracture initiated from the top perforation propagates at a higher speed compared to the other hydro-fractures in the domain. This is a result of the complex interaction between pre-existing and evolving discontinuities which cannot be predicted unless the effect of pre-existing discontinuities is explicitly taken into account. The simulation was terminated at $t = 47$ms, as soon as the top hydro-fracture reached the top boundary of the domain. In addition, it is observed that the hydro-fractures initiated from the right and left perforations deflect downward, away from the hydro-fracture initiated from the top perforation. This is similar to the behaviour observed in the multi-zone hydraulic fracturing example in Section 4.5.2, in which multiple hydraulically driven fractures propagate in a diverging fashion.

Figures 4.19a and 4.19b respectively show the deformed geometry of the fractured body and the distribution of the pressure field in $\Gamma_{p,h}$ obtained at the end of the simulation. The distribution of the fluid pressure field shows that several of the pre-existing cracks are subjected to the fracturing fluid pressure as they become part of $\Gamma_{p,h}$ upon coalescence of propagating hydro-fractures with these pre-existing cracks. We note that the zero pressure values obtained in the left and bottom hydro-fracture branches are not a result of fluid-lag

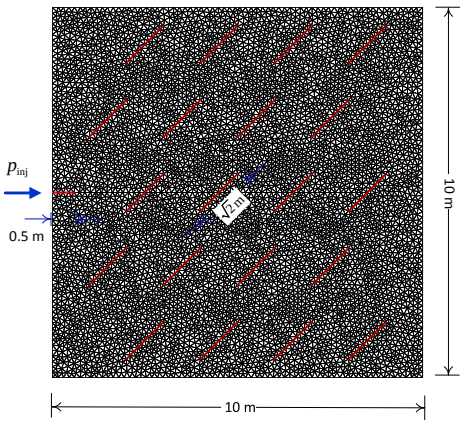

Figure 4.13: Hydraulic fracturing in a naturally-fractured block. The FE mesh consists of 12983 6-noded triangular elements and 77898 nodal points

but are due to the closure of crack faces (i.e., contact condition) at points A and B (see Figures), which occurs during the hydraulic fracturing process and blocks the flow of the fracturing fluid beyond these points. Notably, the crack faces are in contact at points A and B from the moment of crack initiation at these points. To model the blockage of fluid flow due to such conditions, a zero pressure constraint was imposed on the solution of the flow continuity equation (4.19) at those nodal points in $\Gamma_{p,h}$ that were *disconnected* from the injection points (perforations) due to crack closure at A and B. The points A and B remain in contact through the entire course of the hydraulic fracturing process, thus the above constraint was kept active until the end of the simulation.

4.6 Conclusion

A computational algorithm was presented for the simulation of hydraulic fracturing in naturally fractured media. The method offers desirable flexibility in handling the interaction between multiple evolving fractures in the body. The set of coupled hydro-mechanical equations are solved using an iterative solution strategy in which the mechanical and hydraulic unknowns are updated sequentially, in a decoupled manner until convergence is achieved. The set of pressurized cracked interfaces, i.e., those connected to the injection point through a network of interconnected cracked interfaces, was determined using a search algorithm that relies on principles of Graph theory.

It was shown through numerical simulations that the use of the time-continuous, non-

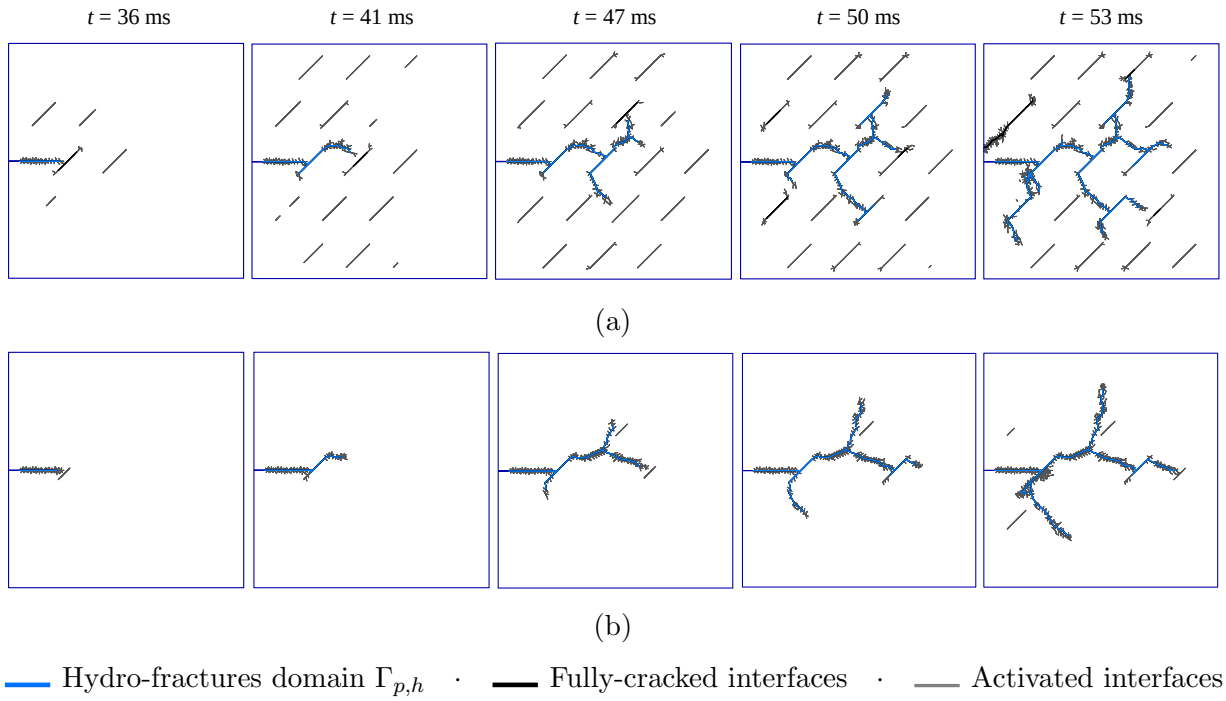

Figure 4.14: Hydraulic fracture trajectories obtained for hydro-fracture propagation in cemented naturally fractured block; a) $\alpha = 0.1$, b) $\alpha = 0.5$, where α is the ratio of the fracture strength of the pre-existing fractures over that of the domain

differentiable energy minimization model of fracture is essential for the stability (i.e., ability to obtain a solution) and robustness (i.e., satisfactory convergence rates with time step refinement) of the hydraulic fracture propagation algorithm. Because time-discontinuous models lead to nonphysical velocity fields, robustness of the solution obtained for the fracturing pressure field is lost given that the mass balance equation defined locally along the cracks is dependent on the crack opening velocity field. One expects that a similar behaviour would be observed in any multi-physics problem with local interfacial fields dependent on crack opening velocities. Further numerical results were presented to show the capabilities of the proposed algorithm in modeling simultaneous hydro-fracture growth as well as fracking in naturally fractured media.

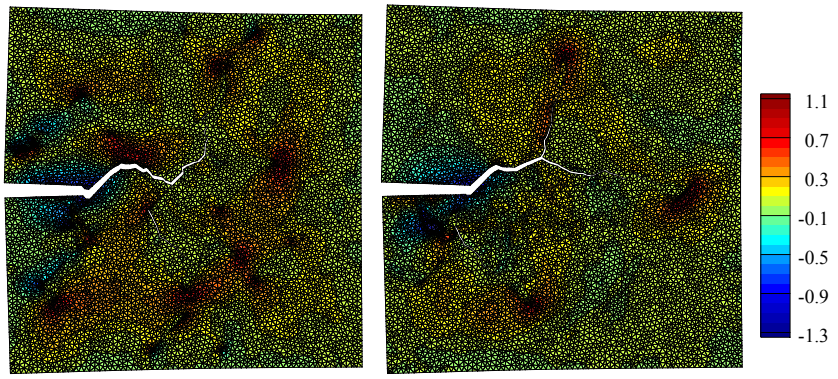

(a) (b)

Figure 4.15: Contours of the maximum principal stress (colour bar in MPa) obtained at the end of the simulation for hydro-fracture propagation in naturally-fractured block; a) $\alpha = 0.1$, b) $\alpha = 0.5$. Deformation magnified 50 times in both cases

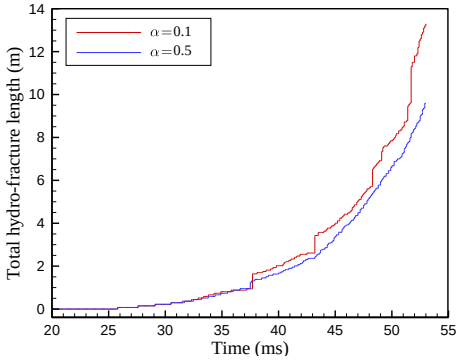

Figure 4.16: Time histories of the total hydro-fracture length obtained with $\alpha = 0.1$ and $\alpha = 0.5$ for hydraulic fracturing in a cemented naturally fractured domain. The bigger "steps" in the the evolution of hydro-fracture lengths correspond to time steps at which the hydro-fractures merge with pre-existing weak surfaces

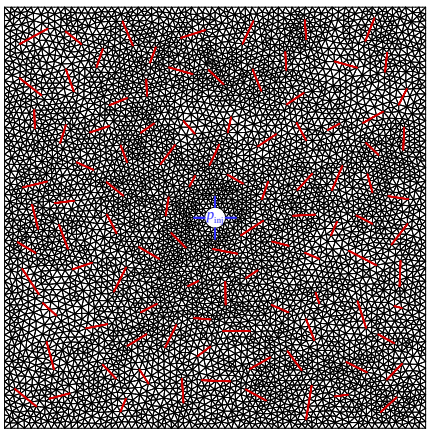

Figure 4.17: Multi-zone hydraulic fracturing in a heavily fractured square domain. The FE mesh used in the computations consists of 11468 triangular elements and 68808 nodal points

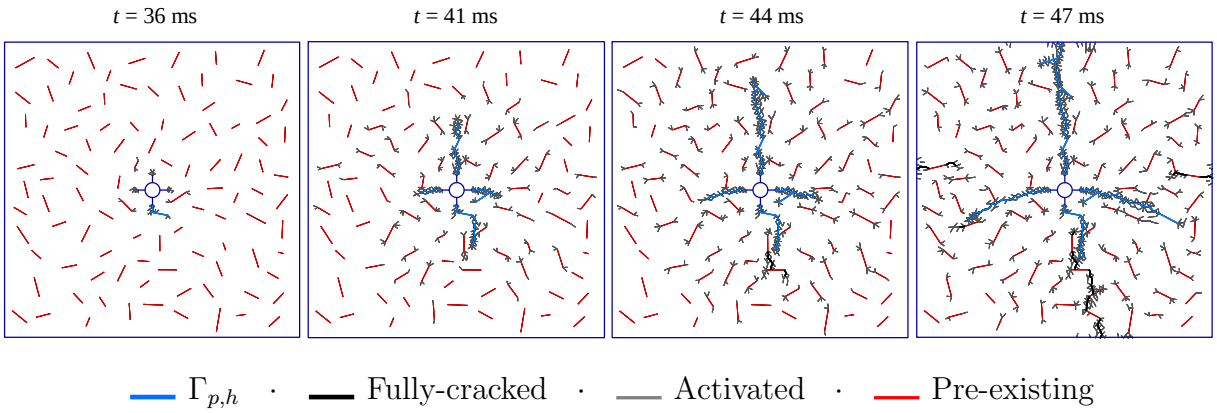

Figure 4.18: Evolution of discontinuities in multi-zone hydraulic fracturing of a heavily fractured square domain

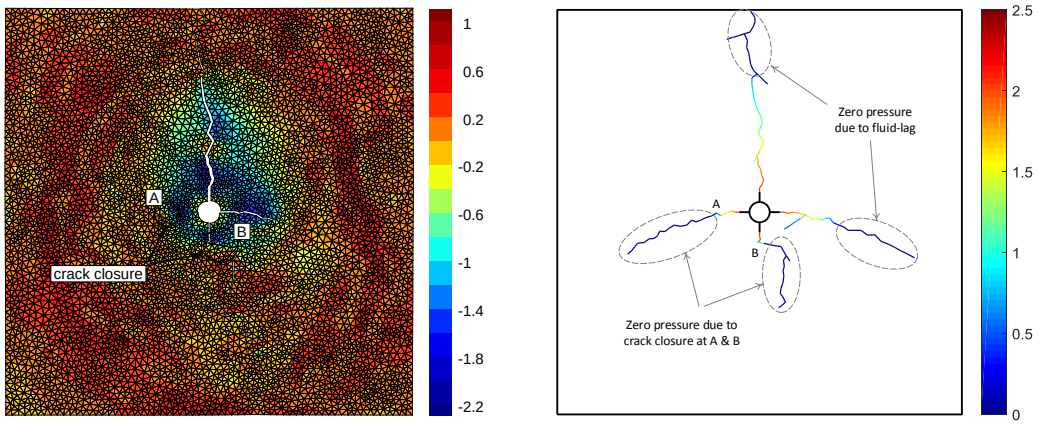

(a) (b)

Figure 4.19: Multi-zone hydraulic fracturing in a heavily fractured square domain; a) final deformed configuration (magnified 50 times) and contours of the maximum principal stress σ_1, b) final distribution of the fluid pressure field in $\Gamma_{p,h}$. Color bar in MPa

Chapter 5

Conclusions and future work

5.1 Summary

Numerical simulation of fracture is an indispensable tool, not only for predicting failure of structures across engineering disciplines, but also for studying mechanisms involved in the fracturing process. Despite the large body of work in discrete crack modelling, most previous method suffer from numerical issues, several of which, as this thesis showed, due to time-discontinuity of the extrinsic cohesive model, leading to lack of convergence of numerical solutions and nonphysical simulations. In particular, existing methods have been mostly limited to explicit time-stepping. Implicit schemes, suited for low-velocity and quasi-static problems, are not well represented in the current literature.

The central idea of this research has thus been to develop robust and mathematically sound computational models that are free from the issues mentioned above. In doing so, several computational algorithms were proposed for the numerical implementation of the nondifferentiable energy minimization approach to cohesive fracture. The key feature of all algorithms proposed is the lack of a stress criterion for activation of cracks. This enables the algorithms to overcome difficulties associated with time-discontinuity. The methods allow for a seamless transition from the uncracked to the cracked state, making possible the use of iterative solvers with implicit time-stepping. A critical component of this work was a strong effort to validate the robustness of the proposed computational frameworks. This was done through performing time step and mesh size convergence studies, qualitative and quantitative comparison of simulations with experimental observations and theoretical findings, and application of the methods to multi-physics problems.

In Chapter 2, a discontinuous Galerkin implementation of the nondifferentiable energy minimization approach to cohesive fracture was introduced in which all element edges are potential sites of cracks. The nondifferentiability was treated using a continuation algorithm on the basis of successive smoothing of the interface potential, an idea originally introduced in [116]. The smooth problems were solved using a trust region method capable of handling the nonconvex objective function. The DG method improves the computational efficiency of the algorithm by eliminating Lagrange multiplier unknowns. Implicit time-stepping was performed using the well-known generalized Newmark scheme [104] for which a proper dynamic potential was also introduced. The temporal convergence tests and the smoothness of velocity contours confirmed that the nondifferentiable energy minimization approach to cohesive fracture completely bypasses the time-discontinuity issue. In addition, a mesh refinement study was performed to show that the method preserves consistency and stability of the finite element formulation in both pre- and post-failure conditions. Various examples confirmed the capabilities of the method to model quasistatic to truly dynamic crack propagation. In addition, the numerical framework was validated by comparing

simulations with experiments. These included load-displacement curves and crack paths in a quasi-static three-point bending beam and the crack path and crack nucleation time in a low-velocity impact of a compact-compression specimen.

In chapter 3, a block coordinate descent algorithm was proposed for nondifferentiable energy minimization within the DG framework proposed in Chapter 2. In each of its iterations, the algorithm obtains crack opening displacements by solving a small nondifferentiable minimization problem at each interface Gauss point using generalized differential calculus. These crack openings are then enforced on the deformation of the finite element mesh when solving the global equilibrium equations. This makes the method extremely easy to incorporate into standard finite element codes. In addition, a distinct advantage of the method is that it allows for both explicit and implicit time integration schemes. It was shown that even though convexity in this context is not a requirement for convergence of the iterations, it is equivalent to a minimum CPZ resolution criterion, known empirically in the previous literature as a requirement for capturing correctly the amount of dissipated fracture energy. The block-CD algorithm appears to be best suited for dynamic applications as the number of iterations required for convergence can be exorbitant when time steps are large. Several mesh convergence studies were presented to show that the method produces convergent dissipated fracture energies. Numerical crack velocities remained well below the Rayleigh wave speed and the crack bifurcated at approximately $0.6v_R$ when analyzing a dynamic crack branching instability.

In Chapter 4, a hydro-mechanical model and computational algorithm was presented for hydraulic fracturing in impermeable media on the basis of the block-CD algorithm proposed in Chapter 3. The hydro-mechanical model is based on nondifferentiable energy minimization for deformation and fracture of the solid body coupled with mass balance of the fracturing fluid within the cracks. Because the mass balance equation is dependent on the crack opening velocity field, time-discontinuous models give rise to spurious solutions for the coupled fluid pressure field defined locally along the crack faces. It was shown that these spurious solutions can eventually lead to instability of the computational algorithm in these models. Thus, this work exemplifies the pivotal role of time-continuity in modelling multi-physics problems. In addition, an algorithm was proposed on the basis of graph theory to identify the set of pressurized cracks within the domain. This extends the applicability of the method to multiple hydraulically driven fracture networks in naturally fractured media, a quality that is generally hard to achieve in other simulation techniques, including XFEM.

5.2 List of publications and presentations

5.2.1 Journal papers

Outcomes of this research were published/submitted for publication in peer-reviewed journals. These articles are listed below:

- **Hirmand MR** and Papoulia KD, A continuation method for rigid-cohesive fracture in a discontinuous Galerkin finite element setting. *International Journal for Numerical Methods in Engineering*, (2018) 115:627650
- **Hirmand MR** and Papoulia KD, Block coordinate descent energy minimization for dynamic cohesive fracture. *Computer Methods in Applied Mechanics and Engineering*, in review (2019), Manuscript ID: CMAME-D-18-01800
- **Hirmand MR**, Vahab M, Papoulia KD, Khalili N, Robust simulation of hydraulically driven fracture networks in naturally fractured impermeable media. *Computer Methods in Applied Mechanics and Engineering*, in revision (2019), Manuscript ID: CMAME-D-19-00248
- Vavasis S, Papoulia KD, **Hirmand MR**, A second-order cone interior-point method for initially rigid cohesive fracture. *Computer Methods in Applied Mechanics and Engineering*, in revision (2019), Manuscript ID: CMAME-D-18-01856

5.2.2 Conference presentations

Outcomes of this research were also presented at the following conferences:

- **Hirmand MR**, Papoulia KD, Discontinuous Galerkin formulation with Nitsche flux for cohesive fracture simulations. *Keynote presentation in the VII European Congress on Computational Methods in Applied Sciences and Engineering (ECCOMAS 2016)*, Crete, Greece. June 5-10, 2016
- Papoulia KD, **Hirmand MR**, Vavasis S, nondifferentiable energy minimization for cohesive fracture. *24th International Congress of Theoretical and Applied Mechanics (ICTAM 2016)*, Montreal, Canada. August 21-26, 2016

- **Hirmand MR**, Papoulia KD, nondifferentiable energy minimization with Nitsche flux for time-continuous cohesive fracture. *14th U.S. National Congress on Computational Mechanics (USNCCM14)*, Montreal, Canada. July 17-20, 2017

- **Hirmand MR**, Papoulia KD, Explicit nondifferentiable energy minimization for dynamic cohesive fracture propagation, *13th World Congress on Computational Mechanics and 2nd Pan American Congress on Computational Mechanics (WCCM XIII and PANACM II)*, New York, USA. July 22-27, 2018

- Vavasis S, Papoulia KD, **Hirmand MR**, A second-order cone interior-point method for initially rigid cohesive fracture, *13th World Congress on Computational Mechanics and 2nd Pan American Congress on Computational Mechanics (WWCCM XIII and PANACM II)*, New York, USA. July 22-27, 2018

5.2.3 Industry presentations

This research was funded in part by NSERC-CRD project COMP410-CRIAQ.[1] Methods proposed in this research along with numerical simulations of matrix and fiber cracking in composite components were presented to the industrial and academic partners of the project in a number of group meetings and seminars. The presentations delivered are listed below.

- State-of-the-art of cohesive zone modelling, University of Laval, Quebec City, September 2015

- Towards a robust approach to dynamic crack propagation simulation, Bombardier Aerospace BAN3, Montreal, April 2016

- A robust approach to dynamic crack propagation with special reference to multi-scale modelling of composites, Webex video-conference, October 2016

- nondifferentiable energy minimization for cohesive crack propagation simulations, Bombardier Aerospace BAN3, Montreal, April 2017

- Simulation of cohesive fracture propagation in composite materials, Webex video-conference, February 2018

[1] Industrial partner CRIAQ, Consortium de Recherche et dInnovation en Arospatiale au Qubec

- Modelling delamination and matrix cracking in aerospace components, Bell Helicopter Textron Canada, Montreal, May 2018
- Dynamic crack propagation and progressive failure analysis in woven composite aircraft structures, Webex video-conference, December 2018

5.3 Recommendations for future work

Some of the research directions that can be pursued in future efforts are suggested below:

1) It is intuitive that material failure is a continuous process that involves different forms of degradation, depending on the material, before a dominant crack forms. That is, localization of damage leads to the formation of a dominant crack in a seamless manner. The nondifferentiable energy minimization algorithms proposed in this research describe cracks as discrete discontinuities. The phase field approach and other continuum damage mechanics models, on the other hand, rely entirely on a smeared damage approach. Both of the methods are unable to describe the transition from distributed damage to the formation of dominant cracks. For the reasons explained in this research, however - notably lack of an activation criterion - nondifferentiable energy minimization algorithms are well positioned to make this type of analysis possible. This would be a major break-through in failure analysis. An interesting topic future research would be developing a numerical frameworks that can bring us closer to this goal.

2) In the present research, potential crack paths were *a priori* limited to the set of inter-element boundaries of the finite element mesh. This is not a mandatory requirement of the methods but a choice for convenience of the finite element implementation. The nondifferential energy minimization approach to cohesive fracture can be generalized by viewing the orientation of the cracks (or the finite element triangulation itself) as an additional unknown field in the context of energy minimization. In that case, the zero displacement jump condition prior to crack nucleation may be enforced "strongly" via a continuous finite element approximation. Interface elements (or enrichment degrees of freedom in an XFEM setting) can then be inserted adaptively to introduce the cracks.

3) Interface potentials used in this research were taken to be of the form proposed by Ortiz and Pandolfi [113], in which the potential is made a function of a norm of crack opening displacements (see Section 3.2.1, for example). This type of cohesive potential is best suited for modelling generalized fracture in homogeneous materials. In the case of an inhomogeneous material with different fracture responses in different directions, such as fiber-reinforced composites, the predictive capabilities of this model may be diminished. A

valuable contribution would thus be developing interface potentials with higher predictive capabilities for inhomogeneous material such as composites.

4) Extending the current two-dimensional computer code to three-dimensional would be a valuable contribution that makes the analysis of real-world applications possible. Implementing parallelized computer program that can handle the increasing computational costs of such simulations can significantly facilities this task.

Bibliography

[1] Reza Abedi, Morgan A Hawker, Robert B Haber, and Karel Matouš. An adaptive spacetime discontinuous galerkin method for cohesive models of elastodynamic fracture. *International Journal for Numerical Methods in Engineering*, 81(10):1207–1241, 2010.

[2] J Adachi, E Siebrits, A Peirce, and J Desroches. Computer simulation of hydraulic fractures. *International Journal of Rock Mechanics and Mining Sciences*, 44(5):739–757, 2007.

[3] Ted L Anderson. *Fracture mechanics: fundamentals and applications*. CRC press, 2017.

[4] P Areias, T Rabczuk, and PP Camanho. Initially rigid cohesive laws and fracture based on edge rotations. *Computational Mechanics*, 52(4):931–947, 2013.

[5] Pedro MA Areias and Ted Belytschko. Analysis of three-dimensional crack initiation and propagation using the extended finite element method. *International Journal for Numerical Methods in Engineering*, 63(5):760–788, 2005.

[6] Pedro MA Areias and Timon Rabczuk. Quasi-static crack propagation in plane and plate structures using set-valued traction-separation laws. *International Journal for Numerical Methods in Engineering*, 74(3):475–505, 2008.

[7] Francisco Armero and Christian Linder. New finite elements with embedded strong discontinuities in the finite deformation range. *Computer Methods in Applied Mechanics and Engineering*, 197(33-40):3138–3170, 2008.

[8] Francisco Armero and Christian Linder. Numerical simulation of dynamic fracture using finite elements with embedded discontinuities. *International Journal of Fracture*, 160(2):119, 2009.

[9] Douglas N Arnold. An interior penalty finite element method with discontinuous elements. *SIAM journal on numerical analysis*, 19(4):742–760, 1982.

[10] Ivo Babuška. The finite element method with penalty. *Mathematics of Computation*, 27(122):221–228, 1973.

[11] Grigory I Barenblatt. The formation of equilibrium cracks during brittle fracture. General ideas and hypotheses. Axially-symmetric cracks. *Journal of Applied Mathematics and Mechanics*, 23(3):622–636, 1959.

[12] Zdenek P Bazant and Jaime Planas. *Fracture and size effect in concrete and other quasibrittle materials*, volume 16. CRC press, 1997.

[13] Ted Belytschko, Hao Chen, Jingxiao Xu, and Goangseup Zi. Dynamic crack propagation based on loss of hyperbolicity and a new discontinuous enrichment. *International Journal for Numerical Methods in Engineering*, 58(12):1873–1905, 2003.

[14] Dimitri P Bertsekas. Nondifferentiable optimization via approximation. In *Nondifferentiable optimization*, pages 1–25. Springer, 1975.

[15] Dimitri P Bertsekas. *Nonlinear programming*. Athena scientific Belmont, 1999.

[16] Florin Bobaru and Guanfeng Zhang. Why do cracks branch? a peridynamic investigation of dynamic brittle fracture. *International Journal of Fracture*, 196(1-2):59–98, 2015.

[17] Thomas J Boone and Anthony R Ingraffea. A numerical procedure for simulation of hydraulically-driven fracture propagation in poroelastic media. *International Journal for Numerical and Analytical Methods in Geomechanics*, 14(1):27–47, 1990.

[18] Michael J Borden, Clemens V Verhoosel, Michael A Scott, Thomas JR Hughes, and Chad M Landis. A phase-field description of dynamic brittle fracture. *Computer Methods in Applied Mechanics and Engineering*, 217:77–95, 2012.

[19] Ronaldo I Borja. A finite element model for strain localization analysis of strongly discontinuous fields based on standard galerkin approximation. *Computer Methods in Applied Mechanics and Engineering*, 190(11-12):1529–1549, 2000.

[20] Blaise Bourdin, Gilles A Francfort, and Jean-Jacques Marigo. Numerical experiments in revisited brittle fracture. *Journal of the Mechanics and Physics of Solids*, 48(4):797–826, 2000.

[21] Blaise Bourdin, Gilles A Francfort, and Jean-Jacques Marigo. The variational approach to fracture. *Journal of Elasticity*, 91(1-3):5–148, 2008.

[22] Joseph K Bradley, Aapo Kyrola, Danny Bickson, and Carlos Guestrin. Parallel coordinate descent for L_1-regularized loss minimization. *arXiv preprint arXiv:1105.5379*, 2011.

[23] Franco Brezzi and Michel Fortin. *Mixed and hybrid finite element methods*, volume 15. Springer Science & Business Media, 2012.

[24] Andrew P Bunger, Xi Zhang, Robert G Jeffrey, et al. Parameters affecting the interaction among closely spaced hydraulic fractures. *SPE Journal*, 17(01):292–306, 2012.

[25] Godofredo T Camacho and M Ortiz. Computational modelling of impact damage in brittle materials. *International Journal of Solids and Structures*, 33(20-22):2899–2938, 1996.

[26] Toan D Cao, Fazle Hussain, and Bernhard A Schrefler. Porous media fracturing dynamics: stepwise crack advancement and fluid pressure oscillations. *Journal of the Mechanics and Physics of Solids*, 111:113–133, 2018.

[27] Toan Duc Cao, Enrico Milanese, Ernst W Remij, Paolo Rizzato, Joris JC Remmers, Luciano Simoni, Jacques M Huyghe, Fazle Hussain, and Bernhard A Schrefler. Interaction between crack-tip advancement and fluid flow in fracturing saturated porous media. *Mechanics Research Communications*, 80:24–37, 2017.

[28] Benoit Carrier and Sylvie Granet. Numerical modeling of hydraulic fracture problem in permeable medium using cohesive zone model. *Engineering Fracture Mechanics*, 79:312–328, 2012.

[29] M. Charlotte, Gilles A. Francfort, and Lev Truskinovsky. Revisiting brittle fracture as an energy minimization problem : Comparisons of griffith and barenblatt surface energy models. In *Symposium on Continuous Damage and Fracture*, pages 7–12. Elsevier, 2000.

[30] Miguel Charlotte, Jérôme Laverne, and Jean-Jacques Marigo. Initiation of cracks with cohesive force models: a variational approach. *European Journal of Mechanics-A/Solids*, 25(4):649–669, 2006.

[31] Chunhui Chen and Olvi L Mangasarian. A class of smoothing functions for nonlinear and mixed complementarity problems. *Computational Optimization and Applications*, 5(2):97–138, 1996.

[32] Francis Clarke. *Functional analysis, calculus of variations and optimal control*, volume 264. Springer Science & Business Media, 2013.

[33] Frank H Clarke. *Optimization and nonsmooth analysis*, volume 5. Siam, 1990.

[34] Philip L Clarke and Reza Abedi. Modeling the connectivity and intersection of hydraulically loaded cracks with in situ fractures in rock. *International Journal for Numerical and Analytical Methods in Geomechanics*, 42(14):15921623, 2018.

[35] Richard Courant, Kurt Friedrichs, and Hans Lewy. On the partial difference equations of mathematical physics. *IBM journal of Research and Development*, 11(2):215–234, 1967.

[36] Brian N Cox, Huajian Gao, Dietmar Gross, and Daniel Rittel. Modern topics and challenges in dynamic fracture. *Journal of the Mechanics and Physics of Solids*, 53(3):565–596, 2005.

[37] Peter A Cundall and Roger D Hart. Numerical modelling of discontinua. *Engineering Computations*, 9(2):101–113, 1992.

[38] Christophe Daux, Nicolas Moës, John Dolbow, Natarajan Sukumar, and Ted Belytschko. Arbitrary branched and intersecting cracks with the extended finite element method. *International Journal for Numerical Methods in Engineering*, 48(12):1741–1760, 2000.

[39] Gianpietro Del Piero. One-dimensional ductile-brittle transition, yielding, and structured deformations. In *IUTAM Symposium on Variations of Domain and Free-Boundary Problems in Solid Mechanics*, pages 203–210. Springer, 1999.

[40] J Desroches, E Detournay, B Lenoach, P Papanastasiou, John Richard Anthony Pearson, M Thiercelin, and Ailan Cheng. The crack-tip region in hydraulic fracturing. *Proc. R. Soc. Lond. A*, 447(1929):39–48, 1994.

[41] E Detournay. Propagation regimes of fluid-driven fractures in impermeable rocks. *International Journal of Geomechanics*, 4(1):35–45, 2004.

[42] John Everett Dolbow. An extended finite element method with discontinuous enrichment for applied mechanics. 2000.

[43] Donald S Dugdale. Yielding of steel sheets containing slits. *Journal of the Mechanics and Physics of Solids*, 8(2):100–104, 1960.

[44] Fazil Erdogan and GC Sih. On the crack extension in plates under plane loading and transverse shear. *Journal of Basic Engineering*, 85(4):519–525, 1963.

[45] Horacio D Espinosa and Pablo D Zavattieri. A grain level model for the study of failure initiation and evolution in polycrystalline brittle materials. part i: Theory and numerical implementation. *Mechanics of Materials*, 35(3-6):333–364, 2003.

[46] Sonia Fernández-Méndez and Antonio Huerta. Imposing essential boundary conditions in mesh-free methods. *Computer Methods in Applied Mechanics and Engineering*, 193(12-14):1257–1275, 2004.

[47] Jay Fineberg and Eran Bouchbinder. Recent developments in dynamic fracture: some perspectives. *International Journal of Fracture*, 196(1-2):33–57, 2015.

[48] JW Foulk III. An examination of stability in cohesive zone modeling. *Computer Methods in Applied Mechanics and Engineering*, 199(9-12):465–470, 2010.

[49] Gilles A Francfort and J-J Marigo. Revisiting brittle fracture as an energy minimization problem. *Journal of the Mechanics and Physics of Solids*, 46(8):1319–1342, 1998.

[50] L. B. Freund. *Dynamic Fracture Mechanics*. Cambridge Monographs on Mechanics. Cambridge University Press, 1990.

[51] Achim Fritz, Stefan Hüeber, and Barbara I Wohlmuth. A comparison of mortar and nitsche techniques for linear elasticity. *Calcolo*, 41(3):115–137, 2004.

[52] JC Gálvez, M Elices, GV Guinea, and J Planas. Mixed mode fracture of concrete under proportional and nonproportional loading. *International Journal of Fracture*, 94(3):267–284, 1998.

[53] Pritam Ganguly. *Spatial convergence of finite element cohesive interface networks*. PhD thesis, Cornell University, 2006.

[54] Pritam Ganguly and Katerina D Papoulia. Pinwheel meshes and branching of cohesive cracks. In *Fracture of Nano and Engineering Materials and Structures*, pages 969–970. Springer, 2006.

[55] Pritam Ganguly, Stephen A Vavasis, and Katerina D Papoulia. An algorithm for two-dimensional mesh generation based on the pinwheel tiling. *SIAM Journal on Scientific Computing*, 28(4):1533–1562, 2006.

[56] D Garagash and E Detournay. The tip region of a fluid-driven fracture in an elastic medium. *Journal of Applied Mechanics*, 67(1):183–192, 2000.

[57] Dmitry I Garagash. Propagation of a plane-strain hydraulic fracture with a fluid lag: Early-time solution. *International Journal of Solids and Structures*, 43(18-19):5811–5835, 2006.

[58] Dariusz Gawin, Bernhard A Schrefler, and M Galindo. Thermo-hydro-mechanical analysis of partially saturated porous materials. *Engineering Computations*, 13(7):113–143, 1996.

[59] Emmanuel E. Gdoutos. *Rayleigh Wave Speed*, pages 369–372. Springer Netherlands, Dordrecht, 2003.

[60] Emmanuel E Gdoutos, Chris A Rodopoulos, and John R Yates. *Problems of fracture mechanics and fatigue: a solution guide*. Springer Science & Business Media, 2013.

[61] Rudy JM Geelen, Yingjie Liu, John E Dolbow, and Antonio Rodríguez-Ferran. An optimization-based phase-field method for continuous-discontinuous crack propagation. *International Journal for Numerical Methods in Engineering*, 116(1):1–20, 2018.

[62] Rudy JM Geelen, Yingjie Liu, Tianchen Hu, Michael R Tupek, and John E Dolbow. A phase-field formulation for dynamic cohesive fracture. *Computer Methods in Applied Mechanics and Engineering*, 2019.

[63] J Geertsma, F De Klerk, et al. A rapid method of predicting width and extent of hydraulically induced fractures. *Journal of Petroleum Technology*, 21(12):1–571, 1969.

[64] Elizaveta Gordeliy and Anthony Peirce. Coupling schemes for modeling hydraulic fracture propagation using the XFEM. *Computer Methods in Applied Mechanics and Engineering*, 253:305–322, 2013.

[65] Mohsen Goudarzi and Soheil Mohammadi. Analysis of cohesive cracking in saturated porous media using an extrinsically enriched EFG method. *Computers and Geotechnics*, 63:183–198, 2015.

[66] Alan Griffith. The phenomena of rupture and flow in solids. *Transactions of the Royal Society London*, 221(582-593):163–198, 1921.

[67] Youn Doh Ha and Florin Bobaru. Studies of dynamic crack propagation and crack branching with peridynamics. *International Journal of Fracture*, 162(1-2):229–244, 2010.

[68] Anita Hansbo and Peter Hansbo. A finite element method for the simulation of strong and weak discontinuities in solid mechanics. *Computer Methods in Applied Mechanics and Engineering*, 193(33-35):3523–3540, 2004.

[69] Peter Hansbo and Mats G Larson. Discontinuous galerkin methods for incompressible and nearly incompressible elasticity by nitsche's method. *Computer Methods in Applied Mechanics and Engineering*, 191(17-18):1895–1908, 2002.

[70] Peter Hansbo and Kent Salomonsson. A discontinuous galerkin method for cohesive zone modelling. *Finite Elements in Analysis and Design*, 102:1–6, 2015.

[71] JM Hanson, RA Schmidt, CH Cooley, JF Schatz, et al. Multiple fracture stimulation using controlled pulse pressurization. In *SPE Unconventional Gas Recovery Symposium*. Society of Petroleum Engineers, 1984.

[72] TS Hille, ASJ Suiker, and S Turteltaub. Microcrack nucleation in thermal barrier coating systems. *Engineering Fracture Mechanics*, 76(6):813–825, 2009.

[73] M Reza Hirmand and Katerina D Papoulia. A continuation method for rigid-cohesive fracture in a discontinuous Galerkin finite element setting. *International Journal for Numerical Methods in Engineering*, 115(5):627–650, 2018.

[74] Brad Lee Holian and Ramon Ravelo. Fracture simulations using large-scale molecular dynamics. *Phys. Rev. B*, 51:11275–11288, May 1995.

[75] George R Irwin. Analysis of stresses and strains near the end of a crack traversing a plate. *J. appl. Mech.*, 1957.

[76] Reji John and Surendra P Shah. Mixed-mode fracture of concrete subjected to impact loading. *Journal of Structural Engineering*, 116(3):585–602, 1990.

[77] S Kalthoff, JF; Winkler. Failure mode transition at high rates of shear loading. In *International Conference on Impact Loading and Dynamic Behavior of Materials*, pages 185–195, 1987.

[78] AR Khoei, H Azadi, and H Moslemi. Modeling of crack propagation via an automatic adaptive mesh refinement based on modified superconvergent patch recovery technique. *Engineering Fracture Mechanics*, 75(10):2921–2945, 2008.

[79] AR Khoei, OR Barani, and M Mofid. Modeling of dynamic cohesive fracture propagation in porous saturated media. *International Journal for Numerical and Analytical Methods in Geomechanics*, 35(10):1160–1184, 2011.

[80] AR Khoei, M Hirmand, M Vahab, and M Bazargan. An enriched FEM technique for modeling hydraulically driven cohesive fracture propagation in impermeable media with frictional natural faults: numerical and experimental investigations. *International Journal for Numerical Methods in Engineering*, 104(6):439–468, 2015.

[81] AR Khoei, M Vahab, E Haghighat, and S Moallemi. A mesh-independent finite element formulation for modeling crack growth in saturated porous media based on an enriched FEM technique. *International Journal of Fracture*, 188(1):79–108, 2014.

[82] AR Khoei, M Vahab, and M Hirmand. Modeling the interaction between fluid-driven fracture and natural fault using an enriched FEM technique. *International Journal of Fracture*, 197(1):1–24, 2016.

[83] AR Khoei, M Vahab, and M Hirmand. An enriched–fem technique for numerical simulation of interacting discontinuities in naturally fractured porous media. *Computer Methods in Applied Mechanics and Engineering*, 331:197–231, 2018.

[84] PA Klein, JW Foulk, EP Chen, SA Wimmer, and HJ Gao. Physics-based modeling of brittle fracture: cohesive formulations and the application of meshfree methods. *Theoretical and Applied Fracture Mechanics*, 37(1-3):99–166, 2001.

[85] Olga Kresse, Xiaowei Weng, Hongren Gu, and Ruiting Wu. Numerical modeling of hydraulic fractures interaction in complex naturally fractured formations. *Rock Mechanics and Rock Engineering*, 46(3):555–568, 2013.

[86] Brice Lecampion, Andrew Bunger, and Xi Zhang. Numerical methods for hydraulic fracture propagation: a review of recent trends. *Journal of Natural Gas Science and Engineering*, 49:66–83, 2018.

[87] Brice Lecampion and Emmanuel Detournay. An implicit algorithm for the propagation of a hydraulic fracture with a fluid lag. *Computer Methods in Applied Mechanics and Engineering*, 196(49-52):4863–4880, 2007.

[88] Jean Lemaitre. *A course on damage mechanics*. Springer Science & Business Media, 2012.

[89] Adrian Lew, Patrizio Neff, Deborah Sulsky, and Michael Ortiz. Optimal bv estimates for a discontinuous galerkin method for linear elasticity. *Applied Mathematics Research Express*, 2004(3):73–106, 2004.

[90] Guowei Liu, Qingbin Li, Mohammed A Msekh, and Zheng Zuo. Abaqus implementation of monolithic and staggered schemes for quasi-static and dynamic fracture phase-field model. *Computational Materials Science*, 121:35–47, 2016.

[91] E Lorentz. A mixed interface finite element for cohesive zone models. *Computer Methods in Applied Mechanics and Engineering*, 198(2):302–317, 2008.

[92] Eric Lorentz, Sam Cuvilliez, and Kyrylo Kazymyrenko. Convergence of a gradient damage model toward a cohesive zone model. *Comptes Rendus Mécanique*, 339(1):20–26, 2011.

[93] Jean-Jacques Marigo, Corrado Maurini, and Kim Pham. An overview of the modelling of fracture by gradient damage models. *Meccanica*, 51(12):3107–3128, 2016.

[94] Jens M Melenk and Ivo Babuška. The partition of unity finite element method: basic theory and applications. *Computer Methods in Applied Mechanics and Engineering*, 139(1-4):289–314, 1996.

[95] Thomas Menouillard and Ted Belytschko. Smoothed nodal forces for improved dynamic crack propagation modeling in XFEM. *International Journal for Numerical Methods in Engineering*, 84(1):47–72, 2010.

[96] J Mergheim, E Kuhl, and P Steinmann. A hybrid discontinuous galerkin/interface method for the computational modelling of failure. *Communications in Numerical Methods in Engineering*, 20(7):511–519, 2004.

[97] Christian Miehe, Martina Hofacker, and Fabian Welschinger. A phase field model for rate-independent crack propagation: Robust algorithmic implementation based on operator splits. *Computer Methods in Applied Mechanics and Engineering*, 199(45-48):2765–2778, 2010.

[98] Christian Miehe and Steffen Mauthe. Phase field modeling of fracture in multi-physics problems. part iii. crack driving forces in hydro-poro-elasticity and hydraulic fracturing of fluid-saturated porous media. *Computer Methods in Applied Mechanics and Engineering*, 304:619–655, 2016.

[99] Nicolas Moës and Ted Belytschko. Extended finite element method for cohesive crack growth. *Engineering Fracture Mechanics*, 69(7):813–833, 2002.

[100] Nicolas Moës, John Dolbow, and Ted Belytschko. A finite element method for crack growth without remeshing. *International Journal for Numerical Methods in Engineering*, 46(1):131–150, 1999.

[101] Peter Moonen, Jan Carmeliet, and LJ Sluys. A continuous–discontinuous approach to simulate fracture processes in quasi-brittle materials. *Philosophical Magazine*, 88(28-29):3281–3298, 2008.

[102] Jorge J Moré and Danny C Sorensen. Computing a trust region step. *SIAM Journal on Scientific and Statistical Computing*, 4(3):553–572, 1983.

[103] Alejandro Mota, Jaroslaw Knap, and Michael Ortiz. Fracture and fragmentation of simplicial finite element meshes using graphs. *International Journal for Numerical Methods in Engineering*, 73(11):1547–1570, 2008.

[104] Nathan M Newmark. A method of computation for structural dynamics. *Journal of the Engineering Mechanics Division*, 85(3):67–94, 1959.

[105] Vinh Phu Nguyen. Discontinuous Galerkin/extrinsic cohesive zone modeling: Implementation caveats and applications in computational fracture mechanics. *Engineering Fracture Mechanics*, 128:37–68, 2014.

[106] Vinh Phu Nguyena and Jian-Ying Wub. Modeling dynamic fracture of solids with a phase-field regularized cohesive zone model. *Computer Methods in Applied Mechanics and Engineering*, 340:1000–1022, 2018.

[107] Joachim Nitsche. Über ein variationsprinzip zur lösung von dirichlet-problemen bei verwendung von teilräumen, die keinen randbedingungen unterworfen sind. In *Abhandlungen aus dem mathematischen Seminar der Universität Hamburg*, volume 36, pages 9–15. Springer, 1971.

[108] Jorge Nocedal and Stephen J Wright. *Nonlinear Equations*. Springer, 2006.

[109] Ludovic Noels and Raul Radovitzky. A general discontinuous galerkin method for finite hyperelasticity. formulation and numerical applications. *International Journal for Numerical Methods in Engineering*, 68(1):64–97, 2006.

[110] Ludovic Noels and Raúl Radovitzky. Alternative approaches for the derivation of discontinuous galerkin methods for nonlinear mechanics. *Journal of Applied Mechanics*, 74(5):1031–1036, 2007.

[111] Ludovic Noels and Raúl Radovitzky. An explicit discontinuous galerkin method for non-linear solid dynamics: Formulation, parallel implementation and scalability properties. *International Journal for Numerical Methods in Engineering*, 74(9):1393–1420, 2008.

[112] Jon Edward Olson, Arash Dahi Taleghani, et al. Modeling simultaneous growth of multiple hydraulic fractures and their interaction with natural fractures. In *SPE Hydraulic Fracturing Technology Conference*. Society of Petroleum Engineers, 2009.

[113] Michael Ortiz and Anna Pandolfi. Finite-deformation irreversible cohesive elements for three-dimensional crack-propagation analysis. *International Journal for Numerical Methods in Engineering*, 44(9):1267–1282, 1999.

[114] Joško Ožbolt, Josipa Bošnjak, and Emiliano Sola. Dynamic fracture of concrete compact tension specimen: Experimental and numerical study. *International Journal of Solids and Structures*, 50(25-26):4270–4278, 2013.

[115] Joško Ožbolt, Akanshu Sharma, and Hans-Wolf Reinhardt. Dynamic fracture of concrete–compact tension specimen. *International Journal of Solids and Structures*, 48(10):1534–1543, 2011.

[116] Katerina D Papoulia. Non-differentiable energy minimization for cohesive fracture. *International Journal of Fracture*, 204(2):143–158, 2017.

[117] Katerina D Papoulia, Chin-Hang Sam, and Stephen A Vavasis. Time continuity in cohesive finite element modeling. *International Journal for Numerical Methods in Engineering*, 58(5):679–701, 2003.

[118] Katerina D Papoulia, Stephen A Vavasis, and Pritam Ganguly. Spatial convergence of crack nucleation using a cohesive finite-element model on a pinwheel-based mesh. *International Journal for Numerical Methods in Engineering*, 67(1):1–16, 2006.

[119] Matin Parchei Esfahani and Robert Gracie. On the undrained and drained hydraulic fracture splits. *International Journal for Numerical Methods in Engineering*.

[120] Kyoungsoo Park and Glaucio H Paulino. Cohesive zone models: a critical review of traction-separation relationships across fracture surfaces. *Applied Mechanics Reviews*, 64(6):060802, 2011.

[121] Kyoungsoo Park, Glaucio H Paulino, Waldemar Celes, and Rodrigo Espinha. Adaptive mesh refinement and coarsening for cohesive zone modeling of dynamic fracture. *International Journal for Numerical Methods in Engineering*, 92(1):1–35, 2012.

[122] Glaucio H Paulino, Kyoungsoo Park, Waldemar Celes, and Rodrigo Espinha. Adaptive dynamic cohesive fracture simulation using nodal perturbation and edge-swap operators. *International Journal for Numerical Methods in Engineering*, 84(11):1303–1343, 2010.

[123] RHJ d Peerlings, R De Borst, WAM d Brekelmans, and JHP De Vree. Gradient enhanced damage for quasi-brittle materials. *International Journal for Numerical Methods in Engineering*, 39(19):3391–3403, 1996.

[124] Anthony Peirce, Andrew Bunger, et al. Interference fracturing: nonuniform distributions of perforation clusters that promote simultaneous growth of multiple hydraulic fractures. *SPE Journal*, 20(02):384–395, 2015.

[125] LF Pereira, J Weerheijm, and LJ Sluys. A numerical study on crack branching in quasi-brittle materials with a new effective rate-dependent non-local damage model. *Engineering Fracture Mechanics*, 182:689–707, 2017.

[126] Carlo Peruzzo, Toan D Cao, E Milanese, P Favia, F Pesavento, Fazle Hussain, and Bernhard A Schrefler. Dynamics of fracturing saturated porous media and self-organization of rupture. *Journal of the Mechanics and Physics of Solids*, 111:113–133, 2018.

[127] Kim Pham, Hanen Amor, Jean-Jacques Marigo, and Corrado Maurini. Gradient damage models and their use to approximate brittle fracture. *International Journal of Damage Mechanics*, 20(4):618–652, 2011.

[128] Timon Rabczuk and T Belytschko. Cracking particles: a simplified meshfree method for arbitrary evolving cracks. *International Journal for Numerical Methods in Engineering*, 61(13):2316–2343, 2004.

[129] Raúl Radovitzky, Andrew Seagraves, Mike Tupek, and Ludovic Noels. A scalable 3D fracture and fragmentation algorithm based on a hybrid, discontinuous Galerkin, cohesive element method. *Computer Methods in Applied Mechanics and Engineering*, 200(1-4):326–344, 2011.

[130] M Ramulu and AS Kobayashi. Mechanics of crack curving and branchinga dynamic fracture analysis. In *Dynamic fracture*, pages 61–75. Springer, 1985.

[131] Ramsharan Rangarajan, Maurizio M Chiaramonte, Michael J Hunsweck, Yongxing Shen, and Adrian J Lew. Simulating curvilinear crack propagation in two dimensions with universal meshes. *International Journal for Numerical Methods in Engineering*, 102(3-4):632–670, 2015.

[132] K Ravi-Chandar and WG Knauss. An experimental investigation into dynamic fracture: I. crack initiation and arrest. *International Journal of Fracture*, 25(4):247–262, 1984.

[133] K Ravi-Chandar and B Yang. On the role of microcracks in the dynamic fracture of brittle materials. *Journal of the Mechanics and Physics of Solids*, 45(4):535–563, 1997.

[134] JJC Remmers, Rene de Borst, and A Needleman. A cohesive segments method for the simulation of crack growth. *Computational Mechanics*, 31(1-2):69–77, 2003.

[135] Julien Réthoré, René De Borst, and Marie-Angèle Abellan. A two-scale approach for fluid flow in fractured porous media. *International Journal for Numerical Methods in Engineering*, 71(7):780–800, 2007.

[136] Julien Réthoré, Rene De Borst, and Marie-Angèle Abellan. A two-scale model for fluid flow in an unsaturated porous medium with cohesive cracks. *Computational Mechanics*, 42(2):227–238, 2008.

[137] Peter Richtárik and Martin Takáč. Parallel coordinate descent methods for big data optimization. *Mathematical Programming*, 156(1-2):433–484, 2016.

[138] D Rittel and H Maigre. An investigation of dynamic crack initiation in PMMA. *Mechanics of Materials*, 23(3):229–240, 1996.

[139] Gonzalo Ruiz, Anna Pandolfi, and Michael Ortiz. Three-dimensional cohesive modeling of dynamic mixed-mode fracture. *International Journal for Numerical Methods in Engineering*, 52(1-2):97–120, 2001.

[140] Chin-Hang Sam, Katerina D Papoulia, and Stephen A Vavasis. Obtaining initially rigid cohesive finite element models that are temporally convergent. *Engineering Fracture Mechanics*, 72(14):2247–2267, 2005.

[141] S Samimi and A Pak. A fully coupled element-free Galerkin model for hydromechanical analysis of advancement of fluid-driven fractures in porous media. *International Journal for Numerical and Analytical Methods in Geomechanics*, 40(16):2178–2206, 2016.

[142] Jessica D Sanders, Tod A Laursen, and Michael A Puso. A nitsche embedded mesh method. *Computational Mechanics*, 49(2):243–257, 2012.

[143] I Scheider and W Brocks. Simulation of cup–cone fracture using the cohesive model. *Engineering Fracture Mechanics*, 70(14):1943–1961, 2003.

[144] Johannes Cornelis Jacobus Schellekens. Computational strategies for composite structures. *NASA STI/Recon Technical Report N*, 94, 1993.

[145] Bernhard A Schrefler, Stefano Secchi, and Luciano Simoni. On adaptive refinement techniques in multi-field problems including cohesive fracture. *Computer Methods in Applied Mechanics and Engineering*, 195(4-6):444–461, 2006.

[146] Robert Sedgewick. *Algorithms*. Pearson Education India, 1988.

[147] Randolph R Settgast and Mark M Rashid. Continuum coupled cohesive zone elements for analysis of fracture in solid bodies. *Engineering Fracture Mechanics*, 76(11):1614–1635, 2009.

[148] Shen Shang and Gun Jin Yun. Stochastic finite element with material uncertainties: Implementation in a general purpose simulation program. *Finite Elements in Analysis and Design*, 64:65–78, 2013.

[149] Eran Sharon and Jay Fineberg. Microbranching instability and the dynamic fracture of brittle materials. *Physical Review B*, 54(10):7128, 1996.

[150] Eran Sharon, Steven P Gross, and Jay Fineberg. Local crack branching as a mechanism for instability in dynamic fracture. *Physical Review Letters*, 74(25):5096, 1995.

[151] Yongxing Shen. A variational inequality formulation to incorporate the fluid lag in fluid-driven fracture propagation. *Computer Methods in Applied Mechanics and Engineering*, 272:17–33, 2014.

[152] Stewart A Silling. Reformulation of elasticity theory for discontinuities and long-range forces. *Journal of the Mechanics and Physics of Solids*, 48(1):175–209, 2000.

[153] Jeong-Hoon Song and Ted Belytschko. Cracking node method for dynamic fracture with finite elements. *International Journal for Numerical Methods in Engineering*, 77(3):360–385, 2009.

[154] Jeong-Hoon Song, Thomas Menouillard, and Alireza Tabarraei. Explicit dynamic finite element method for failure with smooth fracture energy dissipations. *Mathematical Problems in Engineering*, 2013, 2013.

[155] DA Spence and P Sharp. Self-similar solutions for elastohydrodynamic cavity flow. *Proc. R. Soc. Lond. A*, 400(1819):289–313, 1985.

[156] M Stolarska, David L Chopp, Nicolas Moës, and Ted Belytschko. Modelling crack growth by level sets in the extended finite element method. *International Journal for Numerical Methods in Engineering*, 51(8):943–960, 2001.

[157] Erik Svenning. A weak penalty formulation remedying traction oscillations in interface elements. *Computer Methods in Applied Mechanics and Engineering*, 310:460–474, 2016.

[158] Arash D Taleghani. *Analysis of hydraulic fracture propagation in fractured reservoirs: an improved model for the interaction between induced and natural fractures*. PhD thesis, University of Texas at Austin, 2009.

[159] Arash Dahi Taleghani, Jon E Olson, et al. How natural fractures could affect hydraulic-fracture geometry. *SPE Journal*, 19(01):161–171, 2013.

[160] A Tootoonchi, A Khoshghalb, GR Liu, and N Khalili. A cell-based smoothed point interpolation method for flow-deformation analysis of saturated porous media. *Computers and Geotechnics*, 75:159–173, 2016.

[161] Timothy J Truster and Arif Masud. A discontinuous/continuous Galerkin method for modeling of interphase damage in fibrous composite systems. *Computational Mechanics*, 52(3):499–514, 2013.

[162] Chin-Fu Tsang. Coupled hydromechanical-thermochemical processes in rock fractures. *Reviews of Geophysics*, 29(4):537–551, 1991.

[163] Paul Tseng. Convergence of a block coordinate descent method for nondifferentiable minimization. *Journal of Optimization Theory and Applications*, 109(3):475–494, 2001.

[164] M Vahab and N Khalili. X-FEM modeling of multizone hydraulic fracturing treatments within saturated porous media. *Rock Mechanics and Rock Engineering*, pages 1–21, 2018.

[165] Mohammad Vahab and Nasser Khalili. Computational algorithm for the anticipation of the fluid-lag zone in hydraulic fracturing treatments. *International Journal of Geomechanics*, 18(10):04018139, 2018.

[166] FP Van der Meer and LJ Sluys. A phantom node formulation with mixed mode cohesive law for splitting in laminates. *International Journal of Fracture*, 158(2):107, 2009.

[167] FP Van der Meer, LJ Sluys, SR Hallett, and MR Wisnom. Computational modeling of complex failure mechanisms in laminates. *Journal of Composite Materials*, 46(5):603–623, 2012.

[168] JG Wang, Y Zhang, JS Liu, and BY Zhang. Numerical simulation of geofluid focusing and penetration due to hydraulic fracture. *Journal of Geochemical Exploration*, 106(1-3):211–218, 2010.

[169] Garth N Wells and LJ Sluys. A new method for modelling cohesive cracks using finite elements. *International Journal for Numerical Methods in Engineering*, 50(12):2667–2682, 2001.

[170] MF Wheeler, T Wick, and W Wollner. An augmented-lagrangian method for the phase-field approach for pressurized fractures. *Computer Methods in Applied Mechanics and Engineering*, 271:69–85, 2014.

[171] Zachary A Wilson and Chad M Landis. Phase-field modeling of hydraulic fracture. *Journal of the Mechanics and Physics of Solids*, 96:264–290, 2016.

[172] Paul Adams Witherspoon, Joseph SY Wang, K Iwai, and John E Gale. Validity of cubic law for fluid flow in a deformable rock fracture. *Water Resources Research*, 16(6):1016–1024, 1980.

[173] P Wriggers and Giorgio Zavarise. A formulation for frictionless contact problems using a weak form introduced by nitsche. *Computational Mechanics*, 41(3):407–420, 2008.

[174] Stephen Wright and Jorge Nocedal. Numerical optimization. *Springer Science*, 35(67-68):7, 1999.

[175] Stephen J Wright. Coordinate descent algorithms. *Mathematical Programming*, 151(1):3–34, 2015.

[176] X-P Xu and A Needleman. Numerical simulations of dynamic crack growth along an interface. *International Journal of Fracture*, 74(4):289–324, 1996.

[177] X-P Xu and Alan Needleman. Numerical simulations of fast crack growth in brittle solids. *Journal of the Mechanics and Physics of Solids*, 42(9):1397–1434, 1994.

[178] XP Xu, A Needleman, and Farid F Abraham. Effect of inhomogeneities on dynamic crack growth in an elastic solid. *Modelling and Simulation in Materials Science and Engineering*, 5(5):489, 1997.

[179] Chengzeng Yan, Hong Zheng, Guanhua Sun, and Xiurun Ge. Combined finite-discrete element method for simulation of hydraulic fracturing. *Rock Mechanics and Rock Engineering*, 49(4):1389–1410, 2016.

[180] Elizabeth H Yoffe. Lxxv. the moving griffith crack. *The London, Edinburgh, and Dublin Philosophical Magazine and Journal of Science*, 42(330):739–750, 1951.

[181] Xi Zhang, Robert G Jeffrey, and Marc Thiercelin. Deflection and propagation of fluid-driven fractures at frictional bedding interfaces: a numerical investigation. *Journal of Structural Geology*, 29(3):396–410, 2007.

[182] Fenghua Zhou and Jean-Francois Molinari. Dynamic crack propagation with cohesive elements: a methodology to address mesh dependency. *International Journal for Numerical Methods in Engineering*, 59(1):1–24, 2004.

[183] Fenghua Zhou, Jean-Francois Molinari, and Tadashi Shioya. A rate-dependent cohesive model for simulating dynamic crack propagation in brittle materials. *Engineering Fracture Mechanics*, 72(9):1383–1410, 2005.

[184] Robert W Zimmerman and Gudmundur S Bodvarsson. Hydraulic conductivity of rock fractures. *Transport in Porous Media*, 23(1):1–30, 1996.

APPENDICES

Appendix A

Matrix equations of the continuation algorithm

The finite element approximation $\mathbf{u}_h(\mathbf{x},t)$ is expressed in compact form as

$$\mathbf{u}_h(\mathbf{x},t) = \mathbf{N}^u(\mathbf{x})\,\mathbf{U}(t), \qquad \mathbf{x}\in\Omega_h \tag{A.1}$$

where $\mathbf{U}(t)$ is the vector of all displacement nodal degrees of freedom and $\mathbf{N}^u(\mathbf{x})$ is the matrix of finite element shape functions. The traces of the shape functions on $\Gamma^+_{d,h}$, and $\Gamma^-_{d,h}$ are denoted by $\mathbf{N}^{u+}$ and $\mathbf{N}^{u-}$, respectively, and are used to approximate the displacement jump $[\![\mathbf{u}_h]\!]$ as

$$[\![\mathbf{u}_h(\mathbf{x},t)]\!] = \mathbf{N}^{[\![u]\!]}(\mathbf{x})\,\mathbf{U}(t) \quad \text{with} \quad \mathbf{N}^{[\![u]\!]} = [\mathbf{N}^{u+} \quad -\mathbf{N}^{u-}], \qquad \mathbf{x}\in\Gamma_{d,h}. \tag{A.2}$$

Similarly, the finite element approximation $\boldsymbol{\delta}_h(\mathbf{x},t)$ is written as

$$\boldsymbol{\delta}_h(\mathbf{x},t) = \mathbf{N}^\delta(\mathbf{x})\,\mathbf{d}(t), \qquad \mathbf{x}\in\Gamma_{d,h}, \tag{A.3}$$

where $\mathbf{d}(t)$ is the vector of all discontinuity opening nodal degrees of freedom and $\mathbf{N}^\delta(\mathbf{x})$ is the matrix containing the finite element shape functions.

The gradient vector of the finite-dimensional potential in (2.9) is given by

$$\mathbf{g} = \left\{ \begin{array}{c} \mathbf{g}_u \\ \mathbf{g}_\delta \end{array} \right\}, \tag{A.4}$$

with

$$\begin{aligned}\mathbf{g}_u = &\int_{\Omega_h\setminus\Gamma_{d,h}} \mathbf{B}^T\boldsymbol{\sigma}_h\,dV + \int_{\Omega_h\setminus\Gamma_{d,h}} (\mathbf{N}^u)^T\ddot{\mathbf{u}}_h\,dV \\ &- \int_{\partial_t\Omega_h} (\mathbf{N}^u)^T\widetilde{\mathbf{t}}\,dV - \int_{\Omega_h\setminus\Gamma_{d,h}} (\mathbf{N}^u)^T\mathbf{b}\,dV \\ &+ \int_{\Gamma_{d,h}} (\mathbf{N}^{[\![u]\!]})^T\bar{\boldsymbol{\lambda}}_h^{\mathrm{DG}}\,dS + \int_{\Gamma_{d,h}} (\mathbf{B}^{\langle\sigma\rangle})^T\mathbf{D}\bar{\mathbf{n}}_d^T\boldsymbol{g}_h\,dS,\end{aligned} \tag{A.5}$$

and

$$\mathbf{g}_\delta = \int_{\Gamma_{d,h}} (\mathbf{N}^\delta)^T(\mathbf{t}_{\mathrm{cohs}} + \mathbf{t}_{\mathrm{cont}} - \bar{\boldsymbol{\lambda}}_h^{\mathrm{DG}})\,dS, \tag{A.6}$$

where $\bar{\boldsymbol{\lambda}}_h^{\mathrm{DG}} = \langle\boldsymbol{\sigma}_h\rangle\,\mathbf{n}_d + \eta\boldsymbol{g}_h$. In the above, $\mathbf{B}$ is the usual strain-displacement matrix containing spatial derivatives of the displacement shape functions, $\boldsymbol{\sigma}$ (by a slight abuse of notation) denotes the Cauchy stress in vector form, and $\mathbf{B}^{\langle\sigma\rangle} = \frac{1}{2}[\mathbf{B}^+ \;\; \mathbf{B}^-]$ serves to approximate $\langle\boldsymbol{\sigma}_h\rangle$ using the strain-displacement matrices $\mathbf{B}^+$ and $\mathbf{B}^-$ computed on the two sides of the discontinuity. $\overline{\mathbf{n}}_d$ contains the components of the normal vector $\mathbf{n}_d$ and is defined for the transformation from tensorial to matrix formulation as

$$\begin{aligned}\overline{\mathbf{n}}_d &= \begin{bmatrix} n_x & 0 & n_y \\ 0 & n_y & n_x \end{bmatrix} \quad \text{in 2D}, \\ \overline{\mathbf{n}}_d &= \begin{bmatrix} n_x & 0 & 0 & n_y & 0 & n_z \\ 0 & n_y & 0 & n_x & n_z & 0 \\ 0 & 0 & n_z & 0 & n_y & n_x \end{bmatrix} \quad \text{in 3D}.\end{aligned} \tag{A.7}$$

The Hessian matrix is given by

$$\mathbf{H} = \begin{bmatrix} \mathbf{H}_{uu} & \mathbf{H}_{u\delta} \\ \mathbf{H}_{\delta u} & \mathbf{H}_{\delta\delta} \end{bmatrix}, \tag{A.8}$$

with

$$\begin{aligned}\mathbf{H}_{uu} = &\int_{\Omega_h\setminus\Gamma_{d,h}} \mathbf{B}^T\mathbf{D}\mathbf{B}\,dV + \frac{2}{a_2\Delta t^2}\int_{\Omega_h\setminus\Gamma_{d,h}} (\mathbf{N}^u)^T\rho\mathbf{N}^u\,dV + \int_{\Gamma_{d,h}} \eta(\mathbf{N}^{[\![u]\!]})^T\mathbf{N}^{[\![u]\!]}\,dS \\ &+ \int_{\Gamma_{d,h}} (\mathbf{N}^{[\![u]\!]})^T\overline{\mathbf{n}}_d\mathbf{D}\mathbf{B}^{\langle\sigma\rangle}\,dS + \int_{\Gamma_{d,h}} (\mathbf{B}^{\langle\sigma\rangle})^T\mathbf{D}\overline{\mathbf{n}}_d\mathbf{N}^{[\![u]\!]}\,dS, \\ \mathbf{H}_{u\delta} = \mathbf{H}_{\delta u}^T = &-\int_{\Gamma_{d,h}} \eta(\mathbf{N}^{[\![u]\!]})^T\mathbf{N}^\delta\,dS - \int_{\Gamma_{d,h}} (\mathbf{B}^{\langle\sigma\rangle})^T\mathbf{D}\overline{\mathbf{n}}_d\mathbf{N}^\delta\,dS, \\ \mathbf{H}_{\delta\delta} = &\int_{\Gamma_{d,h}} \eta(\mathbf{N}^\delta)^T\mathbf{N}^\delta\,dS + \int_{\Gamma_{d,h}} (\mathbf{N}^\delta)^T\mathbf{D}_d\mathbf{N}^\delta\,dS,\end{aligned} \tag{A.9}$$

in which $\mathbf{D}_d = \nabla_\delta(\mathbf{t}_{\text{cohs}} + \mathbf{t}_{\text{cont}})$ and $\mathbf{D}$ (by a slight abuse of notation) is the elasticity matrix. In the above, a_2 is the Newmark scheme parameter, η is the penalty parameter as defined in Equation (2.8), and ρ is the material density, as mentioned previously in the text.

Appendix B

Generalized differential calculus

Let $f : \mathbb{R}^{n_{\text{dim}}} \to \mathbb{R}$ be a real valued function (not necessarily differentiable or convex) and suppose that f is *Lipschitz continuous* near $\mathbf{x} \in \mathbb{R}^{n_{\text{dim}}}$. The *generalized directional derivative* of f evaluated at $\mathbf{x}$ in the direction $\mathbf{v}$ is a well-defined finite quantity given by

$$f'_{\mathbf{v}}(\mathbf{x}) = \lim_{\substack{\xi \to 0 \\ \mathbf{y} \to \mathbf{x}}} \sup \frac{f(\mathbf{y} + \xi \mathbf{v}) - f(\mathbf{y})}{\xi}. \tag{B.1}$$

The *generalized gradient* of f at $\mathbf{x}$, denoted $\partial f(\mathbf{x})$, is a non-empty sub-set of $\mathbb{R}^{n_{\text{dim}}}$ and is defined as [32, 33]

$$\partial f(\mathbf{x}) = \left\{ \mathbf{s} \in \mathbb{R}^{n_{\text{dim}}} \mid \mathbf{s} \cdot \mathbf{v} \leq f'_{\mathbf{v}}(\mathbf{x}) \ \text{ for all } \mathbf{v} \in \mathbb{R}^{n_{\text{dim}}} \right\}. \tag{B.2}$$

The above definition of generalized gradient reduces to the singleton set $\{\nabla f(\mathbf{x})\}$ when f is differentiable (smooth) at $\mathbf{x}$. At a non-differentiable point, the slope corresponding to each member of $\partial f(\mathbf{x})$ is less steep than the slope of any directional derivative of f at $\mathbf{x}$ considering all admissible directions $\mathbf{v}$. In the context of convex analysis, $\partial f(\mathbf{x})$ is usually referred to as the sub-differential of f. In that case, each member of $\partial f(\mathbf{x})$ is called a sub-gradient of f at $\mathbf{x}$. Just as in differential calculus, where derivatives are rarely computed from the definition, one appeals to a body of theory and to certain rules that characterize generalized gradients, see [32, 33].

Suppose now that f is a convex function of $\mathbf{x}$ so that it attains a minimum (and not a maximum) in its domain of definition. The definition of the generalized gradient equation (B.2) allows for generalization of the minimality condition of f. It follows that a point $\mathbf{x}^\star$ is a global minimizer of f if and only if [32, 33]

$$\mathbf{0} \in \partial f(\mathbf{x}^\star), \tag{B.3}$$

that is, $\mathbf{0}$ is a sub-gradient of f at $\mathbf{x}^\star$. The above condition reduces to the well-known condition $\nabla f(\mathbf{x}^\star) = \mathbf{0}$ when f is differentiable at $\mathbf{x}^\star$. A useful property of the generalized gradient is that $\partial(f_1 + f_2)(\mathbf{x}) = \partial f_1(\mathbf{x}) + \partial f_2(\mathbf{x})$, in which the RHS stands for addition in a *Minkowski* sense, i.e., adding each member in $\partial f_1(\mathbf{x})$ to each member of $\partial f_2(\mathbf{x})$.[1]

[1] Actually, one generally has $\partial(f_1+f_2)(\mathbf{x}) \subseteq \partial f_1(\mathbf{x})+\partial f_2(\mathbf{x})$. The inclusion turns to equality only under certain conditions as explained in [32, 33]. It is possible to show that an equality holds in our subsequent analysis of π_δ.